Development of CMOS Image Sensors for Subretinal Stimulation and On-chip Bioimaging of the Brain

---

網膜刺激及び脳埋め込みオンチップバイオイメージング用 CMOS イメージセンサの開発

David Ng Chee Keong

March 2006

NARA INSTITUTE OF SCIENCE AND TECHNOLOGY

GRADUATE SCHOOL OF MATERIALS SCIENCE

Abstract

The work described in this thesis focuses on the development of CMOS image sensors for two bioimaging applications; in vivo imaging of the mouse brain and electrical stimulation of retinal cells. After an introduction to the background on imaging devices in Chapter 1, I present the approach of using CMOS technology to achieve my research objective. In Chapter 2, the fundamental questions related to this approach in comparison with other available technologies are discussed. Here, the advantages of using CMOS technology are presented. Next, the CMOS device characteristic, especially the photosensor is described in detail. Implementation of the CMOS photosensor for image sensing with relevance to on-chip imaging configuration is presented. In Chapter 3, the initial work leading to the demonstration of on-chip fluorescence image is described. The use of pulse width modulation photosensing was explored for fluorescence measurements. A novel packaging method was developed to enable on-chip fluorescence imaging. Following the work in Chapter 3, a fully packaged CMOS image sensor was used to demonstrate in vitro and in vivo imaging of the mouse brain. This work is described in Chapter 4. The obtained results represent for the first time a report on imaging of the intact mouse brain using a CMOS image sensor. Here, fluorescence imaging deep inside the mouse brain was demonstrated and quantitative measurement of the fluorescence signal for functional study of the brain was obtained. Chapter 5 explores the use of the CMOS sensor to generate sufficient stimulus current for use as a retinal prosthesis device. In this work, I also investigated the change in performance of the CMOS device due to bending to the curvature of the eye. Fundamental issues related to charge mobility of semiconductor devices is investigated. Finally Chapter 6 concludes this thesis and gives a brief outlook for future work.

Acknowledgement

A reflection on the cumulative efforts that culminated to the realization of this thesis brings a flash of emotions that are difficult to describe. Nevertheless, the journey here has been made more pleasant due to the presence of many people who have helped me along the way. I have the highest regards for these people and would like to express my endless gratitude for their help and assistance.

To Professor Masahiro Nunoshita and Professor Jun Ohta, I hold my humblest respect and utmost appreciation. The constant guidance and encouragement they have provided throughout my entire graduate studies have helped in immeasurable ways. Admittedly, the pressures of a graduate student can seem quite insurmountable at times, but on hindsight, it's the very pressure that keeps one motivated and to excel. I am extremely grateful to Professor Masahiro Nunoshita for his very valuable suggestions and constructive comments throughout my work. I believe his kind words have imparted on me positive values that have led me to become more effective and efficient. I am very thankful to Professor Ohta for his generosity in spending time to impart on me invaluable advice and to share a few words of wisdom. The experience has certainly given me a fresh perspective, and I have ever since started to compile a list of my favorite Japanese proverbs and idioms. I would also like to acknowledge my dissertation committee for their helpful discussions and comments; Professor Tadashi Shiosaki for his expertise and willingness to make unique and constructive suggestions, and Professor Sadao Shiosaka for his inspiring suggestions that have led to new ideas for my work.

My first impression of Japan was an unforgettable one due to the warm hospitality of the people that I met. When I first arrived in Japan, I was warmly greeted by the kind staff of the

Association of International Education, Japan (AIEJ) who helped whisked us to our respective destinations and provided us with some pocket money. Then I was warmly welcomed by Dr. Keiichiro Kagawa and Professor Jun Ohta, who took time off to meet me at the Gakken Keihanna bus stop at 8 am in the morning. I later found out that, compared to the average standard (from my personal survey), 8 am in January is much too early in the morning to get out of bed. I have since had the pleasure to study and research under the supervision of Dr. Kagawa who has helped me in more ways that I can remember. On a personal level, I would like to extend my appreciation to Dr. Kagawa who has introduced me to the many facets of Japanese life outside of the laboratory. I can say with conviction that the experience has helped me understand a little more about Japan, its people, its culture and why there is absolutely no equal to the famous *Hida* beef.

I am deeply grateful to Dr. Takashi Tokuda who has shown me the qualities of an excellent researcher. Under his close supervision, I have learnt the proper way to conduct experiments and the best approach to present my results and findings in papers as well as conferences. His expertise in a wide range of topics never fails to impress and motivate me. Most of all, I am touched by his sincerity and understanding (perhaps as a fellow father) who would sometimes bend his back to accommodate my request for time off work.

I would like to acknowledge the support and helpful discussion from Professor Sadao Shiosaka, Dr. Yasuyuki Ishikawa, and Mr. Hideki Tamura of the Graduate School of Biological Sciences. Their generous assistance and support provided have helped tremendously in shaping the work that forms part of this thesis. Furthermore, I cannot be grateful enough for the generous assistance, advice, and help offered by Mr. Tamura during the latter part of my work. I therefore, would like to share with him credit for the work involving the in vitro and in vivo imaging of the mouse brain.

The successful completion of this thesis has been supported by funding from various sources. The retinal prosthesis work has been kindly supported by the “Artificial Vision System” project (Project Leader: Professor Yasuo Tano, Osaka University) which is funded by the New Energy Development Organization (NEDO), and from the “A Development of Artificial Visual System by Retinal Stimulating Electrode” project (Principal Investigator: Professor Yasuo Tano, Osaka University) which is funded by the Department of Health, Welfare and Labour. The biomaging work has been kindly supported by the Semiconductor Technology Academic Research Center (STARC), and by the Ministry of Education, Culture, Sports, Science and Technology.

Over the years, I have had the privilege to work alongside the most capable researchers I have ever met. My thanks go to Dr. Akihiro Uehara of Nidek Co. who has brought me up to speed in LSI design and layout techniques. I have learnt a lot and received much help and guidance from Dr. Uehara’s expert knowledge. To my fellow comrades, Mr. Tetsuo Furumiya and Mr. Koji Yamamoto, I would like to acknowledge their companionship and mutual encouragement throughout our graduate study years. I am most grateful to Mr. Furumiya for his ever willingness to help me polish up my Japanese skills, both the technical and the not so technical. And to Mr. Yamamoto, I thank him for the helpful discussions on image sensor design. Not forgetting too is Dr. Kiyotaka Sasagawa, who is currently with the National Institute of Information and Communications Technology (NICT). I remember fondly the technical discussion with Dr. Sasagawa who possesses extensive experience and knowledge in his field. He serves as a role model by projecting great enthusiasm and motivation in carrying out his research.

I am thankful also to all the colleagues in the Photonics Device Science laboratory for their assistance, conversations, encouragement, and the pleasant atmosphere which they have cultivated. Special thanks go to the team members who are involved in the bioimaging project; Mr. Hideki Okamoto and Mr. Daisuke Mori both with Sony LSI Design Inc., Mr. Masamichi Matsuo, Mr. Akio Yamamoto, Mr. Kunihiro Tanaka, and Mr. Masayuki Kawada. They have been a constant source of help and support. It would be difficult to imagine the progress in my own work without their involvement. I would also like to extend my appreciation to Mr. Yi-Li Pan who is currently at Quanta Display Inc., Taiwan for sharing his wonderful insights and experience as a student and a friend. And to Ms. Kazumi Matsumoto, and Ms. Yuki Asano who have worked tirelessly to aid in the many important administrative work, your assistance has not been taken for granted. I am also grateful to my previous tutor and fellow student, Mr. Tomohiro Nishimura, who is now at Omron Corporation. He has helped me tremendously during my initial stay in Japan.

My heartfelt gratitude to the people who have indirectly but inadvertently helped me during the course of their work. Their contributions will always be cherished and remembered. My sincerest appreciation goes to the friendly volunteer teachers of Network Ikoma, especially Ms. Fumiko Yamazaki, Ms. Keiko Saito, and Mr. Tatsuo Yamagami. My Japanese language skill has improved only because of the dedication that you have shown in your work. And to the Asian Youth Fellowship Program (AYFP) staff and students, especially the kind and patient teachers, Ms. Noriko Osawa, Ms. Reiko Inomata, Ms. Kyoko Bandai, and Mr. Takeshi Fujisawa, who sacrificed a year of their life in order to bring us up to speed in out Japanese proficiency, I have a special place in my heart for them all. And of course, to the ever helpful and resourceful AYFP coordinator, Ms. Seiko Fujimoto, and AYFP senior associate who devoted 10 years to the AYF program, Ms. Kyoko Nakano, my sincerest gratitude.

To the NAIST library staff, I offer my special appreciation. They have worked tirelessly behind the scene, busily delivering the manuscripts that are unavailable online, and many times at astonishing speeds. I believe their pace at work is matched only by their dedication. And to the NAIST Student Affairs Division, and the staff of the previous International Center who I believe knew all the foreign students personally, your help and assistance is firmly acknowledged.

I am deeply thankful to the staff of Ikoma City Hall, especially to the National Health Insurance Division and the Children Welfare Division for taking good care of the welfare of my family. They have provided me with a peace of mind so that I can concentrate fully on my work.

I am grateful to the Japan Ministry of Education, Culture, Sports, Science and Technology for their kind sponsorship throughout my stay here in Japan. Through their generous support, my family and I have been able to live comfortably. My hope is that I have produced the satisfactory results that have been expected of me.

To all my acquaintances and correspondents, your kind support and encouragements is the key to my sustenance. And to the readers who have been patient with me in this lengthy acknowledgement, I hope you do not mind my lack of economy.

Finally, I reserve my greatest appreciation to my family for their unconditional love and support. To my parents, Yan Gim and Sam Fong, who stood by me constantly, and my elder sister and younger brothers, Diana, Daniel and Dominic, who believed in me unwaveringly, I thank them from the bottom of my heart. And most of all to my beloved wife, Wee Fuen, who has been like a sturdy anchor during the roughest moments, and a bright guiding beacon when the passage seems uncertain, she saves me from the insanity of being drowned by the pressures of my work. I am constantly being motivated by her perpetual and almost sagely words, “Dear, when are you graduating?” to which I can finally tell her, “Now, my dear, now.” Above all, I owe it to her for the most wonderful gift that can be bestowed upon any person; the precious gift of children. The glistening eyes of Phoebe and Ernest, may take a whole lot of getting used to, but are like priceless jewels incomparable to any possessions imaginable. To them, I owe them this work and much, much more.

Contents

Chapter 5 Electrical Stimulation and Effect of Mechanical Strain 117

Chapter 1
Introduction

1.1 Background

Imaging devices are being used in many areas, from medical research to space exploration as shown in Fig. 1.1. In the medical and scientific research, imaging devices are essential to advance the field in search of better diagnostic and monitoring tools or devices to help humanity. For example the research work in retinal prosthesis devices holds promise for those who lost their sights and enable the blind to regain some form of visual recovery [1]. On the other end of the spectrum, imaging devices for interplanetary exploration are giving us a glimpse of another world [2]. In between these fields, there are numerous examples where imaging devices are increasingly being utilized for scientific and industrial applications [3-5].

Traditionally, most imaging devices have been based on charge-coupled device (CCD) technology. This is a mature technology where, major technological difficulties have been solved and manufacturing issues remains the main concern for producing a product to meet the demanded specifications. However, as recent as a decade ago, there has been rapid development in complementary metal oxide semiconductor (CMOS) image sensors. Although, both technologies were developed between the early and late 1970s, initial CMOS image sensors suffered from unacceptable performance and were generally overlooked until the early 1990s. By that time, advances in CMOS design were yielding chips with smaller pixel sizes, reduced noise, more capable image processing algorithms, and larger imaging arrays[6-8].

The renewed interest in CMOS image sensors has caused this option to become more mainstream and hence more readily available and accessible to the masses. Since then, a lot

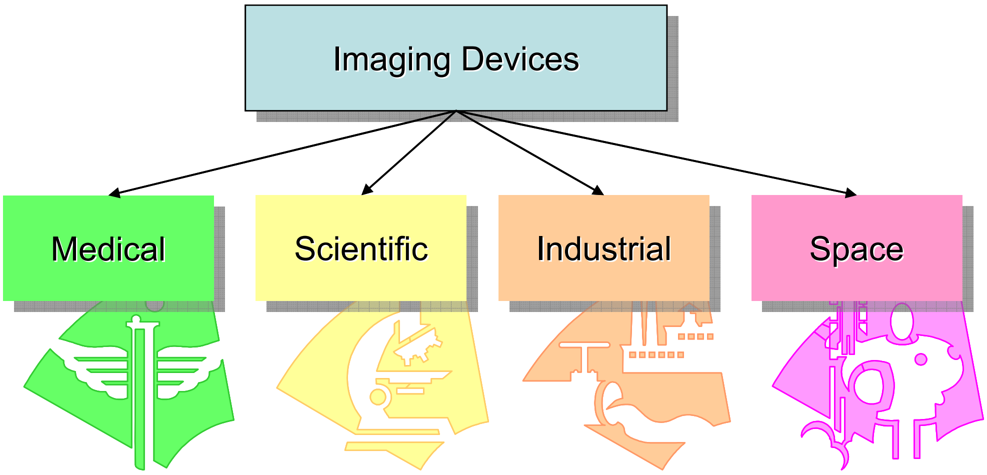

Fig. 1.1 Example of applications of imaging device.

more work has gone into improving its performance to meet or even achieve better than the specified requirements. What we are witnessing now are the development of ultra high speed imaging devices, extremely wide dynamic image sensors, and multi functional system on-chip cameras based on CMOS technology [9-13]. With the availability of these high performance CMOS imaging devices, we are led to the question of looking for niche applications that will make the most out of what these imaging devices has to offer.

While there are many applications that need high performance CMOS cameras, we believe the scientific and medical communities stand to benefit the most from these devices. Therefore, we have focused our work with respect to these fields. Two very important applications that have been identified are, in vitro and in vivo imaging, and retinal prosthesis. These applications will be used to showcase the benefit by implementing the use of CMOS image sensors. Consequently, we are exploring the many issues that need to be addressed before successful implementation of CMOS imaging devices in these two areas can be achieved. Success in this work will serve to demonstrate the viability of the CMOS image sensor for incorporation into a new class of imaging device for further improvement in the medical and scientific imaging field.

1.1.1 In vitro and In vivo Tissue Imaging

Microscopes and their various derivates have been the traditional tools used by biologists and scientists to study cells, both living and dead, of animals and plants. However, the size of these instruments excludes their use in high-throughput, portable diagnostic and in vivo sensing applications. A new device that can image down to the cellular level of a live moving animal would be the ultimate imaging device. Efforts to develop miniaturized systems have resulted in a variety of designs and implementations [14-16]. Recently, CMOS-based devices have shown viability as a new class of emerging micro sensing devices [17-23]. Some of these devices are increasingly being explored to fill a niche application which involves fluorescence detection [24-26]. Although most of these work reported single pixel structures, one notable recent work involved the use of a CMOS image sensor for luminisecence detection and imaging [27]. We believe that important progress has been made so far to demonstrate the use of CMOS sensors for in vitro and in vivo imaging. The final step of applying a CMOS image sensor for these purposes will have a great impact on the development of a new and emerging device for in vitro and in vivo tissue imaging.

1.1.2 Retinal Prosthesis

It is estimated that 50 000 people in Japan and 1 500 000 people worldwide are blind because of photoreceptor deterioration due to retinitis pigmentosa (RP) [28]. Retinal degenerative diseases such as RP and age-related macular degeneration (AMD) have caused tens of millions of people to suffer varying degrees of irreversible vision loss. Many possible treatments are being explored and the artificial retina implant chip has been reported as a potential solution for patients that are blinded by RP or AMD [1, 29]. Several implementations of the implant chip have been reported. One method involves decoupling the photosensor and the stimulus electrode [30-32]. Image data and power are transmitted wirelessly from an external unit to the retinal implant. The other method, which we have adopted and reported in this paper, is where the image sensor and stimulus electrode array are located on the same chip while power is supplied wirelessly [33-35]. Yet another approach involves only passive devices whereby no external power is required [36]. Also, it has been shown that spike trains, and not a constant amplitude stimulation, either electrically or optically, is the preferred method for eliciting response from the retinal cells [37]. Based on this fact, we are developing the subretinal implant chip using the pulse frequency modulation (PFM) photosensor circuit [33]. With the PFM photosensor, we can implement photosensitivity adaptation similar to the mammalian retina [38]. This was demonstrated in our previous work [39]. Image processing based on the output pulse of the PFM circuit has been shown [40]. Our aim is to develop a new functional device that captures the image that falls onto the retina and deliver the necessary spatial and temporal electrical stimulus to the retina cells. To this end, we are developing a CMOS sensor chip for use as a subretinal implant device.

1.2 Aim and Methodology

The aim of this work is to explore the use CMOS image sensors for in vitro and in vivo imaging, as well as capability for electrical stimulation of tissue. In the course of our work,

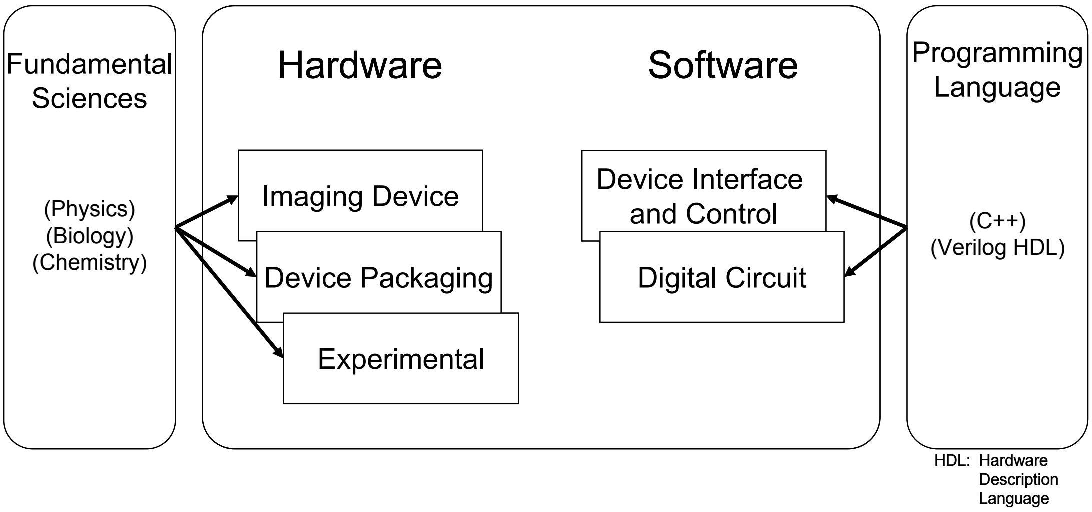

Fig. 1.2 Overview of approach to develop imaging devices for medical and scientific research.

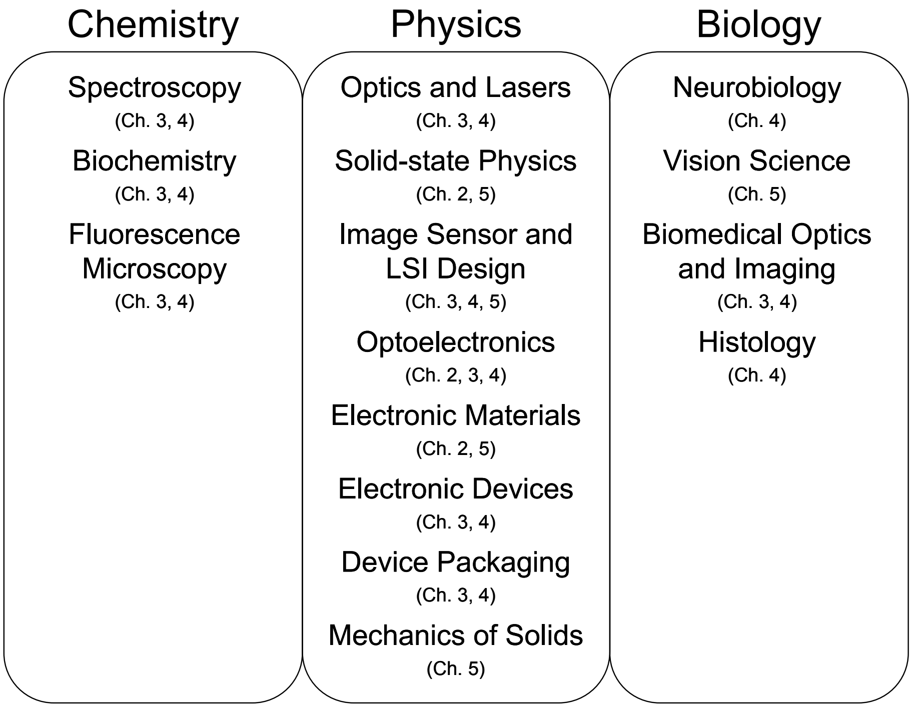

Fig. 1.3 Multidisciplinary science applied into this research work.

we have identified several areas that are needed in the development the CMOS image sensor as shown in the diagram in Fig. 1.2. Generally, development work lies on building the hardware and programming and interfacing the software. Furthermore, the work covered in this investigation necessitates a multidisciplinary approach due to the scope of the applications involved. By combining various disciplines in physics, chemistry and biology we have achieved this goal. For example, an understanding of the physics underlying device characterization; widespread use of electronics in device layout and design, a strong grasps of the mechanics involved in actual implementation, and the chemistry and biology involved all played their roles. Fig. 1.3 shows the involvement of the sciences required during the course of this work. Each field is specified and its location with reference to each chapter is given.

1.3 Thesis Outline

This thesis is organized into six chapters. Each chapter starts with a short summary detailing its contents. The entire thesis contains details of my work leading to the development of CMOS image sensors that are capable of on-chip fluorescence imaging and generation of electrical stimulus current.

In Chapter 2, various advantages by utilizing the CMOS imaging technology for biomedical imaging are described. Many strategies concerning the use of CMOS image sensors are investigated. The pulse modulation photosensing scheme is explained. Fundamental issues involving device characteristics and applications for bioimaging are raised and answered. These include device-tissue interaction and light transport in biological tissue.

In Chapter 3, the use of a CMOS photosensor for fluorescence detection is described. In particular static and dynamic fluorescence detection is demonstrated. A special packaging technique is developed to enable an optical configuration for on-chip fluorescence imaging using the CMOS image sensor. The packaging process is described in detail this chapter. Fluorescence imaging results obtained using the fully packaged sensor chip are presented. The image sensor sensitivity and on-chip imaging resolution are also investigated.

In Chapter 4, the work leading to in vitro and in vivo imaging is described. Here, the packaged CMOS image sensor is used for fluorescence imaging of a mouse brain. Both in vitro imaging of the mouse brain slice and in vivo imaging of the intact mouse brain are demonstrated. Also, a special brain tissue phantom is developed to verify in situ fluorescence imaging for verification of in vivo imaging, and as a platform to test model fluorescence reactions. The results in this chapter represent the first reported instance of in vivo imaging and quantitative fluorometric measurements inside the live and intact mouse brain.

Chapter 5 expands upon the imaging capability of the CMOS sensor by demonstrating electrical stimulus capability. This shows the potential use of the CMOS sensor apart from the normal imaging purposes. I have successfully demonstrated biphasic pulse generation above the threshold levels of the human retina at 500 μA. Also, due to the application of the image sensor as a retinal prosthesis inside the human eye, the effect of mechanical strain on the CMOS devices is studied.

Finally, Chapter 6 concludes this thesis by reviewing the results obtained and discussing the impact of this work to the scientific community. Suggestions for potential future work are carefully raised and elaborated.

References

[1] E. Zrenner, “Will retinal implants restore vision?” *Science*, vol. 295, pp. 1022-1025, Feb. 2002.

[2] J. F. Bell III, et al., “Pancam multispectral imaging results from the opportunity rover at meridiani planum,” *Science*, vol. 306, pp. 1703-1709, Dec. 2004.

[3] L. Melton, “The big picture,” *Nature*, vol. 437, pp. 775-779, Sep. 2005.

[4] T. Etoh, H. Mutoh, “High-speed imaging device,” U.S. Patent 6 972 795, Dec. 2005.

[5] G. J. Tearney, M. E. Brezinski, B. E. Bouma, S. A. Boppart, C. Pitris, J. F. Southern, J. G. Fujimoto, “In vivo endoscopic optical biopsy with optical coherence tomography,” *Science*, vol. 276, pp. 2037-2039, Jun. 1997.

[6] J. R. Janesick, “Lux transfer: CMOS versus CCD,” in *Proceedings of SPIE*, Sensors and Camera Systems for Scientific, Industrial, and Digital Photography Applications III, M. M. Blouke, J. Canosa, N. Sampat, ed.s, Apr. 2002, vol. 4669, pp. 232-249.

[7] T. Lulé, S. Benthien, H. Keller, F. Mütze, P. Rieve, K. Seibel, M. Sommer, M. Böhm, “Sensitivity of CMOS based imagers perspectives,” *IEEE Trans. Electron Devices*, vol. 47, pp. 2110-2122, Nov. 2000.

[8] H. -S. Wong, “Technology and device scaling considerations for CMOS imagers,” *IEEE Trans. Electron Devices*, vol. 43, pp. 2131-2142, Dec. 1996.

[9] E. Culurciello, R. Etienne-Cummings, K. A. Boahen, “A biomorphic digital image sensor,” *IEEE J.Solid-State Circuits*, vol. 38, pp. 281-294, Feb. 2003.

[10] D. Stoppa, A. Simoni, L. Gonzo, M. Gottardi, G.-F. Dalla Betta, “Novel CMOS image sensor with a 132-dB dynamic range,” *IEEE J. Solid-State Circuits*, vol. 37, pp. 1846-1852, Dec. 2002.

[11] P. -F. Rüedi, P. Heim, F. Kaess, E. Grenet, F. Heitger, P. -Y. Burgi, S. Gyger, P. Nussbaum, “A 128 × 128 Pixel 120-dB Dynamic-Range Vision-Sensor Chip for Image Contrast and Orientation Extraction,” *IEEE J. Solid-State Circuits*, vol. 38, pp. 2325-2333, Dec. 2003.

[12] A. Mioni. (Mar. 1997). *Vision Chips or Seeing Silicon*. (3rd rev.) [Online]. Available: http://aaron.eleceng.adelaide.edu.au.

[13] Y. Oike, “Smart Image Sensors and Associative Engines for Three Dimensional Image Capture,” *PhD dissertation*, The University of Tokyo, Dec. 2004.

[14] F. Helmchen, M. S. Fee, D. W. Tank, W. Denk, “A miniature head-mounted neurotechnique two-photon microscope: high resolution brain imaging in freely moving animals,” *Neuron*, vol. 31, pp. 903-12, Sep. 2001.

[15] J. -M. Jang, H. -J. Shin, S. -W. Hwang, E. -G. Yang, D. -S. Yoon, T. -S, Kim, J. -Y. Kang, “Miniaturized fluorescence detection system to remove background noise of the incident light using micro mirror and lens,” *Sens. Actuators B*, vol. 108, pp. 993-1000, Jul. 2005.

[16] D. M. Rector, G. R. Poe, P. Redgrave, R. M. Harper, “A miniature CCD video camera for high-sensitivity light measurements in freely behaving animals,” *J. Neurosci. Meth.*, vol. 78 pp. 85-91, Dec. 1997.

[17] C. Hagleitner, A. Hierlemann, D. Lange, A. Kummer, N. Kerness, O. Brand, H. Baltes, “Smart single-chip gas sensor microsystem,” *Nature*, vol. 414 , pp.293-296, Nov. 2001.

[18] D. -S. Kim, Y. -T. Jeong, H. -J. Park, J. -K. Shin, P. Choi, J. -H. Lee, G. Lim, “An FET-type charge sensor for highly sensitive detection of DNA sequence,” *Biosens. Bioelectron.*, vol. 20, pp. 69-74, Jul. 2004.

[19] P. Swanson, R. Gelbart, E. Atlas, L. Yang, T. Grogan, W. F. Butler, D. E. Ackley, E. Sheldon, “A fully multiplexed CMOS biochip for DNA analysis,” *Sens. Actuators B*, vol. 64, pp. 22-30, Jun. 2000.

[20] N. Y. Shen, Z. Liu, B. C. Jacquot, B. A. Minch, E. C. Kan, “Integration of chemical sensing and electrowetting actuation on chemoreceptive neuron MOS (CvMOS) transistors,” *Sens. Actuators B*, vol. 102, pp. 35-43, Sep. 2004.

[21] K. Sawada, T. Ohshina, T. Hizawa, H. Takao, M. Ishida, “A novel fused sensor for photo- and ion-sensing,” *Sens. Actuators B*, vol. 106, pp. 614-618, May 2005.

[22] P. A. Hammond, D. Ali, D. R. S. Cumming, “Design of a single-chip pH sensor using a conventional 0.6-μm CMOS process,” *IEEE Sens. J.*, vol. 4, pp. 706-712, Dec. 2004..

[23] T. Tokuda, A. Yamamoto, K. Kagawa, M. Nunoshita, J. Ohta, “A CMOS image sensor with optical and potential dual imaging function for on-chip bioscientific applications,” *Sens. Actuators A*, vol. 125, pp. 273-280, Jan. 2006.

[24] E. K. Bolton, G. S. Sayler, D. E. Nivens, J. M. Rochelle, S. Ripp, M. L. Simpson, “Integrated CMOS photodetectors and signal processing for very low-level chemical

sensing with the bioluminescent bioreporter integrated circuit," *Sens. Actuators B*, vol. 85, pp. 179-185, Jun. 2002.

[25] R. A. Yotter, M. R. Warren, D. M. Wilson, "Optimized CMOS photodetector structures for the detection of green luminescent probes in biological application," *Sens. Actuators B*, vol. 103, pp. 43-49, Sep. 2004.

[26] U. Lu, B. C. -P. Hu, Y. -C Shih, C. -Y. Wu, Y. -S. Yang, "The design of a novel complementary metal oxide semiconductor detection system for biochemical luminescence," *Biosens. Bioelectron.*, vol. 19, pp. 1185-1191, May 2004.

[27] K. Salama, H. Eltoukhy, A. Hassibi, A. E. Gamal, "Modeling and simulation of integrated bioluminescence detection platforms," *Biosens. Bioelectron.*, vol. 19, pp. 1377-1386, Jun. 2004.

[28] J. R. Heckenlively, "The diagnosis and classification of retinitis pigmentosa," in *Retinitis Pigmentosa*, J. R. Heckenlively, ed. Philadelphia: JB Lippincott Co., 1988, pp. 21-23.

[29] E. Margalit, M. Maia, J. D. Weiland, R. J. Greenberg, G. Y. Fujii, G. Torres, D. V. Piyathaisere, T. M. O'Hearn, W. Liu, G. Lazzi, G. Dagnelie, D. A. Scribner, E. de Juan Jr, M. S. Humayun, "Retinal prosthesis for the blind," *Surv. Opthalmol.*, vol. 47, pp. 335-356, Jul. 2002.

[30] M. S. Humayun, E. de Juan Jr., J. D. Weiland, G. Dagnelie, S. Katona, R. Greenberg, S. Suzuki, "Pattern electrical stimulation of the human retina," *Vision Res.*, vol. 39, pp. 2569-2576, Jul. 1999.

[31] M. Schwarz, R. Hauschild, B. J. Hosticka, J. Huppertz, T. Kneip, S. Kolnsberg, L. Ewe, H. K. Trieu, "Single-chip CMOS image sensors for a retina implant system," *IEEE Trans. Circuits Syst. II*, vol. 46, pp. 870-877, Jul. 1999.

[32] W. Liu, K. Vichienchom, M. Clements, S. C. DeMarco, C. Hughes, E. McGucken, M. S. Humayun, E. de Juan, J. D. Weiland, R. Greenberg, "A neuro-stimulus chip with telemetry unit for retinal prosthetic device," *IEEE J. Solid-State Circuits*, vol. 35, pp. 1487-1497, Oct. 2000.

[33] J. Ohta, N. Yoshida, K Kagawa, M. Nunoshita, "Proposal of application of pulsed vision chip for retinal prosthesis," *Jpn. J. Appl. Phys.*, vol. 41, pp. 2322-2325, Apr. 2002.

[34] A. Dollberg, H. G. Graf, B. Höfflinger, W. Nisch, J. D. Schulze Spuentrup, K. Schumacher, E. Zrenner, "A fully testable retinal implant," in *Proc. BioMED*, Jun. 2003, pp. 255-260.

[35]D. Ziegler, P. Linderholm, M. Mazza, S. Ferazzutti, D. Bertrand, A.M. Ionescu, Ph. Renaud, "An active microphotodiode array of oscillating pixels for retinal stimulation," *Sens. Actuators A*, vol. 110, pp. 11-17, 2004.

[36] A. Y. Chow, M. T. Pardue, V. Y. Chow, G. A. Peyman, C. Liang, J. I. Perlman, N. S. Peachey, "Implantation of silicon chip microphotodiode arrays into the cat subretinal space," *IEEE Trans. Neural Syst. Rehab. Eng*., vol. 9, pp. 86-95, Mar. 2001.

[37] A. Stett, W. Barth, S. Weiss, H. Haemmerle, E. Zrenner, "Electrical multisite stimulation of the isolated chicken retina," *Vision Res.*, vol. 40, pp. 1785-1795, Jun. 2000.

[38] B. Sakmann, O.D. Creutzfeldt, "Scotopic and mesopic light adaptation in cat's retina," *Pfugers Arch.*, vol. 313, pp. 168-185, 1969.

[39] K. Kagawa, K. Isakari, T. Furumiya, A. Uehara, T. Tkuda, J. Ohta, M. Nunoshita, "Pixel design of a pulsed CMOS image sensor for retinal prosthesis with digital photosensitivity control," *Electron. Lett*., vol. 39, pp. 419-421, Mar. 2003.

[40] K. Kagawa, K. Yasuoka, D. C. Ng, T. Furumiya, T. Tokuda, J. Ohta, M. Nunoshita, "Pulse-domain digital image processing for vision chips applicable to low-voltage operation in deep-submicron technologies," *IEEE J. Select. Topics Quantum Electron.*, vol. 10, pp. 816-828, Jul. 2004.

Chapter 2

CMOS Imaging Technology for Biological Applications

In this chapter, the use of CMOS image sensors is discussed especially with relevance to bioimaging applications. A comparison with other imaging technologies is made. The advantage of using CMOS image sensors is then described. Next the CMOS characteristic, in particular the photocurrent generation is described in detail. Various read-out methods like the active pixel sensor and pulse modulation methods are then discussed. Because a CMOS device is used in an environment where there is interaction between the device and the measured object, device effectiveness needs to be addressed. In this work, light transport inside biological tissue is discussed in relation to the on-chip imaging configuration.

Keywords: CMOS, active pixel sensor, pulse modulation, device-tissue, photo-electrical, light transport

2.1 Introduction

Photosensors are the most important element of imaging devices as described in the previous chapter. Incident photons onto the photosensor are converted into electrons by the photosensors. Hence, by using a photosensor and measuring the number of electrons generated, a quantitative number related to the incident photons can be known or sensed. Table 2.1 lists three popular photosensor technologies and compares their performances.

Among these photosensors, the CCD-type is a mature technology that has been developed and perfected over the years. In the original version of this device, electrons converted from the incident photons are transferred or read out by shifting the charges in a serial manner down the entire area of the CCD. To date, many different versions of CCDs exist in the form of intensified charge coupled device (iCCD), electron multiplying charge coupled device (EMCCD), or frame transfer charge coupled device (ft-CCD). These devices are used in lower end applications in consumer goods such as digital cameras and scanners and more demanding higher end applications in scientific tools found in spectrophotometers and fluorescence microscopes. Through specialized process, a back illuminated CCD can reach an extremely high quantum efficiency up to 90% [3].

Another type of photodetector is the photomultiplier tube (PMT). This device has extremely high photosensitivity reaching the limit of single photon detection. However, because of its size and power requirements, the use of PMTs are reserved for the most specialized cases like astronomy, where performance and cost are major concerns. Furthermore, due to the construction of the device which includes a vacuum tube, implementation of a compact arrayed device remains a technological hurdle.

In comparison to CCD or PMT, the CMOS photosensor is a relatively new technology.

Table 2.1 Comparison between three currently available photosensing technologies.

	Photosensor		
	PMT	CCD	CMOS
Efficiency and detection range [2]	single photon (115 -1400 nm)	up to 90% (200 -1200 nm)	up to 50% (190 -1000 nm)
Response time [2]	1 ns	10 ns	100 ns
Dark current [1,2]	0.01 nA	10 pA/cm^2	30 pA/cm^2
System integration and issues	• bulky and expensive • colour and image sensing difficult	• moderately expensive with saturated market	• system integration and miniaturization with high potential for bioimaging applications

Although fundamentally, both CCD and CMOS photosensor utilize the photo-generated electrons, a slight difference in operation exists. For the CMOS photosensor, the electrons discharge out of the photodiode capacitor which is then sensed by measuring the voltage across the capacitor. A consequence of this is a relatively high noise in the output signal. Also, because, the CMOS photosensor is fabricated using the same process as other semiconductor devices, it is often not optimized for photosensitivity. For example, a standard CMOS line for mitigating CMOS latchup can lead to low red response. Similarly, the process for creating dense, short-gate length CMOS logic chips cause high dark current and low green response. These factors combine which results in lower performance for CMOS image sensors. However, because the CMOS photosensor is integrated with the readout circuitry, a single chip that includes photon sensing, signal amplification, processing and readout is possible. Also, improvements from many fronts are being proposed and developed to give extra leverage to the CMOS image sensors. These include the use availability of specialized p-i-n photodiodes [4], special processing circuits [5], and low voltage operation [6].

In terms of image quality and sensitivity, the CMOS image sensor has not reached the levels offered by other mature competing technologies. For any application, there will be a trade-off and a need to balance between capabilities and advantages offered. But because CMOS technology has been shown to be capable of many exciting possibilities, it is especially suited for the application that we are focusing on as described in Chapter 1. These advantages will be as will be explored in §2.2 below.

2.2 Advantages of CMOS Imaging Technology

CMOS technology is capable of producing a system-on-chip device whereby the signal conditioning and processing, memory core and communication module can be implemented onto a single device. This has been the driving force for the development of better performance computation chip. Coupled with the capability of photon detection, rapid development of CMOS image sensors has taken place in the last two decades. Recently, it has been found that the sensing capability of CMOS-based devices goes beyond light sensing. Recent development of CMOS-based devices have shown that the benefit of using CMOS technology extends beyond those functions. It has been reported that the CMOS device is capable of measuring pH, ion, electrical potential, temperature, and other parameters [7-11]. Because an array of these detectors can be built, high resolution imaging in these parameters can be performed. This is the main strength of the CMOS sensor compared to other technologies. When various detector pixels are combined onto a single chip, a truly integrated single-chip can be realized [12, 13].

The advantages of CMOS imaging technology can be summarized as follow;

- high spatial and temporal resolution optical imaging
- potential for multi-parameter sensing which includes gas, temperature, pH, ions, and electrical potential on a single device [7-11]

- multi-site electrical stimulation capability [14, 15],
- wireless operation which benefits observation of freely-moving animals [16, 17].

These advantages can be utilized to fabricate CMOS based devices that have multi functions on a single chip. In this work, these advantages are explored to realize a CMOS device that is capable of on-chip imaging. Here, on-chip imaging refers to the use of a single device for imaging, without any optics. In other words, the sample is in contact with the imaging device. In this configuration, imaging can be extended to other parameters like electrical potential and electrical stimulus. When this configuration is used, experiments are no longer limited to space constraints of the microscope or limited to use in the laboratory.

2.3 CMOS Photodiode

2.3.1 Photodiode Characteristic

The main element in the CMOS imaging device that converts incident photons to electrical signal (phtotocurrent) is the photodiode. The photodiode consists of a semiconductor p-n junction. There are a number of different p-n junctions available in standard the CMOS technology. In this work, I have studied two photodiode structures; the n-well/p-sub and p-diff/n-well structure. These structures are available in all standard CMOS technologies, from the first generation process, down to the most advanced sub-micron technology. These photodiodes are shown in Fig. 2.1.

The detailed operation of the photocurrent generation of the photodiode (PD) can be found in standard textbooks on semiconductor devices [18]. Basically, near the p-n junction the silicon becomes depleted of electrical charges. This is known as the *depletion region* as shown in

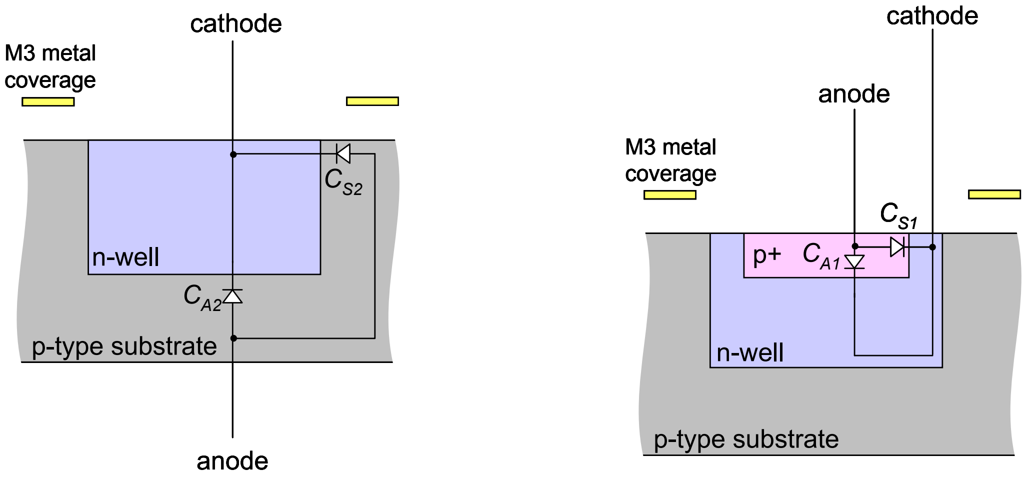

(A) (B)

Fig. 2.1 Diagrammatic sectional profile of (A) n-well/p-sub, and (B) p-diff/n-well photodiode.

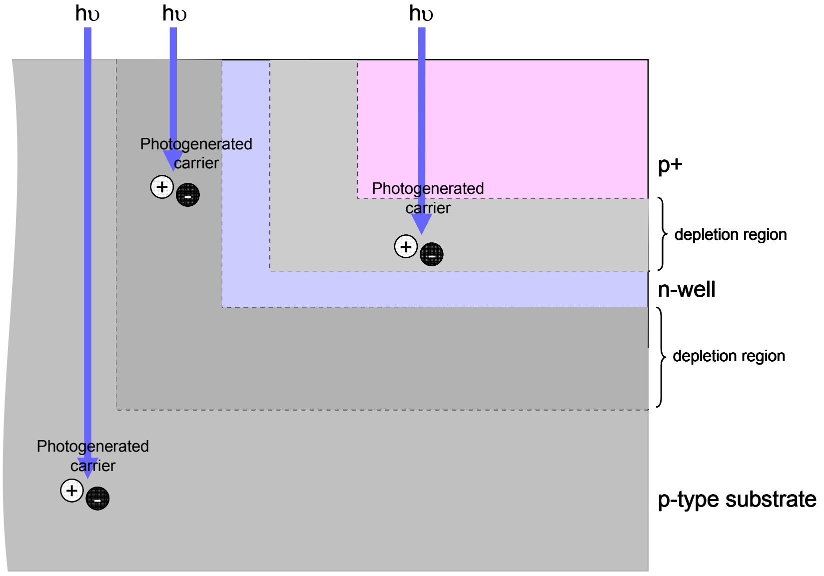

Fig. 2.2 Generation of carrier at the depletion region is swept by the field potential and contribute to the photocurrent. Beyond the depletion region, the photogenerated carriers do not to contribute to the photocurrent.

Fig. 2.2. The depth of the depletion region can be varied by applying a reverse bias voltage across the junction. When the depletion region reaches the back of the diode the photodiode is said to be *fully depleted*. This region is important to PD performance since most of the sensitivity to radiation originates there. Also, the capacitance of the p-n junction depends on the depth of this variable region. Increasing the bias voltage increases the depth of this region and lowers the junction capacitance until the fully depleted condition is achieved. This capacitance is also a function of the resistivity of silicon used and active area size.

When a photon of incident light is irradiated onto the active area, an electron-hole pair is generated. The electrons and holes are separated electrons passing to the *n* region and holes to the *p* region. This results in a photocurrent generated by light. This current is further divided into generation recombination limited current and diffusion limited current due to the different mechanism whereby the current is generated [19]. The migration of electrons and holes to their respective regions is called the *photovoltaic effect*. When no bias voltage is applied, the silicon photodiodes operate as a current generator. The photodiode has two terminal electrodes, a cathode and an anode, and it has a low forward resistance (anode positive) and high reverse resistance (anode negative). Normal biased operation of most photodiodes calls for negative biasing the active area of the device which is the anode or positive biasing the device backside which is the cathode. In the photovoltaic and zero bias modes, the generated current or voltage is in the diode forward direction. Hence the generated polarity is opposite to that required for the biased mode.

The relationship between the photodiode junction capacitance, C_j, bias voltage, V_b and dopant concentrations N_a, N_d are defined as follow. The junction capacitance,

$$C_j = \sqrt{\frac{q \cdot \varepsilon_{Si}}{2\left(\phi_j + V_b\right)} \frac{N_a \cdot N_d}{N_a + N_d}}, \tag{2.1}$$

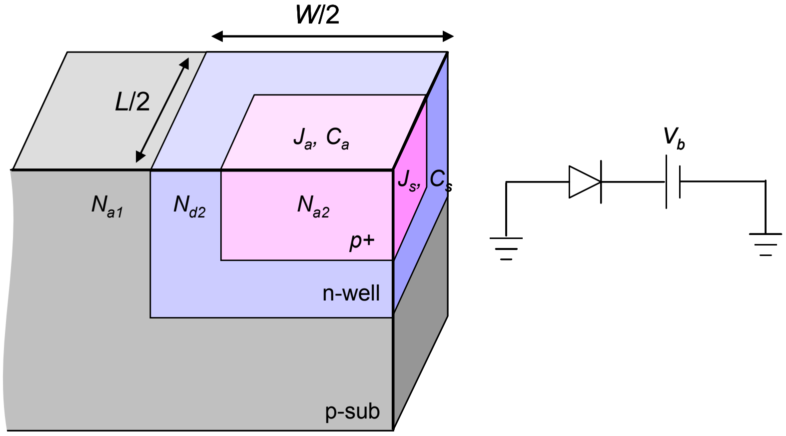

Fig. 2.3 Junction capacitance, *C* and dopant concentration, *N* for p-diff/n-well and n-well/p-sub PD. The bias voltage, V_b is applied to the cathode terminal as shown in the quarter cross sectional view of the photodiode. The photodiode width, *W* and length, *L* is defined as shown.

and the junction potential,

$$\phi_j = V_{ther} \ell n \left(\frac{N_a \cdot N_d}{n_i^2} \right). \tag{2.2}$$

where, electron charge, $q = 1.6 \times 10^{-19}$ C, thermal voltage $V_{ther} = 26$ mV at 300 K, Boltzman constant, $k = 1.3 \times 10^{-23}$ J/K, permittivity of Silicon, $\varepsilon_{\mathrm{Si}} = 1.04 \times 10^{-12}$ F/cm, and silicon intrinsic carrier, $n_i = 1.5 \times 10^{10}$ cm^{-3} at 300 K. Here, the dopant concentrations, N_a and N_d refer to the n- and p-type dopant concentrations, respectively as shown in Fig. 2.3. These relationships enable us to calculate the dopant concentrations from the process parameters [20]. Furthermore, the capacitance, C_{PD} and leakage (dark) current, I_D for the photodiodes can be calculated using the following expressions.

$$C_{PD} = (W \cdot L) \frac{C_a}{\left(1 + \frac{V_b}{\phi_j}\right)^{m_a}} + 2(W + L) \frac{C_s}{\left(1 + \frac{V_b}{\phi_j}\right)^{m_s}}, \tag{2.3}$$

$$I_D = J_s (W \cdot L) + J_a \cdot 2(W + L). \tag{2.4}$$

For a photodiode with width, *W* and length, *L* equals to 50 μm, the capacitance and leakage currents for the p-diff/n-well and n-well/p-sub photodiode were calculated[*].

2.3.2 Responsivity

The p-diff/n-well and n-well/p-sub CMOS photodiodes were fabricated and responsivity measurements were measured. Fig. 2.4 shows the responsivity spectra of these photodiodes. The measurement was made across the wavelength ranging from UV (400 nm) to visible region (700 nm). From the result it can be seen that the responsivity of the n-well/p-sub photodiode is comparatively higher for most of the measured wavelength range. Because I am interested in applying the photodiodes to the fluorescence detection as well as the visible light detection, the n-well/p-sub photodiode was selected for all subsequent sensor designs. In this evaluation work,

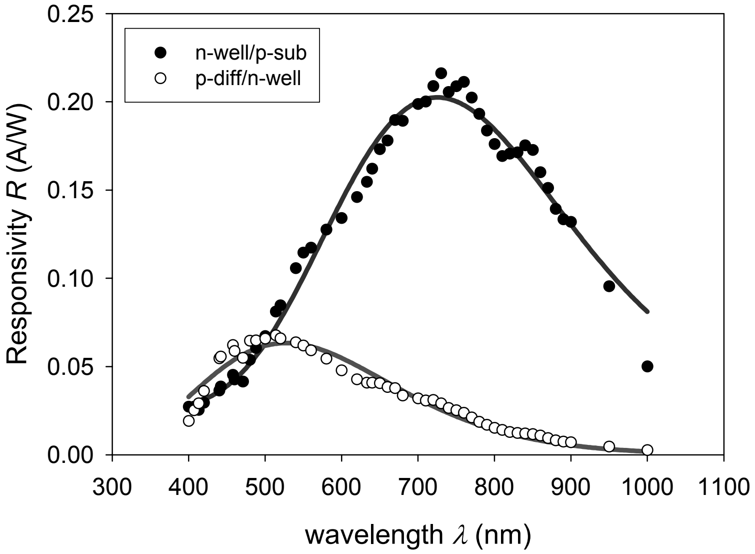

Fig. 2.4 Responsivity spectra of n-well/-psub and p-diff/n-well photodiodes.

---

[*] Due to the non-disclosure agreement (NDA) signed with the foundry, the process parameters and related results cannot be shown here.

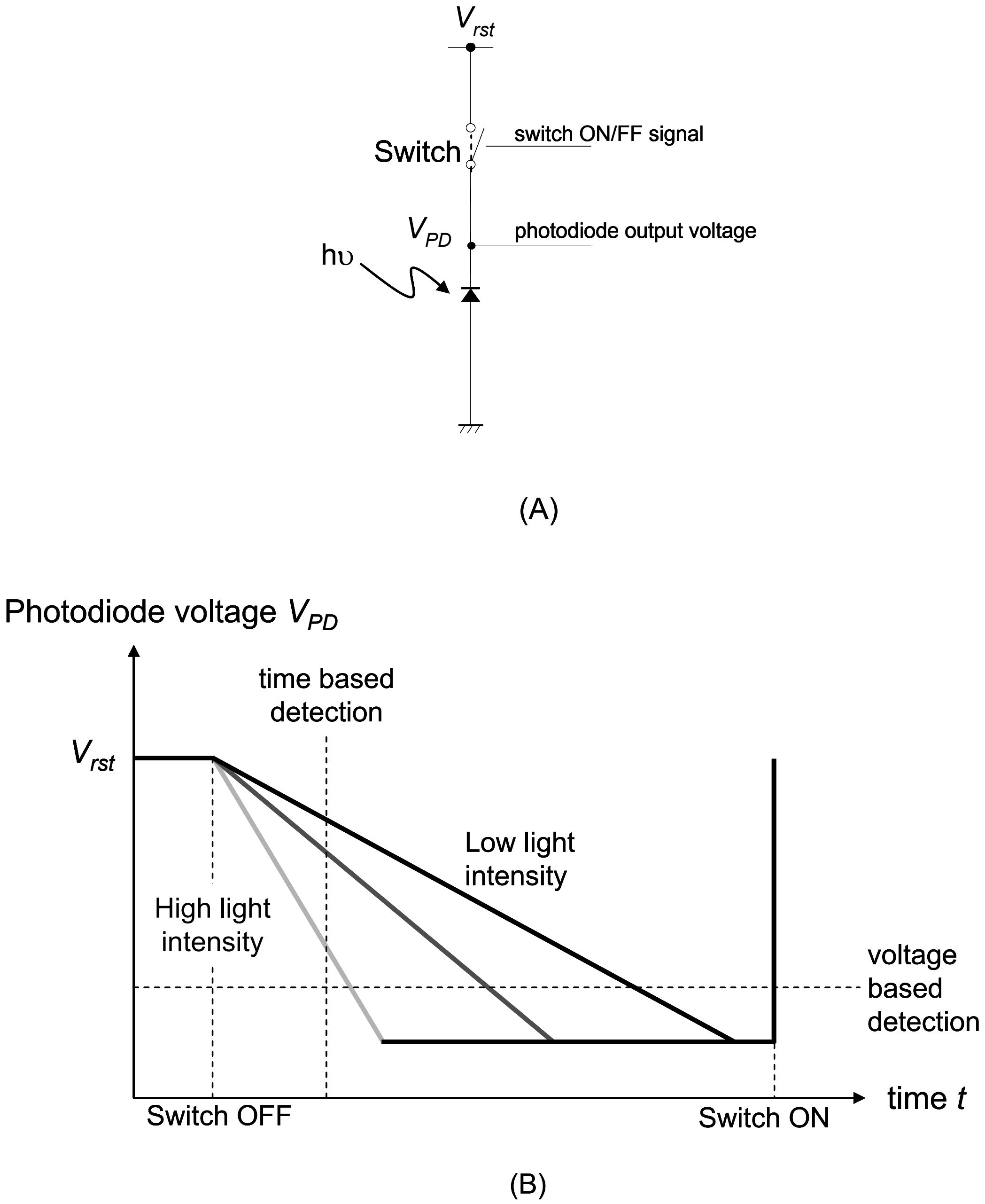

Fig. 2.5 (A) Photodiode connected to voltage source V_{rst} via a switch. (B) Rate of change of photodiode voltage V_{PD} after the switch disconnects depending on incident light intensity.

although the 0.6 μm CMOS technology was used, a similar trend can be extrapolated for the 0.35 μm deeper sub-micron technology as confirmed by simulation.

2.3.3 Readout Methods

As mentioned earlier, photosensing for the CMOS PD is achieved by measuring the photodiode voltage across its terminals as the photogenerated currents discharge its capacitance. In order to use the PD as a photosensor, a switch is needed to charge up the photodiode capacitance which connects it to a source voltage and then disconnect as shown in Fig. 2.5 (A). After the switch is turned OFF, photogenerated current will discharge the photodiode capacitance. A constant light intensity, Φ will be converted to a steady photocurrent, i_L at a certain efficiency called the quantum efficiency, η.

The PD output can be measured in two ways; time-based and reference voltage-based readout method as shown in Fig. 2.5 (B). For the former, the V_{PD} is measured at a specified time interval. This method has the flexibility of utilizing a constant clock for the readout signal. The drawback here is the need for accurately measuring the photodiode voltage using a form of an analog-to-digital (A/D) converter. Hence the accuracy and resolution of the reading is dependent on the A/D used. One way to implement this readout method is by using a three transistor active pixel sensor (APS) circuit as shown in Fig. 2.6 (A). To conserve space and reduce fixed pattern noise, the A/D converter is often located on the column amplifier (not shown). Fig. 2.6 (B) shows how the APS circuit can be implemented into a 2D array.

The other measurement method is by constantly comparing the V_{PD} to the reference voltage, V_{ref}. Once V_{PD} falls below V_{ref}, a pulse is produced. The advantage of this method is the absence of the A/D converter which takes up a lot of space. A comparator circuit on the other hand can be implemented using a differential amplifier which is less complicated and much smaller. Also,

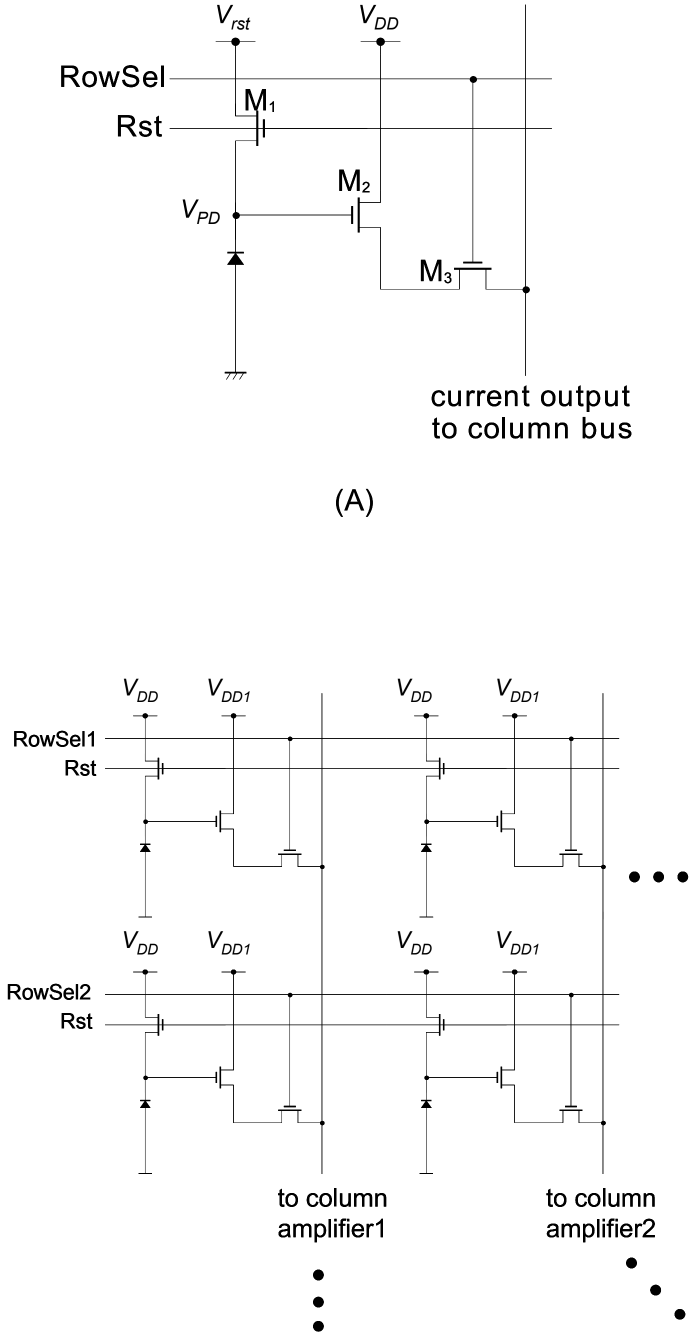

(A)

(B)

Fig. 2.6 (A) Three-transistor APS circuit. (B) Image sensor circuit based on three transistor APS circuit.

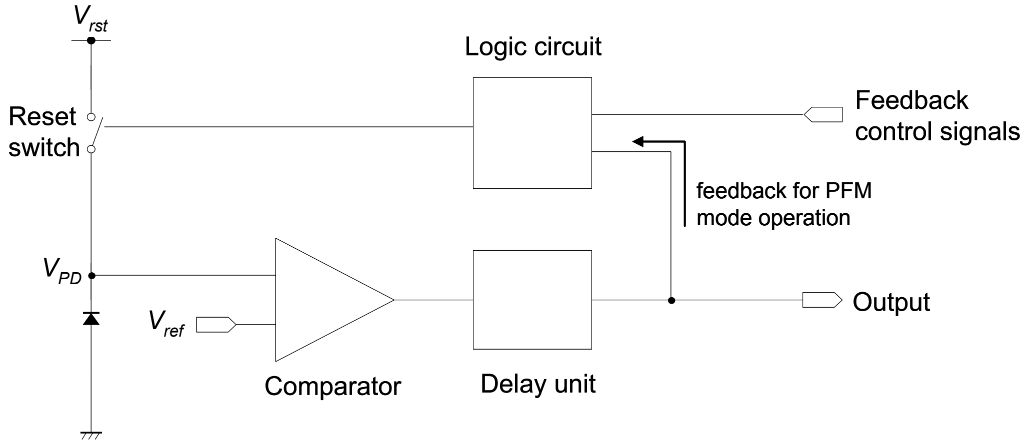

Fig. 2.7 General schematic of the pulse modulation circuit.

the output resolution is independent of the type of A/D converter used. This has the advantage of increasing the measured dynamic range. Hence low light intensity detection will benefit from this method. However, the drawback of this method is an increase in time needed to detect the output pulse when a low light intensity is present. When implemented onto a 2D image sensing array, the readout speed of a single frame can be severely affected when using this method for low light intensity detection. Fig. 2.7 shows the general circuit whereby this method can be implemented. Because the output is in pulses, with duration or length of the pulse being modulated by the incident light, this method is often referred to as the pulse modulation sensing. This photosensing circuit can be further operated in two different modes; the pulse width modulation (PWM), and the pulse frequency modulation (PFM) modes. The difference in these methods are; for PWM, the reset signal is controlled by an external signal such that the reset interval is constant, much like for the APS case, whereas for the PFM mode, the reset signal is controlled by the photosensor output which is feedback. A delay unit is also used in the PFM

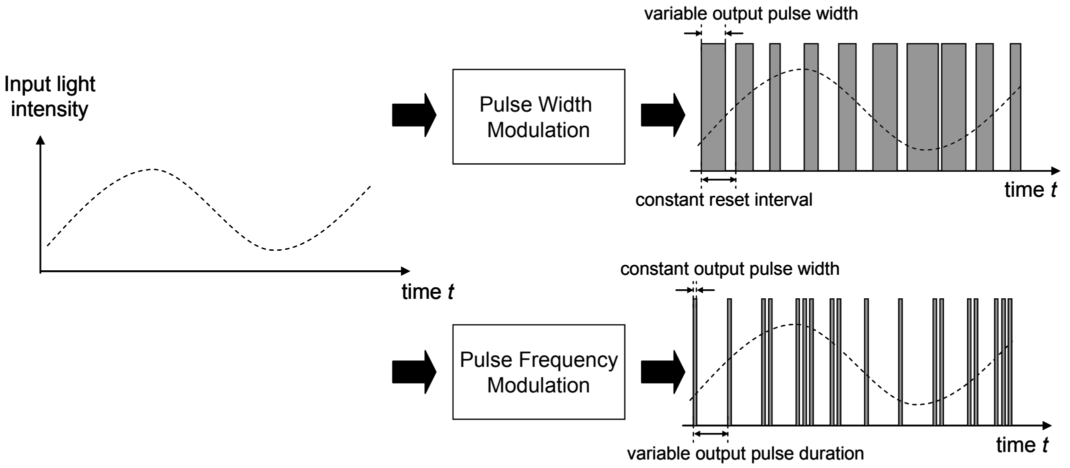

Fig. 2.8 Typical output from pulse width modulation and pulse frequency modulation circuit.

mode. The delay unit generates the same output as its input but shifted by a small amount of time. Its purpose here is to provide a constant output pulse width to ensure that the feedback signal is properly feedback to control the reset switch. The typical outputs from the PWM and PFM signal are shown in Fig. 2.8. When given an input light with variable intensities, higher light intensity will result in shorter output pulse widths for the PWM mode and higher pulse count in the PFM mode. The actual implementation and characteristics of the PWM and PFM circuits will be further described in Chapter 3 and Chapter 5.

2.4 On-chip imaging

As described earlier, the CMOS chip is capable of multiple of parameter sensing. In order to take advantage of these sensing capabilities, the sensor chip needs to be in contact with the object to be measured. Because the separation between the sensor surface and the object is

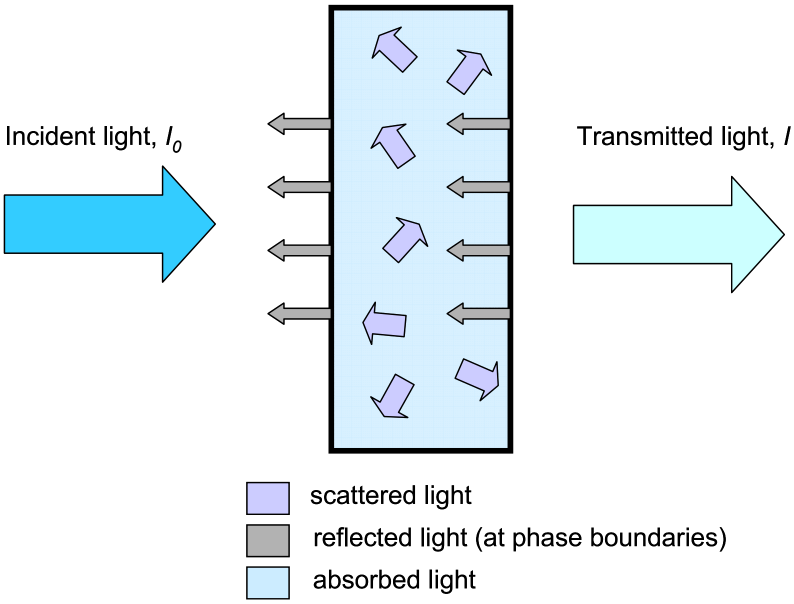

Fig. 2.9 Interaction of incident light with matter. The incident light is reflected, scattered and absorbed.

negligible, I call this on-chip imaging. In this imaging configuration, the subject usually takes the form of a liquid, or solid. The sensing parameters encountered in this work are mainly in the light domain. Hence, the proper analysis of light paths through different media will be discussed; When light is incident onto matter, it is scattered, reflected, and absorbed as shown in Fig. 2.9. In this work, I focus on light propagation through a highly absorbing medium such as a liquid and a highly scattering and reflective solid medium such as biological tissue. Although a proper analysis would require the treatment using electromagnetic radiation and its interactions with matter, here I focus on the macro model whereby actual measurable quantities and their relationships are studied.

2.4.1 Light Propagation in Liquid

I have studied the light propagation mechanism through liquids for the development of on-chip fluorescence imaging. This will help in measurement of the concentration of

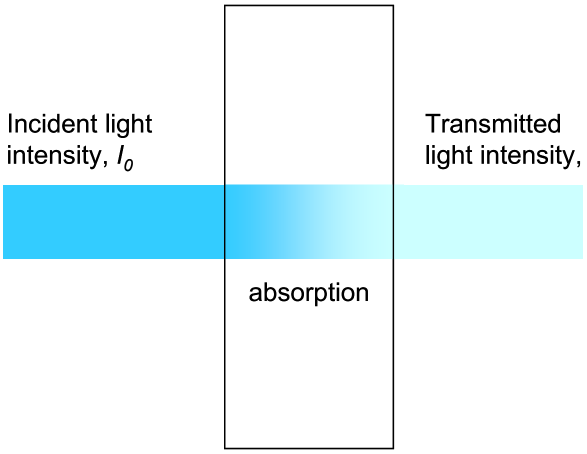

Fig. 2.10 Propagation of light through absorbing media such as liquid

fluorophore present. The main mechanism for light attenuation through a solution or molecular disperse media is mainly by absorption as shown in Fig. 2.10. The basis for light absorption can be explained by the fact that the incident photon frequency matches the frequency associated with the molecule's energy transition. The closer the wavelength frequencies match each other, the higher will be the absorption or energy transfer. In the macro model, the transmitted light intensity I and incident light intensity I_0 can be related using the Lambert-Beer law, which states that the absorbance,

$$A = \varepsilon \cdot b \cdot c, \tag{2.5}$$

where ε is the molar absorption coefficient with units ($M^{-1}cm^{-1}$), c is the molar concentration of absorbing species (in M), and b is the sample thickness (in cm). Also, it can be shown that the transmittance T which is defined by the ratio I/I_0, is related to absorbance by the following equation.

$$T = 10^{-A}. \tag{2.6}$$

Here, I would like to note that silicon is opaque under visible light as all the incidents photon energy is absorbed and converted to electron-hole pairs as described in §2.3.1.

2.4.2 Light Transport in Biological Tissue

When the medium consists of particles with size that is comparable to wavelengths of the incident light, scattering cannot be ignored. UV and visible light transport in biological tissues is an example of this case. Biological tissues are highly scattering and absorbing. The light transport in biological tissues plays an important role for many instruments in biological studies. By measuring and analyzing light scattering, information about the cells or tissues that underwent physiological changes can be obtained. This is because the change in cell physiology is reflected in its size or refractive index. In this work, an understanding of light propagation through tissue gives a basis whereby the propagation of excitation and fluorescence light in the brain can be quantified and estimated.

Although many theories exist to predict the transmission of light (fluence rates) in tissue, the accuracy of these models depends on the optical properties from measurement. The optical parameters which are most reported for biological tissue are; total attenuation coefficient, effective attenuation coefficient, effective penetration depth, absorption and scattering coefficient, and scattering anisotropic factor. These parameters can be obtained by using different measurement techniques and different models to explain the measured data [21].

2.4.3 Optical Property of the Brain

The biological tissue used in the scope of my work is the mammalian brain. One optical property used to quantify the penetration depth of light into tissues is the effective attenuation coefficient. This coefficient is the rate of decay of fluence rate (total light irradiance incident from all angles) in tissue regions far from light sources and boundaries, and is defined as,

$$\frac{I_0}{I_1} = e^{-\mu_{\text{eff}} \cdot b}, \tag{2.7}$$

where I_0 and I_l are the intensity of the incident and attenuated light, and b is the distance traveled. The coefficient can also be calculated as follows,

$$\mu_{eff}^2 = 3\mu_a\left[\mu_a + (1-g)\mu_s\right], \tag{2.8}$$

where the absorption coefficient, μ_a (cm^{-1}), scattering coefficient, μ_s (cm^{-1}), and anisotropy coefficient, g can be found by independent measurements of diffuse reflection, total transmission, and unscattered transmission of the tissue. It is a well known fact that photon penetration through the tissue is dependent on the wavelength of the light. This is directly observed when measurement is done to quantify the effective attenuation coefficient. Fig. 2.11 shows the relationship between μ_{eff} and wavelength λ based on measurement data of the cat brain in vivo [22]. When the coefficient values for wavelengths of 365 and 470 nm corresponding to the excitation and emission peak wavelength of AMC (see §3.3.2 for description on AMC) were calculated by interpolation and extrapolation from a linear fitting curve, the values are found to be μ_{eff1} = 51.8 cm^{-1} and μ_{eff2} = 38.3 cm^{-1}.

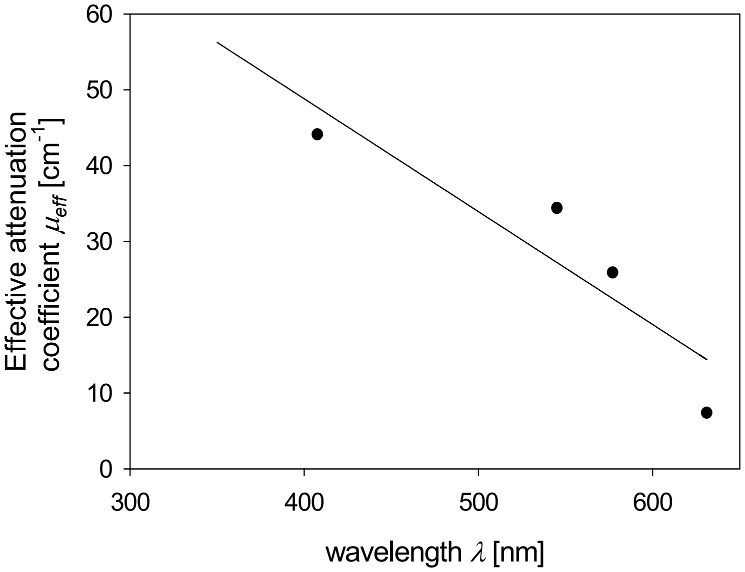

Fig. 2.11 Effective attenuation coefficient from in vivo cat brain measurement.

2.4.4 Estimation of Fluorophore Detection Inside Brain Tissue

Using the discussion above, I attempt to estimate the amount of detectable AMC fluorophore inside the brain. As a first approximation, the Beer-Lambert law is used. Excitation light is provided from the tip of a 500 μm diameter PMMA fiber.

From the photosensitivity measurement in Chapter 3 (Fig. 3.15), the minimum detectable light at λ = 470 nm is $I_{\lambda em1} = 10^{-7}$ W/cm^2. If the distance of AMC from the image sensor is $d_2 =$ 0.01 cm, and the effective attenuation coefficient is μ_{eff2} = 38.335 cm^{-1}, then the minimum required emission, $I_{\lambda em0}$ can be calculated from the following the relationship

$$\frac{I_{\lambda em0}}{I_{\lambda em1}} = e^{-\mu_{\text{eff2}} \cdot b_2}, \tag{2.9}$$

which is found to be 1.467 × 10^{-7} W/cm^2.

A rough estimate for the volume of AMC used is about 0.01 μl. Assuming the AMC taking the cubic shape, the side length, b is then equal 0.1 cm. From AMC sensitivity measurement (§ 3.4.3) the minimum detectable AMC is c = 10 μM. From [23], the molar extinction coefficient of AMC is ε = 25500 cm^{-1}M^{-1}. Hence, the excitation intensity that reaches the AMC, $I_{\lambda ex1}$ can be calculated from the following equation,

$$\frac{I_{\lambda em0}}{I_{\lambda ex1}} = 10^{-\varepsilon \cdot b \cdot c}. \tag{2.10}$$

This value is found to be about 1.556 × 10^{-7} W/cm^2.

Finally if the fiber is placed a distance of, d_1 = 0.1 cm from the AMC, the minimum excitation intensity needed can be found from the equation

$$\frac{I_{\lambda ex1}}{I_{\lambda ex0}} = e^{-\mu_{\text{eff1}} \cdot d_1}. \tag{2.11}$$

Due to the shorter wavelength of the excitation light compared to the emission light, the effective attenuation coefficient μ_{eff1} is expected to be higher and was found to be 51.78 cm^{-1}.

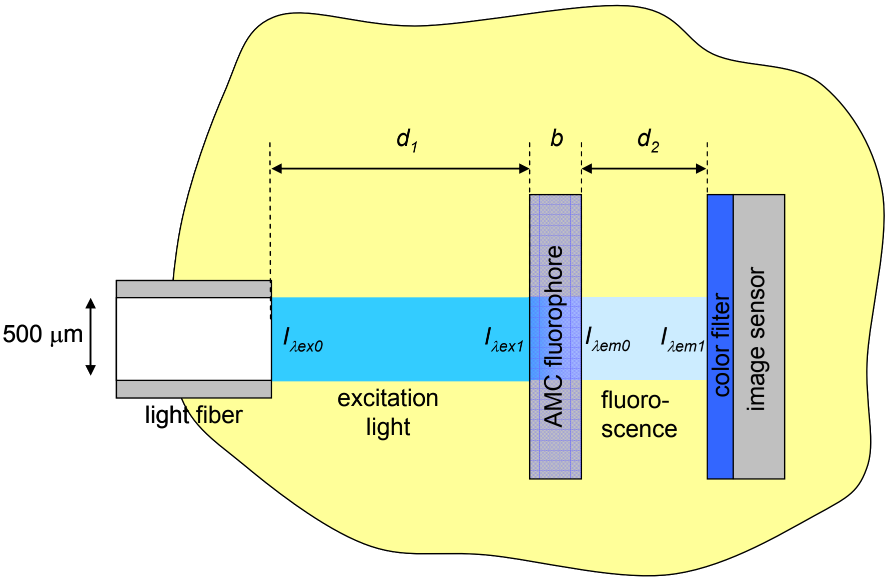

Fig. 2.12 Schematic of light transmission inside brain for first order estimation for AMC detection.

The excitation intensity, $I_{\lambda ex0}$ is then calculated to be 27.6 µW/cm^2. The required excitation intensity should exceed this value for possible detection of AMC. The excitation light, P from the 500 µm PMMA fiber was found to be about 400 nW @ 380 nm. The intensity is calculated from the equation,

$$I_{\lambda ex} = \frac{P}{A}, \tag{2.12}$$

where A is the cross sectional area of the fiber. From eq. (2.12) the intensity is found to be 203.7 µW/cm^2. Hence it can be concluded that the current setup of fiber and image sensor is capable of detecting 10 µM of AMC.

2.5 Summary

In this chapter, CMOS technology was compared to CCD and PMT. The advantages of building a CMOS based sensor were then described. This was followed by a discussion on the fundamental photocurrent generation mechanism of a CMOS photodiode. Based on the process parameters furnished by the CMOS process vendor, the capacitance and leakage current of the photodiode was calculated. Next, various readout methods including the pulse modulation photosensing method for the photodiode were described. The pulse modulation method is applied in this work and will be further elaborated in the following chapters. On-chip imaging configuration using the CMOS image sensor was then described. For on-chip imaging, an analysis of light propagation in liquid and turbid media was presented. Following this, the fluorophore detection limit inside the mammalian brain was calculated. This chapter laid down the fundamentals for the development and application of the CMOS image sensor in the subsequent chapters.

References

[1] J. R. Janesick, “Lux transfer: CMOS versus CCD,” in *Proceedings of SPIE*, Sensors and Camera Systems for Scientific, Industrial, and Digital Photography Applications III, M. M. Blouke, J. Canosa, N. Sampat, ed.s, vol. 4669, pp. 232-249, Apr. 2002.

[2] R. A. Yotter, D. M. Wilson, “A review of photodetectors for sensing light-emitting reporters in biological systems,” *IEEE Sens. J.*, vol. 3, pp. 288-303, Jun. 2003.

[3] C. G. Coates, D. J. Denvir, N. G. McHale, K. D. Thornbury, M. A. Hollywood, “Optimizing low-light microscopy with back-illuminated electron multiplying charge-coupled device: enhanced sensitivity, speed, and resolution,” *J. Biomedical Optics*, vol. 9, pp. 1244-1252, Nov. 2004.

[4] H. Zimmermann, “Improved CMOS-integrated photodiodes and their application in OEICs,” *Workshop on High Performance Electron Devices for Microwave and Optoelectronic Applications*, pp. 346-351, Nov. 1997.

[5] Y. Değerli, F. Lavernhe, P. Magnan, J. A. Farré, “Analysis and reduction of signal readout circuitry temporal noise in cmos image sensors for low-light levels,” *IEEE Trans. Electron Devices*, vol. 47, pp. 949-962, May 2000.

[6] C. Xu, W. Zhang, W. -H. Ki, M. Chan, “A 1.0-V VDD CMOS Active-Pixel Sensor With Complementary Pixel Architecture and Pulsewidth Modulation Fabricated With a 0.25-µm CMOS Process,” *IEEE J. Solid-State Circuits*, vol. 37, pp. 1853-1859, Dec. 2002.

[7] C. Hagleitner, A. Hierlemann, D. Lange, A. Kummer, N. Kerness, O. Brand, H. Baltes, “Smart single-chip gas sensor microsystem,” *Nature*, vol. 414 , pp.293-296, Nov. 2001.

[8] P. A. Hammond, D. Ali, D. R. S. Cumming, “Design of a single-chip pH sensor using a conventional 0.6-µm CMOS process,” *IEEE Sens. J.*, vol. 4, pp. 706-712, Dec. 2004..

[9] T. Tokuda, A. Yamamoto, K. Kagawa, M. Nunoshita, J. Ohta, “A CMOS image sensor with optical and potential dual imaging function for on-chip bioscientific applications,” *Sens. Actuators A*, vol. 125, pp. 273-280, Jan. 2006.

[10] K. Sawada, T. Ohshina, T. Hizawa, H. Takao, M. Ishida, “A novel fused sensor for photo- and ion-sensing,” *Sens. Actuators B*, vol. 106, 614-618, May 2005.

[11] G. Zeck, P, Fromherz, “Noninvasive neuroelectronic interfacing with synaptically connected snail neurons immobilized on a semiconductor chip,” *Proc. Natl. Acad. Soc.*, vol. 98, pp. 10457-10462, Aug. 2001.

[12] J. Lee, J. D. Rogers, D, L. Nida, J. S. Aaron, K. V. Sokolov, R. R. Richards-Kortum, M. R. Descour, “Multimodal miniature microscope (4M Device): novel methodology for multimodality tissue imaging in vivo,” in *Proceedings of SPIE*, Manipulation and Analysis of Biomolecules, Cells, and Tissues, D. V. Nicolau, J. Enderlein, R. C. Leif, D. L. Farkas, ed.s, pp. 168-176, Jun. 2003.

[13] V. -D. Tuan, G. Griffin, D. L. Stokes, A. Wintenberg, “Multi-functional biochip for medical diagnostics and pathogen detection,” *Sens. Actuators B*, vol. 90, pp. 104-111, Apr. 2003.

[14] T. Furumiya, D. C. Ng, K. Yasuoka, K. Kagawa, T. Tokuda, M. Nunoshita, J. Ohta, “Functional verification of pulse frequency modulation-based image sensor for retinal prosthesis by in vitro electrophysiological experiments using frog retina,” *Biosens. Bioelectron.*, in Press, 2005.

[15] Ohta J, Tokuda T, Kagawa K, Terasawa Y, Ozawa M, Fujikado T, Tano Y. “LSI-based stimulus electrodes for retinal prosthesis,” presented at the *2nd DOE Int. Symp. Artificial Sight*, Ft. Lauderdale, Florida, USA, Apr. 29, 2005.

[16] C. -N.Chien, F. -S. Jaw, “Miniature telemetry system for the recording of action and field potentials,” *J. Neurosci Methods*, vol. 147, pp. 68-73, Aug. 2005.

[17] J. Mavoori, A. Jackson, C. Diorio, E. Fetx, “An autonomous implantable computer for neural recording and stimulation in unrestratined primates,” *J. Neurosci. Methods*, vol. 148, pp.71-77, Oct. 2005.

[18] J. Singh, *Semiconductor optoelectronics physics and technology*, New York: McGraw-Hill, 1995.

[19] H. Holloway, A. D. Brailsford, “Peripheral photoresponse of a p-n junction,” *J. Appl. Phys.*, vol 54, pp. 4641-4656, Aug. 1983.

[20] S. Ehrenfri, “0.6 μm CMOS CUP process parameters,” Austria Mikro System International, Document #: 9933011 B, Oct. 1998. (confidential)

[21] W.-F. Cheong, S. A. Prahl, A. J. Welch, “A review of the optical properties of biological tissues,” *IEEE J. Quantum Electron.*, vol. 26, pp. 2166-2185, Dec. 1990.

[22] D. R. Doiron, L. O. Svaasand, and A. E. Profio, “Light dosimetry in tissue applications to

photoradiation therapy," in *Porphyrin Photosensitization*, D. Kessel, T. J. Dougherty, ed.s, New York: Plenum, 1983, pp. 63-75.

[23] Y. Kanaoka, T. Takahashi, H. Nakayama, K. Takada, T. Kimura, S. Sakakibara, "A new fluorogenic substrate for aminopeptidase," *Chem. Pharm. Bull. (Tokyo)*, vol. 25, pp. 362-363, Feb. 1977.

Chapter 3

Fluorescence Detection and Imaging

In this chapter the use of CMOS photosensor for fluorescence detection is evaluated. An n-well/p-sub photodiode is used due to its high sensitivity. The capability for low light intensity and photosensing was evaluated using a pulse modulation (PM) photosensing readout circuit. By measuring the photosensor characteristic, it is found that the photosensor is capable of detecting light intensity down to 1 nW/cm^2 with a dynamic response range of 120 dB. An accurate modeling equation is developed to study the photosensing characteristics. Using the photosensors, both the static and dynamic fluorescence measurements are demonsrrated. Measurement resolution of 1 nM of the fluorescent agent 7-Amino-4-methylcoumarin (AMC) and real-time measurement of Indo1/Ca^{2+} fluorophore complex are demonstrated. By implementing an array of photosensors, we devised a CMOS image sensor. Two types of read-out methods were studied and we found that by connecting a high speed analog-to-digital (A/D) converter to the analog current output of the photosensors (pixels) we are able to obtain comparatively fast imaging frame rates. Finally, we developed a novel packaging method that enabled on-chip fluorescence imaging. The excitation light used in fluorescence studies is attenuated using a color filter that has high selectivity for a number of fluorophore species. A transmittance of -44 dB is achieved by multiple coating of the filter. The fully packaged device is about 350 μm thick. Using the packaged device, fluorophore sensitivity measurements were performed. The CMOS technology used in this work are the standard 0.60 μm 3-metal 2-poly, and 0.35 μm 4-metal 2-poly processes.

Keywords: pulse modulation, CMOS image sensor, bioimaging, fluorescent

3.1 Introduction

The fluorescence technique is a highly specific and sensitive method for detecting chemical and biomolecular events. Because of high specificity of this method, it is often used to detect the existence of a certain biomolecular species. Biofluorescene refers to fluorescence of biological origin. To date, a great number of fluorescence probes or fluorophores have been developed to target specific cellular ions, DNA, or proteins [1].

Fluorescence detection is possible due to the wavelength difference between the excitation and emitted fluorescence lights. By carefully filtering the two wavelengths, the emitted fluorescence signal can be detected and measured. Traditionally, fluorescence detection systems are based on an instrument which consists of a light source, excitation and emission filters and a photodetector. Spectrofluorometers and fluorescence microscopes are examples of these systems that are widely used for fluorescence detection and imaging. In this work, we focus on the development of a CMOS image device dedicated for biofluorescence applications.

CMOS image sensors have recently attracted much attention from the biological science community. They offer both image sensing and fluorescence measurement capabilities. We are exploring the possibility of utilizing the CMOS image sensors for multi-parameter on-chip imaging. The proposed idea is to embed a host of CMOS-based sensors in a two-dimensional array, forming a truly integrated sensor chip as shown in Fig. 3.1. This chip, when thinned-down to about 150 μm and bonded onto a flexible substrate, will ensure conformance of the sensor to the physical contours of the biological sample for example the eye. The advantages of using a CMOS image sensor for fluorescence imaging are high spatial and temporal resolution imaging at high frame rates. Also, such CMOS image sensors have shown a comparable sensitivity to conventional CCD image sensors for fluorescence detection [2, 3]. Because of its inherent

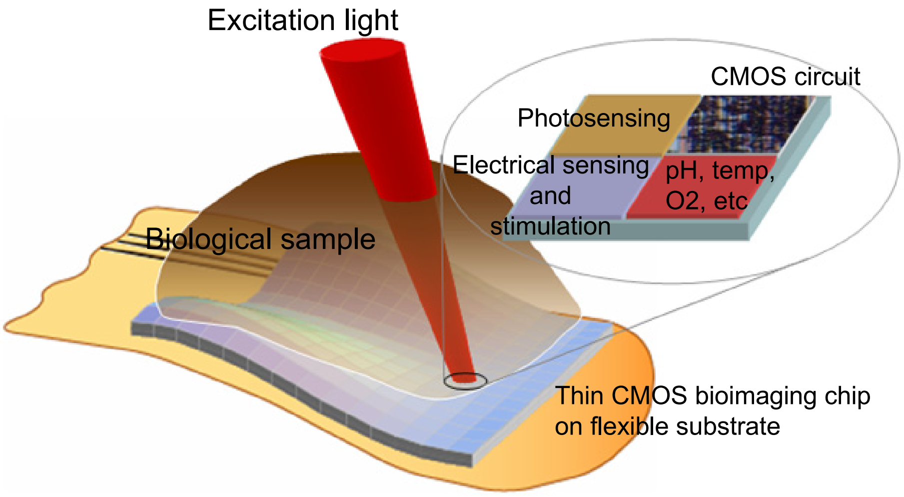

Fig. 3.1 Schematic of proposed CMOS sensor chip implementation of a multi-parameter sensing pixel onto an array onto a flexible substrate.

system-on-chip capability, a single chip is all that is required for sensing, signal processing and data interface, resulting in a highly integrated and compact device. This will have a wide appeal due to its small dimensions and hence will be available for a myriad of applications like brain imaging and micro-array fluorescence detection.

In this chapter, low light intensity fluorescence is used as the application platform to demonstrate the CMOS photosensor detection capability. The targeted applications are static and dynamic measurements of fluorescent emission from biological cells. Studies such as high resolution neuropsin (a brain protease) imaging in the study of memory and learning function of the brain and real-time calcium ion flux transport in intracellular cells will greatly benefit from the development of this sensor chip. Furthermore, a CMOS imaging device is developed to enable simultaneous imaging and detection capability at near video frame rates. By developing a special packaging technique for the image sensor, on-chip fluorescence imaging is possible. These issues will be discussed in detail in this chapter.

3.2 CMOS Photosensor

In Chapter 2, the CMOS photosensor ability to detect incident light was described. In this work, a CMOS photosensor was designed for sensing light from a fluorescent light source. This is useful in order to apply the CMOS image sensor in fluorescence techniques. In order to determine the light detection characteristic of the CMOS photosensor, measurement is performed by using a monochromatic light source and an actual fluorescence source. This will provide experimental values for sensitivity and minimum detection limit. Further, the photosensor applied in static and dynamic measurements to assess its capability in fluorescence detection.

3.2.1 Pulse Modulation Photosensing

Detection of low intensity fluorescence with a wide dynamic measurement range is a requirement for most applications due to the minute amount of fluorophore present and the high excitation light intensity. Hence, a photosensor design that is able to address these issues is required. In order to design a CMOS photosensor for this purpose, we have studied and utilized the pulse modulation method. Following the discussion in Chapter 2, a photosensor with pulse modulation circuit was designed. The schematic of this circuit is shown in Fig. 3.2. It consists of a photodiode, a comparator, and a reset switch with feedback from the output. As described in Chapter 2, the n-well/p-sub CMOS photodiode is used due to its higher responsivity across a wider range of spectrum. In the circuit, the cathode terminal of the photodiode is connected to the comparator, implemented by a differential amplifier, across a source follower. The differential amplifier acts as an analog-to-digital converter.

The operation of the photosensor can be described as follows. At the negative edge of the reset signal, Rstin, the photocurrent will discharge and the photodiode voltage V_{PD} will reduce.

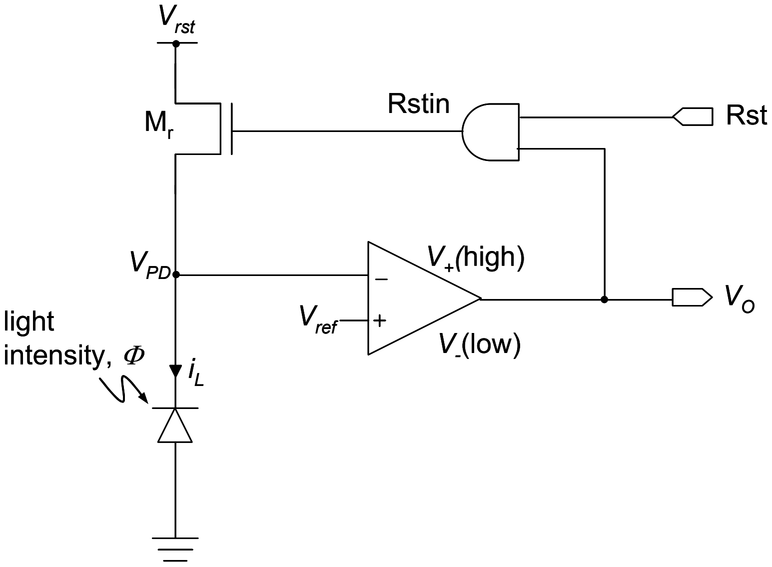

Fig. 3.2 Schematic of pulse modulation photosensing circuit.

When V_{PD} falls below the reference voltage V_{ref}, the output voltage, V_O goes low. On reset, the output returns high and the photodiode voltage is reset to the value V_1 which takes on the value of $V_{rst}-V_{th}$, where V_{th} is the threshold voltage of the reset transistor, Mr. This operation is shown in Fig. 3.3 (A). By measuring the time between reset and output high, the photodiode discharge time, t_d can be determined. Additionally, the slope of the discharge curve is related to the intensity of the incident light Φ. A shorter discharge time t_{d1} corresponds to a higher light intensity Φ_1 as shown in Fig. 3.3 (B). This relationship can be used to measure the light intensity. The relationship between photocurrent i_L and discharge time or the pulse width between reset, t_d can be expressed by

$$t_d = \frac{C_{PD}\left(V_1 - V_{ref}\right)}{i_L^{\gamma}}, \tag{3.1}$$

where C_{PD} is the photodiode capacitance, and V_1 is the maximum source follower voltage at reset. The denominator term, i_L has a power correction factor γ. The photocurrent i_L is related to the incident light intensity as follows

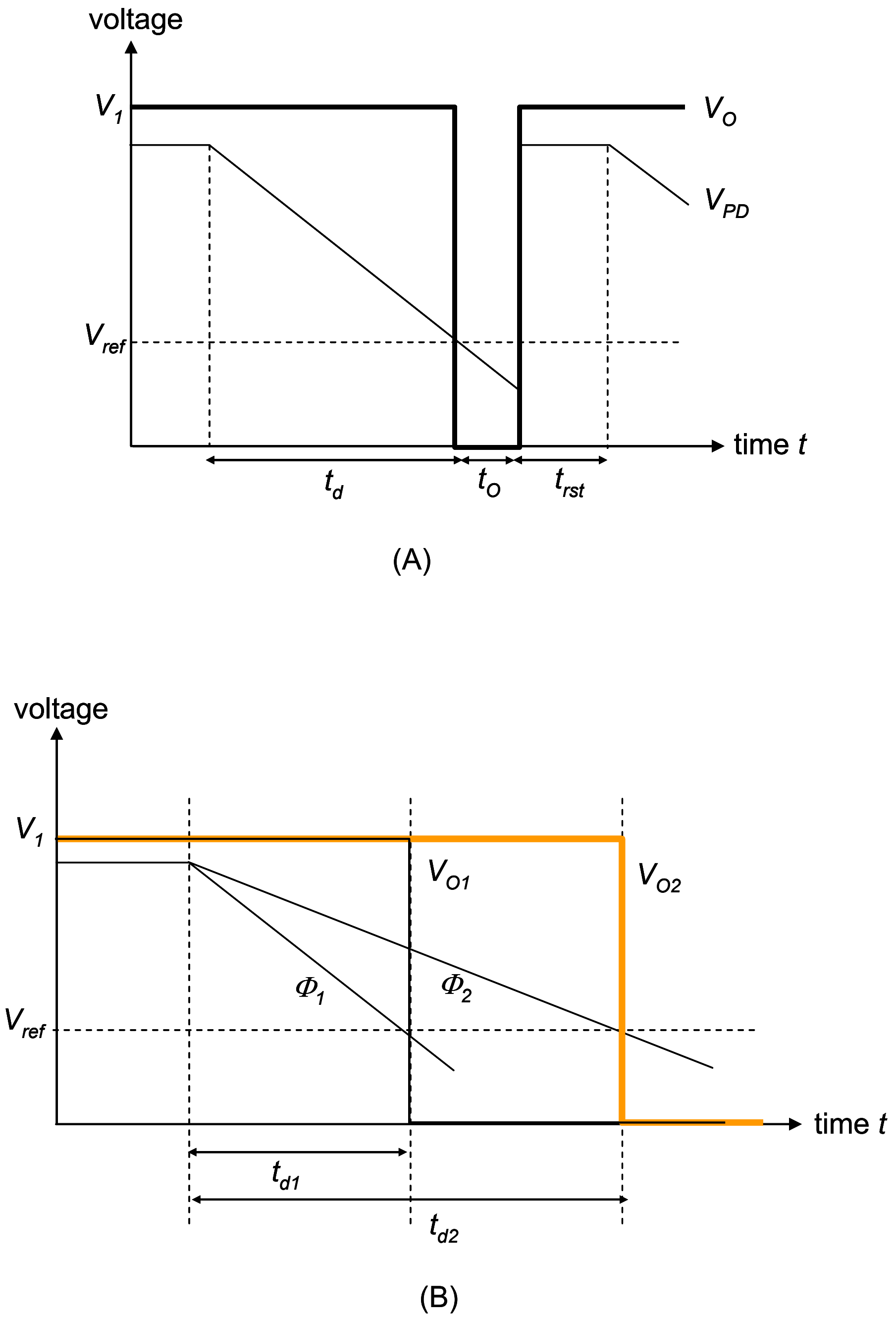

Fig. 3.3 (A) Diagram of pulse modulation photosensing operation. (B) Output of pulse modulation photosensing depends on the intensity of input light.

$$i_L = R \cdot A \cdot \Phi + i_D, \tag{3.2}$$

where R is the photodiode responsivity, A is the photodiode area, and i_D is the photodiode dark current.

The pulse modulation circuit can be operated in two different modes, the pulse frequency modulation mode (PFM) [4-6] or the pulse width modulation mode (PWM) [7-9]. In the PFM mode, the reset signal, Rst is kept high and when V_O become low, the photodiode is immediately reset resulting in very short output pulse width, t_O and reset time, t_{rst}. Thus, the PFM mode is also referred to as self-reset photosensing. In order to operation in the PFM mode, a delay element, implemented either with an inverter chain or a flip-flop, is inserted between the amplifier output and the reset transistor, as described in Chapter 2. In PWM mode, the reset signal pulse Rst is controlled at a constant period. By controlling this period, the saturation of the photodiode caused by extremely high incident light can be avoided, vice-versa, extremely long integration periods can be properly measured. It should be noted that the PFM mode is suitable in a bright environment, where the output pulse frequency can easily be captured using a pulse counter. On the other hand, the PWM mode is more suited for a dark environment, when faint light measurement is necessary. The long integration time caused by the slow photodiode discharge can be easily measured. When high intensity light is incident on to the pulse modulation sensor, high-frequency output pulses (low discharge time pulses) are generated. On the other hand, low-intensity light input will cause low-frequency output pulses (large discharge time between pulses). Due to the fact that the output is digitized in pulses, output storage, data transmission and signal processing will be much simplified.

3.2.2 Photosensitivity and Dark Current

A photosensor test-element-group (TEG) based on the pulse modulation circuit was

Table 3.1 Specifications of pulse modulation photosensor TEG.

Process		0.6 μm CMOS 3M2P
Size		100 x 400 μm^2
Photodiode	type	p-diff/n-well
	size	50 μm x 50 μm
Pulse width resolution		0.4 μs ~ 0.4ms
Dynamic range		6 decades (120 dB)
Minimum detectable change		1.6×10^3 photon/s
Dark current		0.12 pA

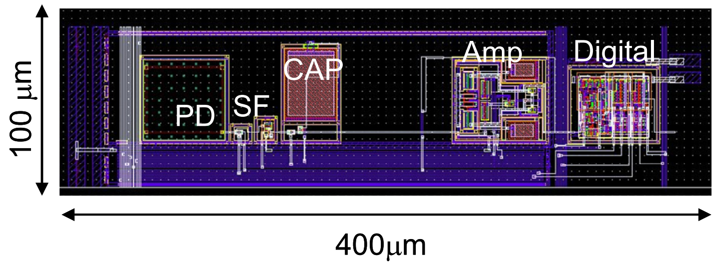

Fig. 3.4 Layout of pulse modulation photosensor.

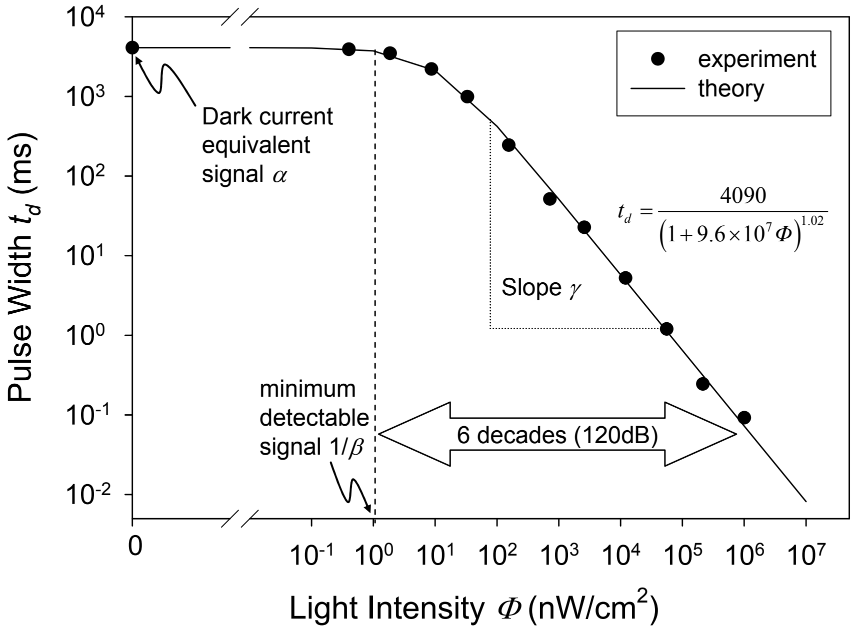

Fig. 3.5 Photosensitivity measurement from pulse modulation photosensor at wavelength of 670 nm.

fabricated. The TEG layout is shown in Fig. 3.4. Its specifications are listed in Table 3.1. In order to measure the sensitivity of the photosensor we used a semiconductor laser with a wavelength of 670 nm. The laser light was directed perpendicular to the photodiode. By decreasing the incident light intensity using neutral density filters (MAN-25-1, 10, 50 Sigma Koki, Japan) we are able to measure up to 6 orders of light intensity change. In order estimate the dark current, measurement in total darkness was also performed.

Fig. 3.5 shows the result of light sensitivity measurement for the pulse modulation photosensor operated in PWM mode. From the result, it can be observed that the pulse modulation photosensor has an excellent linearity, with the dynamic range of 6 decades (120 dB). Also, by inspection, the minimum measurable detection limit is found to be about 10 nW/cm^2. For each of the measurement point, multiple readings were taken in order to determine the output variations. Throughout the entire input light intensity range, the deviation from the measurement mean is less than ±0.2 %. This represents a resolution of 20 pW/cm^2 for the minimum detectable intensity level. Hence, the minimum detectable deviation in intensity level is 20 pW/cm^2. Using the conversion factor of $5.05 \times 10^{15}\lambda$ photon/cm^{2}s (where λ is in nm), the minimum detectable change in photon level can be calculated using the following equation,

$$\Delta P_{\min} = 5.05 \times 10^{15} \times \lambda \times \Delta\Phi_{min} \times A, \tag{3.3}$$

where $\Delta\Phi_{min}$ is the minimum detectable intensity deviation, and A is the photodiode area. Its value is worked out to be about 1.6×10^3 photon/s.

By inspection of eq. (3.1), a modeling equation of the following form can be used to fit the photosensitivity experimental data.

$$t_d = \frac{\alpha}{(1 + \beta \cdot \Phi)^{\gamma}}. \tag{3.4}$$

When fitted to eq. (3.4), the constants α, β and correction factor, γ were replaced by the values 4.09 s, 9.6×10^7 cm^2/W, and 1.02, respectively to give a best fit for the experimental data. These values can also be obtained by studying the physical implications for each constant. When the light intensity is zero, α, which corresponds to the y-axis intercept, is the dark current equivalent signal. The constant β is related to the minimum detectable light intensity level. In which case, its value will be related to the dark current value i_D. By inspection of equations eq. (3.1), (3.2), and (3.4),

$$\beta = \frac{(R \times A)}{i_D}. \tag{3.5}$$

This constant represents the reciprocal of minimum detectable level (see Appendix). Finally, γ is the magnitude of the slope which is the detection sensitivity of the photosensor.

In order to estimate the value of the constant α, the dark current i_D value need to be known. This value can be determined by measurement of the pulse width output in absolute darkness. Under this condition, only the leakage current contributes to the discharge of the photodiode. Alternatively, it can also be calculated from the following equation,

$$i_D = \left. \frac{C_{PD}\left(V_1 - V_{ref}\right)}{t_{dis}} \right|_{\Phi=0}. \tag{3.6}$$

The experimental measurement condition are; V_{rst} = 5 V, V_{th} = 1 V, and V_{ref} = 2 V. The photodiode capacitance C_{PD} is calculated from the process data which was supplied by the CMOS foundry [10]. For a 50 × 50 μm^2 n-well/p-sub diode, the total capacitance (side-wall and lateral) taken at the average bias voltage of 3.5 V is 145 fF. The dark current i_D is then calculated by using eq. (3.6) which equals 70.8 fA. This i_D value agrees well with the leakage current data supplied by the CMOS foundry for a nwell/psub diode of the same size (see §2.3.1). Hence, by rewriting eq. (3.6), the value of α can then be estimated as follows,

$$\alpha = t_d\big|_{\Phi=0} = \frac{i_D}{C_{PD}\left(V_1 - V_{ref}\right)}. \tag{3.7}$$

By reusing the leakage current data as i_D, α can then be calculated to be equal to 4.462 s. This value can be taken as the theoretical limit for α.

The constant β is calculated from eq. (3.5). The responsivity of the photodiode R at $\lambda = 670$ nm has been measured to be about 0.19 A/W (see Chapter 2). Using this value, the constant β can be calculated to be 6.71×10^7 cm^2/W. The calculated value matches closely the fitted value of 9.6×10^7 cm^2/W and can be taken as the reciprocal of the theoretical minimum detection level Φ_{min}. The slight discrepancy is due to the under estimation of the photodiode responsivity R for photodiodes of different sizes. In this photosensor TEG, the photodiode area is 50×50μm^2 as compared to the photodiode used to the responsivity measurement of 200×200μm^2. In this case, the minimum detection level value Φ_{min} which is the inverse of the constant β is then calculated to be equal to 10.4 nW/cm^2. This value is exceptionally close to the value as inspected from the graph in Fig. 3.15 which is 10 nW/cm^2.

The constant, γ in eq. (3.1) which initially seems counter intuitive as physically γ should always be 1, can be understood as the measurement sensitivity. This value is dependent on the system characteristics as well as the experiment conditions. For the ideal case, γ is equal to 1. In most cases, it lies very close to 1 for photosensor. As the measurement becomes more complicated, involving image sensors and non-linear light sources, the γ value will shift further away from 1.

3.2.3 Fluorescence Detection

Static and dynamic measurements of fluorescence were performed using the pulse modulation photosensor. For static measurement (time invariant), the UV excitable fluorophore, 7-Amino-4-methylcoumarin, AMC (3099-v Peptide Institute, Japan) was used. The excitation peak wavelength of AMC is 380 nm, and its emission peak wavelength is 460 nm. For dynamic measurements (time varying), the cell impermeant type Ca^{2+} indicator, Indo1 (I004-10 Dojindo

Lab., Japan) was used. The excitation peak wavelength of Indo1 is about 340 nm for calcium free and calcium saturated Indo1, and the emission peak wavelengths are 475 nm for calcium free and 401 for calcium saturated Indo1. The excitation source for both experiments is a HeCd laser (325 nm) beam with a cross-section diameter of about 2 mm. Fluorescence emission was measured using the photosensors positioned away from the direct excitation light path.

(i) Static Fluorescence Measurement

The experimental setup for the static measurement of different concentrations of the AMC fluorophore is shown in Fig. 3.6 (A). A washer with an inner diameter of 3.3 mm and height of 0.5 mm ensured that only a small volume of AMC (about 6 μl) was used. Due to the high-intensity excitation light from the laser, the beam was directed away from the photosensor as shown in Fig. 3.6 (B). In the experiment, different concentrations and excitation light intensities were used. The concentration of AMC used ranged from 1 nM to 100 μM, while the excitation light intensity covered 6 nW/cm^2 to 2 mW/cm^2. Discharge time readings were taken for varying AMC concentrations and light intensities. Fig. 3.7 shows the relationship of the measured pulse width t_d against the fluorophore concentration and the excitation light intensity. From the experiment, the minimum detectable AMC concentration of 1 nM was obtained.

(ii) Dynamic Fluorescence Measurement

For the dynamic fluorescence experiment changes in fluorescence intensity from Ca^{2+} free Indo1 to Ca^{2+} saturated Indo1 was measured. In the experiment 50 ml of $CaCl_2$ at 10 mM was added to 500 μl of Indo1 at 10 μM inside a PMMA cuvette. The PMMA material is relatively unexcited by the UV irradiation light. A continuous measurement was performed to observe dynamic changes before and after formation of Indo1/Ca^{2+} complex. The experiment setup is

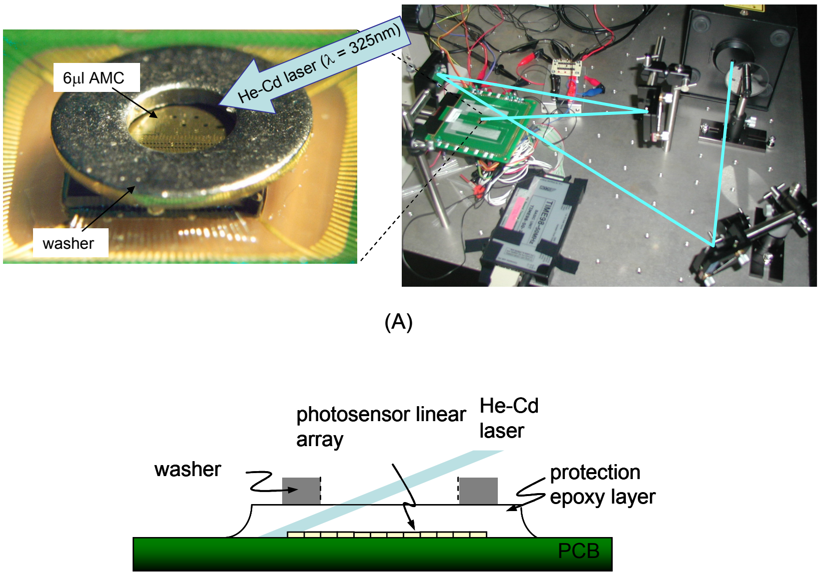

(A)

(B)

Fig. 3.6 (A) Photograph of experimental setup for AMC concentration measurement. (B) Diagram of AMC concentration measurement experiment

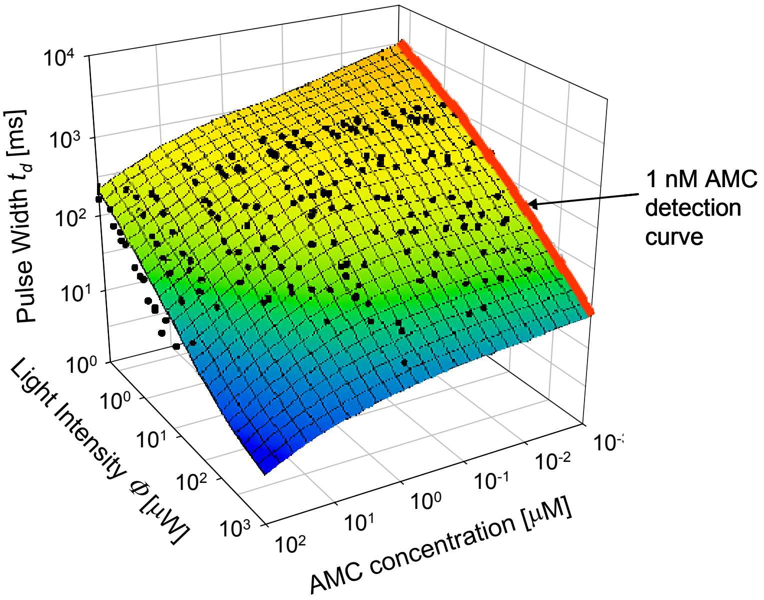

Fig. 3.7 AMC sensitivity measurement at different excitation light intensities.

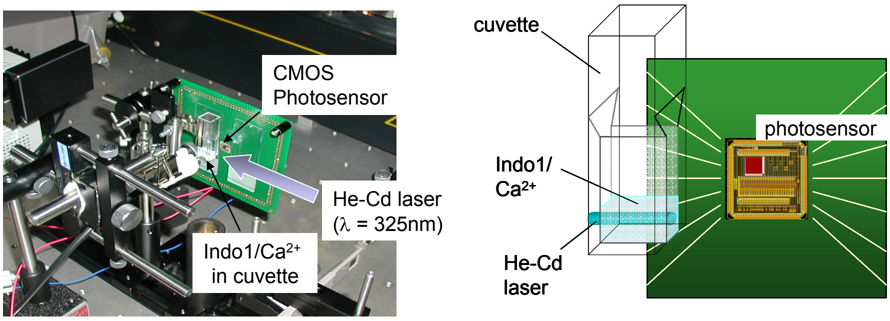

(A) (B)

Fig. 3.8 (A) Photograph of transient fluorescence measurement of Indo1/Ca^{2+} complex experiment, and (B) diagrammatic representation of experimental setup.

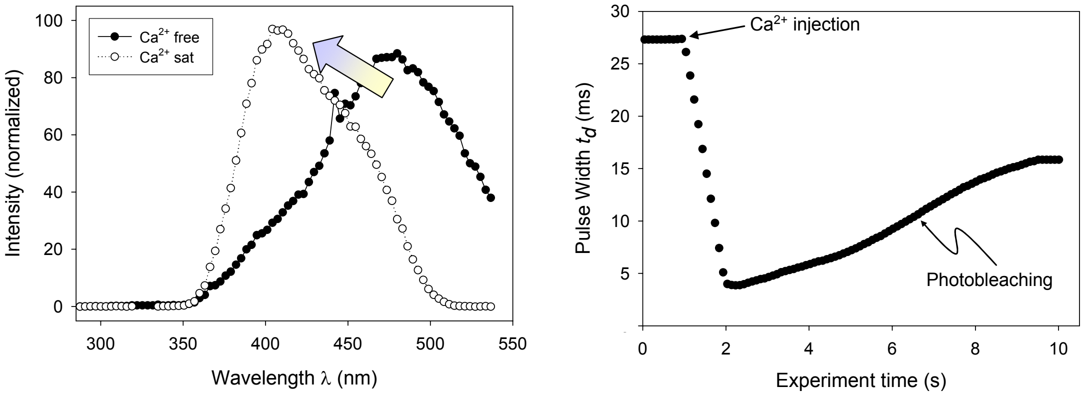

(A) (B)

Fig. 3.9 A) Intensity and spectrum change from Ca^{2+} free Indo1 to Ca^{2+} saturated Indo1 as measured by using a calibrated Princeton multispectral analyzer. (B) Intensity change when Ca^{2+} injected into Indo1 as measured by the CMOS photosensor.

shown in Fig. 3.8. The spectrum is shifted for Ca^{2+} free and Ca^{2+} saturated Indo1 as shown in Fig. 3.9 (A). The dynamic measurement shows that the continuous measurement using the pulse modulation mode is possible as shown in Fig. 3.9 (B). Here the fluorescent intensity changes due to the introduction of Ca^{2+} and subsequently a photobleaching effect can be clearly seen. This experiment shows that using the photosensor in pulse modulation mode, dynamic measurement in the sub-second order is possible.

3.3 CMOS Image Sensor

Depending on the applications involved, photosensing capability only may not be sufficient to meet all the requirements. The need for imaging capability is most apparent in studies involving interactions between fine structures which require information in the spatial domain. An example would be to observe and measure the growth of a cell. The distinction between photosensing and imaging can best be illustrated by comparing a spectrometer and a microscope. In this work, fluorescence imaging is required for studying a biological specimen both in vitro and in vivo. Hence, the CMOS image sensor is developed and tested for fluorescence imaging. The capability of the CMOS image sensor for this purpose is described in this section.

3.3.1 Device Design

In order to implement a 2D array of photosensors (image sensor), the photosensor is modified into an active pixel sensor (APS) circuit as shown in Fig. 3.10 (A). The pixel circuit consists of additional transistors that form the source follower input and the switch for the row select signal. Each pixel output is connected to the column bus line which is output as analog current and also to the comparator and stored as 1-bit memory in a DFF before output as digital

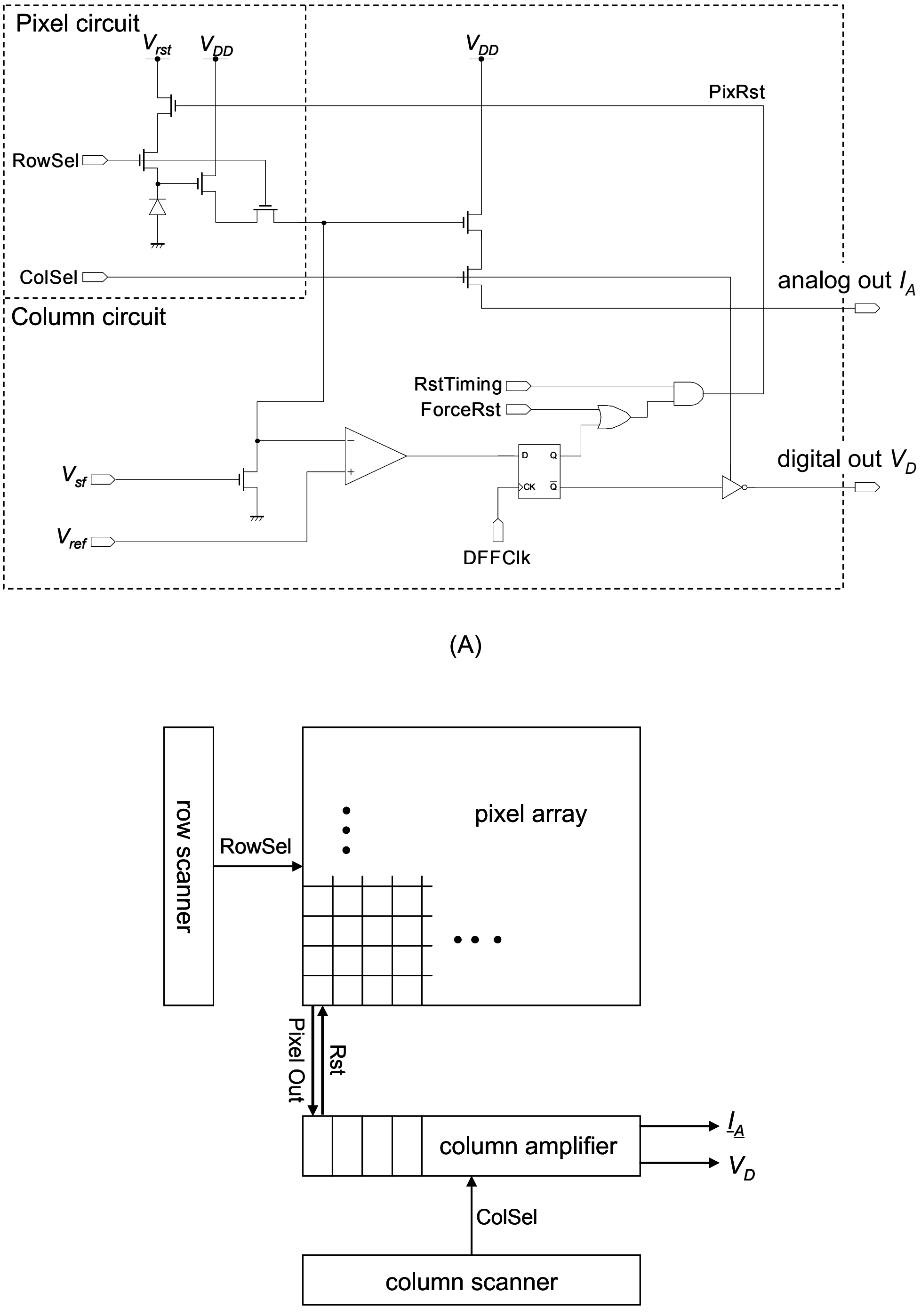

(A)

(B)

Fig. 3.10 (A) Schematic of active pixel sensor photosensing circuit with output connected to the column bus and column amplifier. V_{rst}, V_{DD}, V_{sf} are the reset voltage, supply voltage and bias voltage of source follower respectively. (B) Block diagram of CMOS image sensor.

pulse. The column bus is connected to a column amplifier and the array output is read out sequentially using a column scanner in a serial fashion. This reduces the number of input-output pads. The block diagram of the image sensor is shown in Fig. 3.10 (B). The analog current output I_A is connected to an off-chip amplifier while the pulse modulation sensing mode (as explained in §3.2.1) provides the digital output V_D. As will be discussed later, by using the analog output, imaging with a faster frame rate can be achieved. This is useful for real-time imaging where visual feedback is important during in vivo imaging. Although the digital output offers wider dynamic range and lower light detection sensitivity, it suffers from a reduced frame rate. The timing chart for operating the image sensor with digital output is shown in Fig. 3.11.

A 176 × 144 array image sensor chip was designed and fabricated using the standard CMOS process. Due to its high photon responsivity, the n-well/p-sub photodiode was utilized. Each pixel has a size of $7.5 \times 7.5\ \mu m^2$. The dimension of the chip is $2 \times 2.5\ mm^2$. It is designed to be large enough to image the mouse hippocampus and yet small enough for invasive imaging of each brain hemisphere independently. A photomicrograph of the CMOS image sensor is shown in Fig. 3.12. In the design, only a single side of the chip has input-output pads. This helps reduce complexity in wire bonding during the packaging process and helps reduce the final packaged device size. This is an important factor for implementing on-chip in vivo imaging. The specifications are shown in Table 3.2. Fig. 3.13 shows a schematic of the measurement setup of the image sensor and a PC. The analog output is connected to an off-chip interface circuit board. The analog electrical current output signal from the chip is converted to a voltage signal via a transimpedance amplifier before digitized into 12-bit data using an analog-to-digital (A/D) converter and read into the digital (input-output) I/O board (PCI-2772C Interface Corp., Japan) inside the PC. The control signals are supplied by a PC (Dimension 8400 Dell). Because the maximum operating voltage of the chip is limited to 3.3 V, a voltage shift circuit is needed to

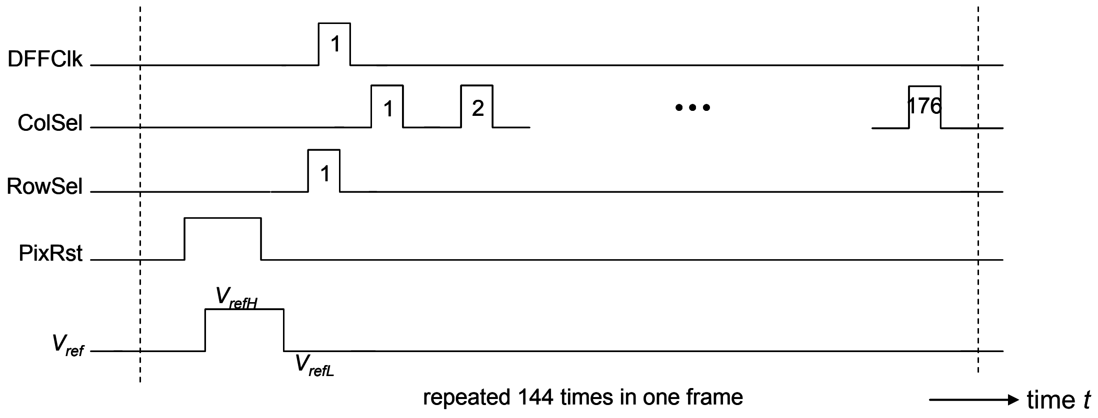

Fig. 3.11 Timing chart of CMOS image sensor operation in pulse modulation mode for digital pulse output. All pulse high is 5 V and pulse low is 0 V except for V_{ref} which is given by V_{refH} and V_{refL} respectively.

Table 3.2 Specifications of CMOS image sensor.

Technology		0.35 μm Std. CMOS 4M2P
Power supply		3.3 V
Chip size		2 mm x 2.2 mm
Pixel	type	modified 3-transistor APS
	number	176 x 144 (QCIF)
	size	7.5 x 7.5 μm^2
Photodiode	type	nwell/psub
	Size	16.2 μm^2
Output		analog current, digital 1-b pulse
Dynamic range		3 decade (60 dB)
Frame rate (with external A/D)		0.08 – 16.5 fps

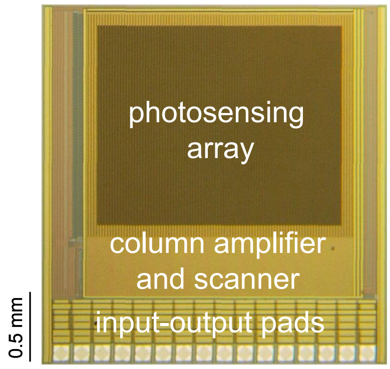

Fig. 3.12 Photomicrograph of CMOS image sensor.

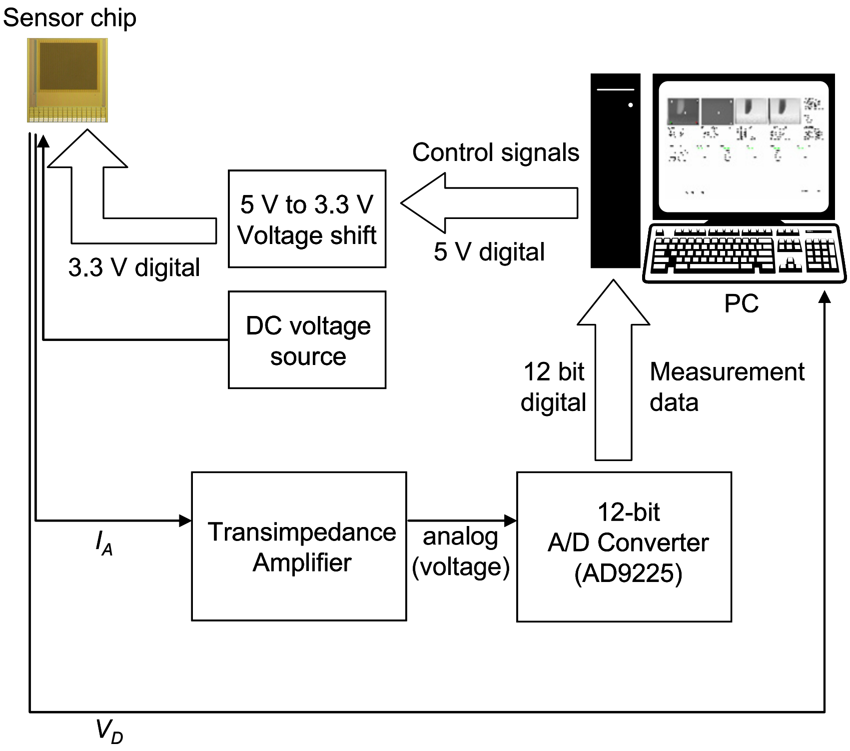

Fig. 3.13 Schematic of the device measurement setup and PC interface.

convert the 5 V signals from the PC. The digital output from the chip is read off the chip directly.

A customized program is developed to control the input output signals. Digitized data from the image sensor is stored, processed and displayed onto the screen. Image subtraction of a background image captured at the beginning and during the program operation enables minute changes to be tracked. Imaging dynamic range is increased by changing the integration time or frame rate during operation. This way, up to 4 decades of light intensity changed can be faithfully imaged. Also, auto-balancing of the image enables high contrast images to be displayed. This operation essentially stretches the grayscales to the maximum possible 255 so that small changes in the measured values can be seen with the naked eye. Also, real time data plotting enable quick monitoring of changes in the signal during the experiment. Fig. 3.14

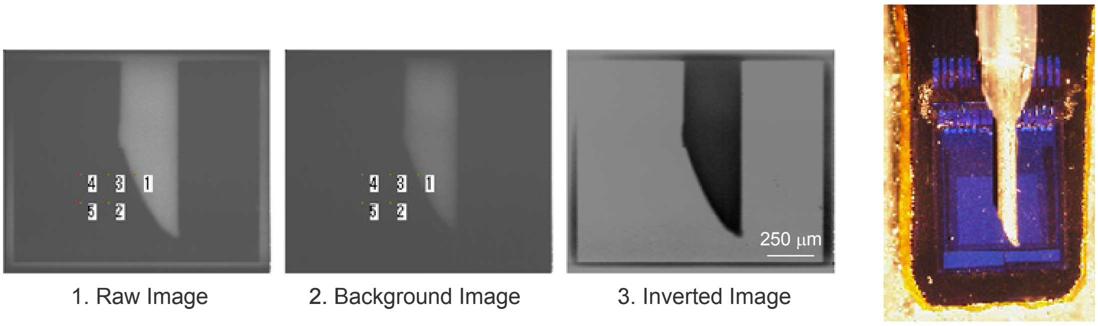

1. Raw Image 2. Background Image 3. Inverted Image

Fig. 3.14 Screen capture of program operation using the 176 x 144 pixel array image sensor. The position of five pixels can be set independently and is shown in Image 1 (Raw Image). Image 2 is the image captured at program initialization. Image 3 shows the inverted image where Image 2 is subtracted from Image 1. The image shows a hypodermic tube attached to the image sensor captured in air as shown in the microphotograph on the far right.

shows a typical output from the program operation.

3.3.2 Light sensitivity

The photosensitivity of the image sensor operating in the pulse modulation mode is measured by using the same procedure as described in §3.2.2. The measured result is shown in Fig. 3.15. A comparison with the photosensitivity of a single photodetector (Fig. 3.5) shows that the measurable dynamic range is reduced by 3 decades. This is due to the fact that each pixel on the image sensor array is scanned and its output was read out individually. In the digital output operation, a single frame consists of only 1-bit information. In order to display 255 gray levels, a minimum of 256 frames need to be captured. The combination of row scan and accumulation of the frames amounts to an increase in required imaging time of about 3 orders of magnitude. This can be unacceptable long for imaging purposes. As explained in Chapter 2, the output from the pixels on the array can be read out at a constant rate whereby the analog current output is used, or by comparing the photodiode voltage of each pixel as in the pulse modulation sensing mode. In the former, the output resolution will be determined by the performance of the A/D

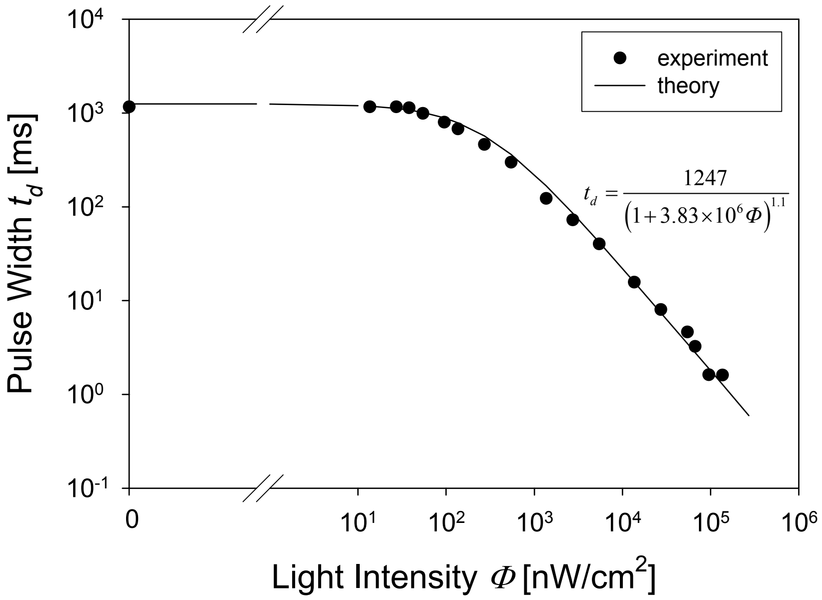

Fig. 3.15 Photosensitivity measurement from image sensor at 470 nm operating in pulse width modulation.

converter. This configuration can be used to improve the imaging frame rates. The disadvantage of this method is the requirement of additional off-chip circuitries. On the other hand, the advantage of using pulse modulation mode is single chip operation. However, the trade off for this method is the longer frame time. Nevertheless, it has been shown that a 64 × 64 image array operating in the pulse modulation mode can be useful for static fluorescence imaging in a previous work [11, 12]. In order to achieve a reasonable frame time, the image sensor operating with analog output is used this work.

3.3.3 On-chip Imaging Resolution

An investigation on the imaging resolution capability for on-chip imaging was performed. On-chip imaging configuration refers to the operation of image sensor with the sample in contact with the sensor without additional use of other optical elements as described in Chapter 2. This is to determine the minimum resolvable pattern during in vivo imaging in the brain. In

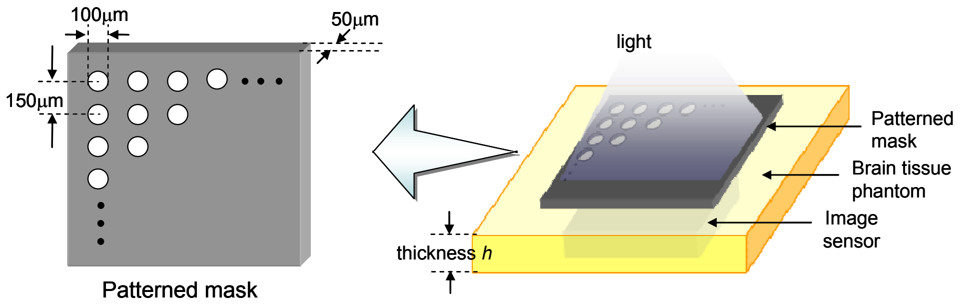

Fig. 3.16 Experimental setup used to determine on-chip imaging resolution.

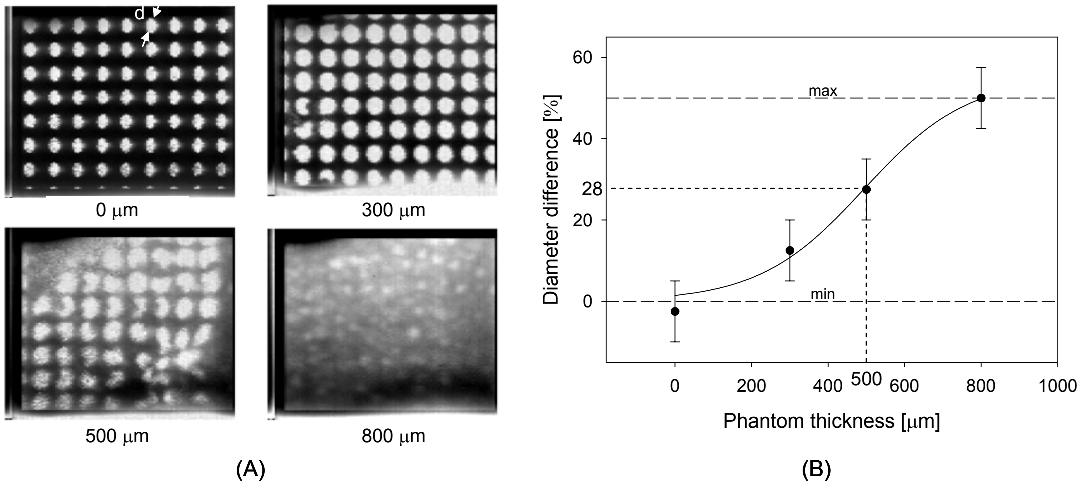

Fig. 3.17 (A) Mask pattern images at various opaque gel thickness, and (B) plot of difference in image hole diameter to true diameter at different gel thickness.

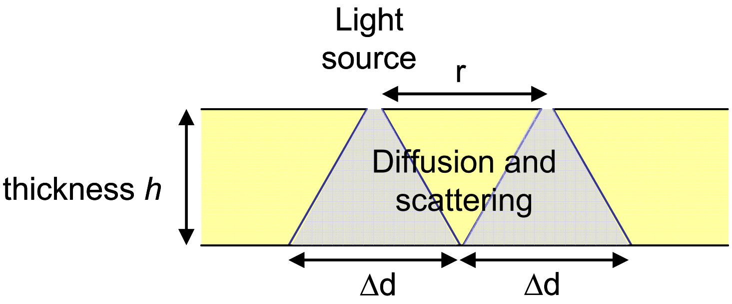

Fig. 3.18 Light from the two point light source is diffused and scattered in the phantom before it reaches the image sensor. The minimum resolvable pattern is given by Rayleigh's criterion when *r* is reduced such that the images overlap as shown. At this point, $r = \Delta d$

the experiment, a brain tissue phantom (see §4.3 for details) was used. A 50 μm thick stainless steel mask consisting of holes 100 μm in diameter with 150 μm pitch was placed on top of the phantom medium of different thickness. Uniform 470 nm monochromatic light was irradiated from above. The experimental setup is shown in Fig. 3.16. The imaged pattern at different thickness is shown in Fig. 3.17 (A). The edge of the holes is determined from the binarized image obtained by the threshold operation at the mid-level of full 255 gray scales. The hole diameter *d* is then measured by counting the pixels across the hole. The hole diameter is calculated based on the pixel size of 7.5 μm. The difference between the imaged hole diameter and the true diameter (100 μm) at different gel thickness is plotted in Fig. 3.17 (B). From this plot, it is observed that about 28 % increase of the true size of a light source as irradiated from the mask holes is observed when the light is scattered and diffused through the 500 μm thick phantom medium. The minimum resolvable spatial resolution can be deduced from the experimental data based on the Rayleigh's criterion as shown in Fig. 3.18. From the experimental result, it is shown that for a 500 μm thick slice, the minimum resolvable pattern is about 28 μm (an increase of 28% for a 100 μm hole pattern). This represents a four fold decrease in imaging resolution as the pixel size is 7.5 μm. However, even at this resolution, it is still sufficient for in vivo observing of neuronal assemblies such as the hippocampus which has size in the mm order.

3.4 Packaging for On-chip Fluorescence Imaging

As described in §3.2.3, fluorescence detection using a photosensor was performed by limiting the amount of excitation light onto the photodiode while maximizing the amount of fluorescence emission onto the photodiode. The same method, however, cannot be applied for an array of photosensors. For fluorescence imaging, especially for the on-chip imaging configuration, we have adopted the use of a color filter that selectively filters out the excitation light that is directly incident onto the image sensor. This color filter is spin-coated onto the image sensor as described below.

3.4.1 Packaging Method

A bare image sensor chip as thin as 150 μm was used. The chip was bonded to a 100 μm thick flexible polyimide substrate. The substrate has pre-printed conductive wiring for interfacing between the chip and the measurement equipment. It has to be flexible and biocompatible for the surgical insertion of an embedded sensor device into the living body. The bonding pads on the chip were then wire-bonded to the polyimide substrate and the chip was then sealed in an optically transparent and water-proof epoxy resin film to protect it from the biological environment. Finally, a color filter is spin-coated onto the sensor device. The filter is intended to block off the excitation light allowing only the fluorescent emission to reach the image sensor. The thickness of the fully packaged device is about 350 μm while its width is about 2.7 mm as shown in Fig. 3.19. The entire device including the substrate is as light as 0.3 g making it suitable for embedding into small animals such as a mouse.

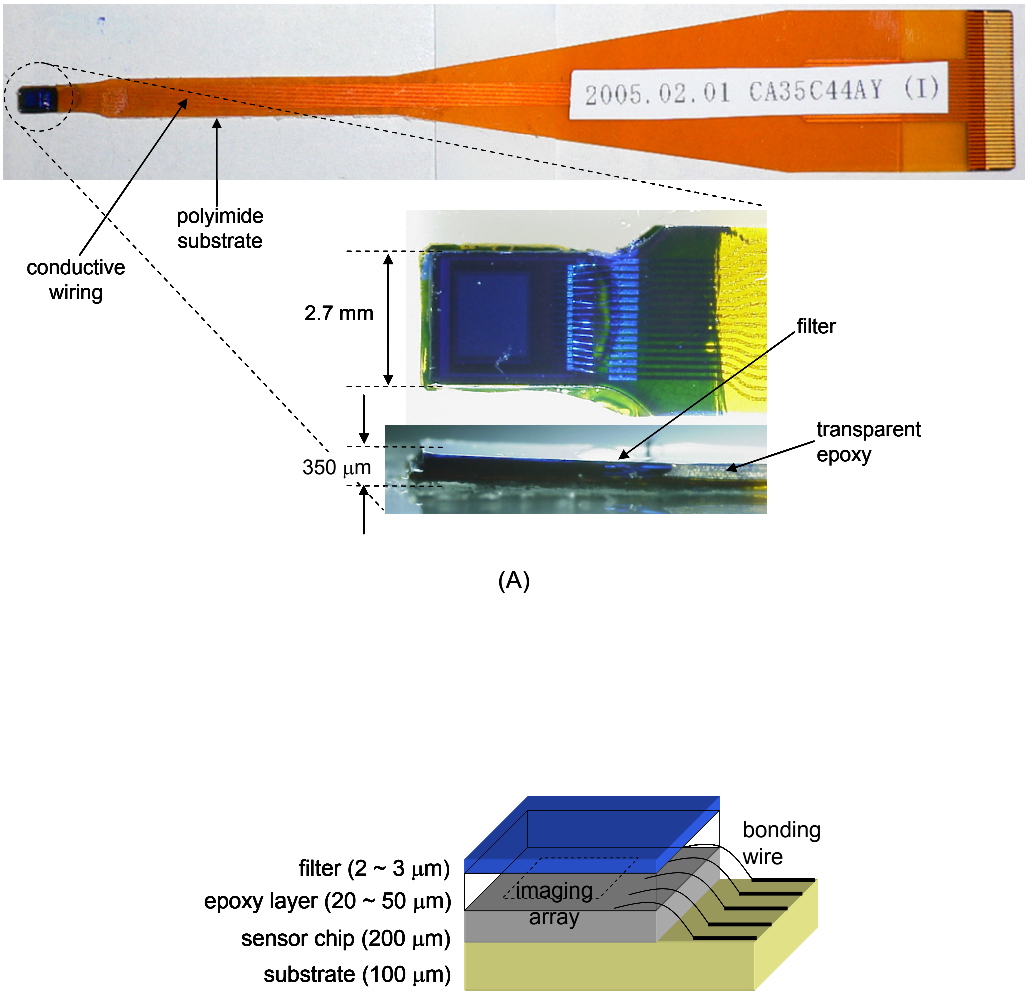

Fig. 3.19 (A) Fully packaged chip coated with blue filter. Inset shows zoomed up view of image sensor. (B) Diagram of the cross sectional thickness profile is shown at the bottom.

The packaged device was tested for more than 3 months and found to be functional without degradation in performance. This indicates that this packaging technique is suitable for chronic in vivo experiment. This is important when continuous recording in animals is required for an extended amount of time. Although the present device has not undergone extensive biocompatibility tests, acute experiments performed using devices developed with a similar packaging technique have shown successful operation in various biological environments [13-15]. As biocompatibility issues have not been fully studied, further work is needed in this area.

3.4.2 Filter and Fluorophore Spectrum

Two color filters are used for filtering the excitation light. A red filter which enables the light above 600 nm to pass, and a blue filter which allows the 460 nm light to pass through relatively unattenuated. These filters offer high selectivity for the fluorescence emission of

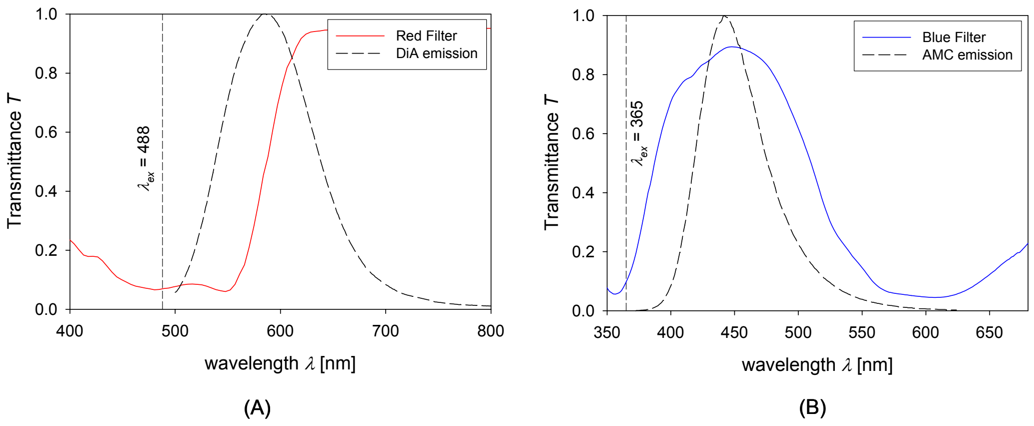

Fig. 3.20 (A) Comparison between red filter transmittance spectrum and DiA fluorescence spectrum. (B) Comparison between blue filter transmittance spectrum and AMC fluorescence spectrum.

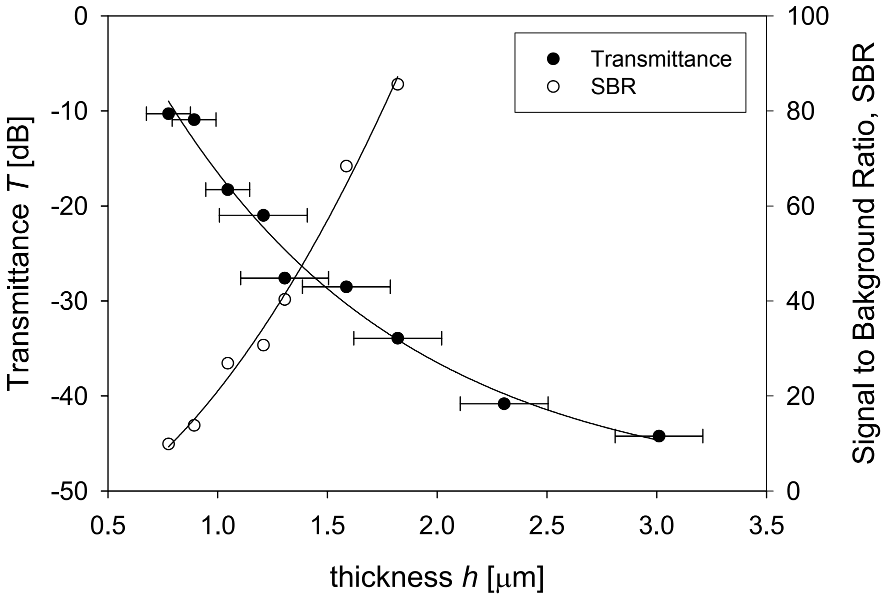

Fig. 3.21 Transmittance of fluorescence and signal-to-background ratio measurement as a function of the filter coating thickness.

4-(4-(dihexadecylamino)styryl)-N- methylpyridinium iodide (DiA Molecular Probes, USA) and 7-amino-4-methylcoumarin (AMC, 3099-v Peptide Institute, Japan) as shown in Fig. 3.20. Application of multiple coating of the filter results in a decrease of the transmittance of excitation light. Using this process, a minimum transmittance of -44 dB which is comparable to discrete filters used in fluorescence microscopes was achieved. Also, by defining the signal-to-background ratio (SNB) as the ratio of transmitted fluorescence light at 470 nm to transmitted excitation light at 365 nm, a graph showing its relationship to the filter thickness is plotted in Fig. 3.21. From this result, it is seen that the SNB increases with the thickness of the filter.

3.4.3 Fluorescence Detection Sensitivity

Using the packaged device which is coated with blue resist, we measured its photosensitivity and fluorophore detection sensitivity. The photosensitivity of the image sensor is measured using a monochromatic light source of wavelength 470 nm. This wavelength is used as it represents the peak wavelength of the AMC fluorophore emission which is comparatively unattenuated by the filter. Fig. 3.22 (A) shows the characteristic sensitivity profile as the light intensity and the frame time of the image sensor are varied while Fig. 3.22 (B) shows the same result when the signal level is plotted against light intensity at various frame times. It is observed that the sensitivity of the image sensor increases with frame time at the lower light intensity region. This implies that low light intensity resulting from low fluorescence can be measured with the higher sensitivity by increasing the frame time. In the experiment, the analog current output from the chip is used. The output is measured as the digitized photodiode voltage. These voltages represent the 12-bit (0 to 4095) values from the output of the A/D converter and are shown as signal level without units.

Finally, the fluorescence sensitivity of the image sensor was measured. Due to the fact that the static measurement of the fluorophore is made, the image sensor was operated in pulse modulation mode. This enabled more rigorous quantification of the image sensor characteristic. For the fluorescence sensitivity measurement, a fluorescence reference standard AMC solution was used. Pure water was used to dilute the original (stock) 10 mM AMC solution forming AMC solution of various concentrations. These were introduced onto the surface of the device via a microtube. The microtube reduces evaporation rate of the AMC solution compared to injection directly onto the sensor surface. This enabled stable readings to be taken for a prolonged measurement period. The excitation light was provided by a 500 μm PMMA light fiber with one end coupled to a 350 nm light bandpass-filtered light from an Hg lamp light

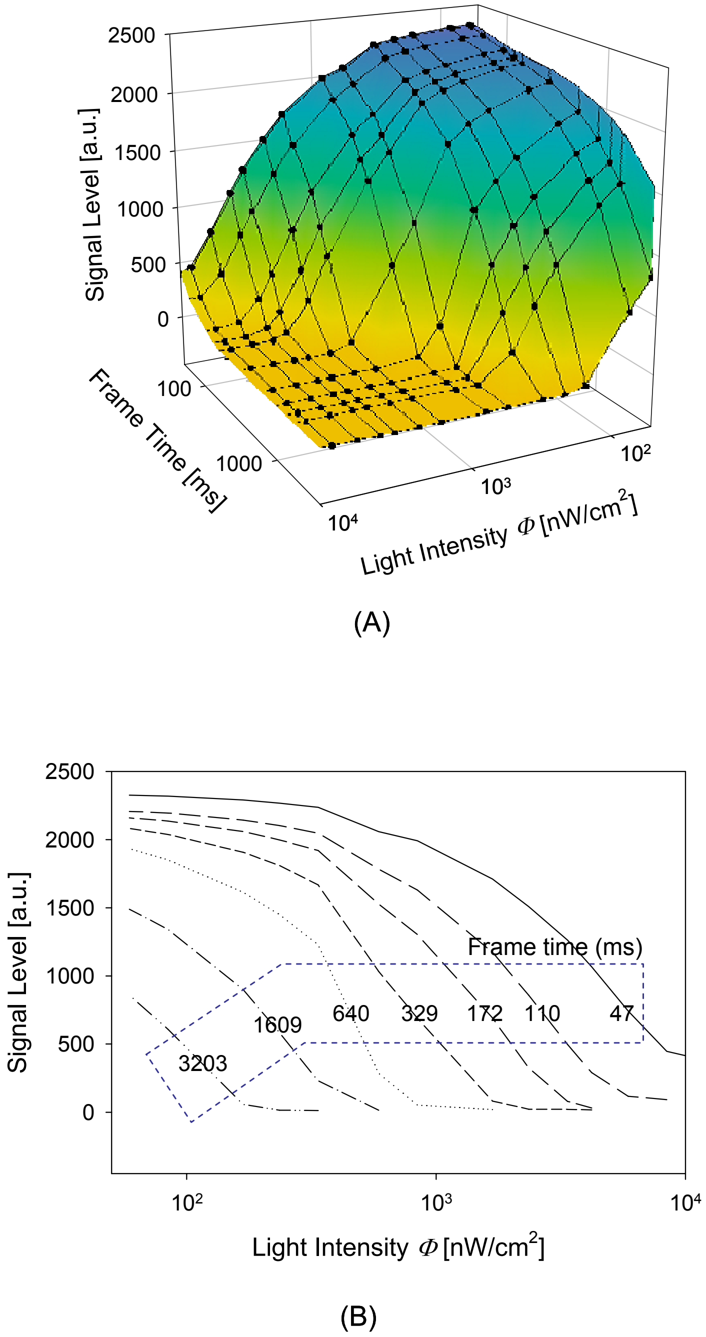

Fig. 3.22 (A) Photosensitivity of packaged image sensor with 470 nm illumination light for various frame times, and (B) an increase in frame time results in higher integration time thus enabling higher sensitivity measurement at the low light intensity region (legend in the graph refers to frame time in ms).

source. Fig. 3.23 (A) shows the device used in the experiment and Fig. 3.23 (B) shows the fluorescence sensitivity measurement result. From the result, capability of the image sensor for measuring AMC concentration down to 1 μM is confirmed. By using eq. (3.4), close fitting can be obtained as,

$$t_d = \frac{6854.8}{\left(1+0.0028C\right)^{2.473}}, \tag{3.8}$$

where, t_d is the output signal in ms, and C is the AMC concentration in μM. The fitting parameters α, β, and γ are 6854.8 ms, 0.0028 μM^{-1} and 2.473, respectively. Because the same fitting equation is used, this shows a direct correlation between the fluorescence emission and photogenerated current. The increase in the value of γ shows the reduced dynamic range of the image sensor compared to measurement using a single photosensor as expected. From this result, it can be concluded that, the measured output signal is directly proportional to the incident light intensity. And that the light intensity is related to the fluorescence signal in a linear fashion. Hence, an increase in signal from the actual measurement can be used as a measure of the amount of fluorophore.

3.5 Discussion

The CMOS photosensor sensitivity for light detection was shown experimentally in §3.2.2. A macro model was developed to explain the photosensitivity measurement. The argument presented has three important implications. First, eq. (3.1) represents an accurate macro model describing the CMOS photosensing characteristic. This is confirmed and verified by the experimental measurement data. Second, the proposed eq. (3.4) is a suitable fitting equation for eq. (3.1), and hence can be used as a measure for quantifying the various unknown parameters without performing experiments. As shown in eq. (3.4), the model is also appropriate for

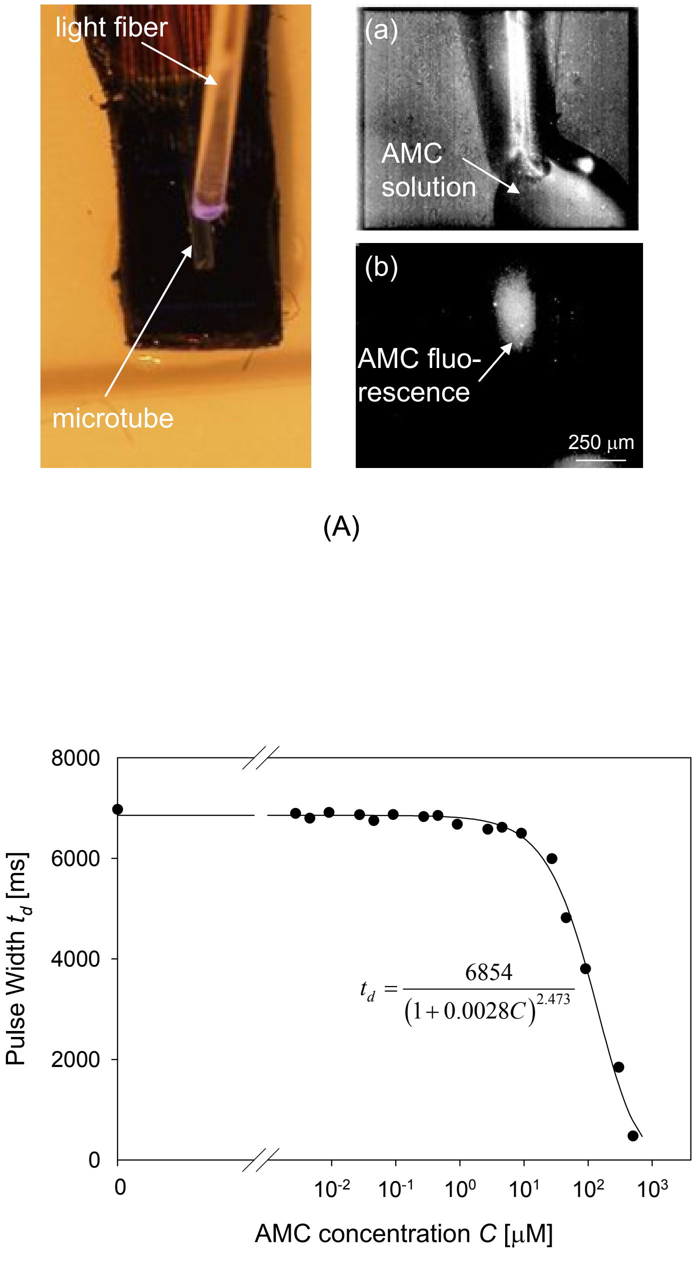

(A)

(B)

Fig. 3.23 (A) Experiment setup for fluorophore sensitivity measurement showing the imaging device with attached microtube and excitation light provided by the tip of a 500 mm PMMA light fiber. Right images show (a) captured image with halogen lamp lighting, (b) captured image with fiber light illumination only. (B) AMC fluorescence sensitivity measurement using image sensor. The device was operated at a frame rate of 0.16 fps.

analyzing the characteristics of the image sensor in fluorescence imaging. This is important when characterizing a new light source for light intensity linearity. Finally, by employing this understanding of the CMOS photosensor, optimization for highest sensitivity can be achieved without exhaustive iterative design and testing. Hence, future work in CMOS image sensor will benefit greatly from this study.

The image sensor architecture that is developed can be improved in terms of the device sensitivity and the imaging frame rate. Given that many schemes have been reported to increase the sensitivity and bandwidth of CMOS image sensors [16-22], further improvement can be expected. One way of increasing the frame rate is by implementing parallel and multiplexed signal read-out. Furthermore, by reducing the imaging region to a smaller region of interest also imaging frame rates can be improved [23, 24]. Sensitivity can be increased by increasing the fill-factor of the pixel using deeper sub-micron fabrication technology. Also, work leading to optimized photosensing architecture for weak-light sensing has been reported [25-27].

3.6 Summary

A CMOS photosensor was evaluated for the fluorescence detection capability. Using photosensing in the pulse modulation mode, a high temporal resolution with a wide dynamic range has been verified. It was found that the photosensor is capable of detecting light intensity of 1 nW/cm^2 with a dynamic response of 120 dB. A macro model equation was developed for understanding the photosensing mechanism. When used to measure the fluorescence of AMC, it was found that the photosensor is able to detect a minimum AMC concentration of 1 nM. In order to implement high spatial resolution imaging, a 2D array of photosensors is designed and fabricated. Currently the pixel size is 7.5 μm, and thus the image sensor is expected to provide a theoretical spatial resolution of similar dimensions. Further investigation shows that on-chip imaging of inside a turbid medium reduces the imaging spatial resolution. It was found that light scattering in the phantom medium does not reduce the image resolution considerably if the imaging depth is kept below 500 μm. When implemented on such a CMOS image sensor, it is realized that the pulse modulation photosensing mode operates at a comparably low frame rate. By utilizing the analog current output and implementing off-chip A/D conversion, an order of magnitude improvement in the imaging frame rate was achieved. Also, by developing a novel packaging technique for the image sensor, an on-chip fluorescence imaging device was developed. The device was evaluated for fluorescence sensing and measurement. The fully packaged imaging device is used to demonstrate in vitro and in vivo imaging of the mouse brain as will be described in the next chapter. The main objective of this work is to show that by a CMOS image sensor can be applied to fluorescent imaging, and this work has led to the development of a device that is capable of on-chip fluorescence imaging. This has paved the way for further development in the image sensor design. Potential applications for the imaging device include integration with other systems like microfluidic devices for rapid chemical analysis.

References

[1] R. P. Haughland, *Handbook of fluorescent probes and research products*, 9th ed., Eugene: Molecular Probes, 2002, pp. 1-6.

[2] J. P. Golden, F. S. Ligler, “A comparison of imaging methods for use in an array biosensor,” *Biosens. Bioelectron.*, vol. 17, pp. 719-725, Sep. 2002.

[3] J. R. Janesick, "Lux transfer: CMOS versus CCD," in *Proceedings of SPIE*, Sensors and Camera Systems for Scientific, Industrial, and Digital Photography Applications III, M. M. Blouke, J. Canosa, N. Sampat, ed.s, Apr. 2002, vol. 4669, pp. 232-249.

[4] W. Yang, “A wide-dynamic-range, low-power photosensor array,” in *Proceedings IEEE* International Solid-State Circuits Conference ISSCC, Feb. 1994, pp. 230-231.

[5] F. Andoh, H. Shimamoto, Y. Fujita, “A digital pixel image sensor for real-time readout,” *IEEE Trans. Electron Devices*, vol 47, pp. 2123-2127, Nov. 2000.

[6] J. Ohta, N. Yoshida, K. Kagawa, M. Nunoshita, “Proposal of application of pulsed vision chip for retinal prosthesis,” *Jpn. J. Appl. Phys.*, vol. 41, pp. 2322-2325, Apr. 2002.

[7] A. Kitchen, A. Bermak, A. Bouzerdoum, “PWM digital pixel sensor based on asynchronous self-resetting scheme,” *IEEE Electron Device Lett.*, vol. 25, pp. 471-473, Jul. 2004.

[8] S. G. Chamberlain, V. K. Aggarwal, “Photosensitivity and characterization of a solid-state integrating photodetector,” *IEEE J. Solid-State Circuits*, vol. SC-7, Apr. 1972.

[9] T. Tokuda, D. C. Ng, H. Okamoto, K. Kagawa, J. Ohta, M. Nunoshita, “Wide dynamic range pulse modulation image sensor for on-chip bioimaging applications,” in *Proc. IEEE Sensors*, Oct. 2004, vol. 2, pp. 818-821.

[10] S. Ehrenfri, “0.6 µm CMOS CUP process parameters,” Austria Mikro System International, Document #: 9933011 B, Oct. 1998. (confidential)

[11] H. Okamoto, “バイオイメージング向けパルス変調方式 CMOS イメージセンサの研究,” *M.Sc. dissertation*, Nara Inst. Sc. Tech., Mar. 2004 (in Japanese).

[12] T. Tokuda, D. C. Ng, H. Okamoto, M. Matsuo, A. Yamamoto, K. Kagawa, J. Ohta, M. Nunoshita, H. Tamura, S. Shiosaka, “Pulse modulation image sensor for in vitro brain

imaging," *ITE Technical Report*, vol. 28, pp. 15-18, Mar. 2004 (in Japanese).

[13] T. Furumiya, D. C. Ng, K. Yasuoka, K. Kagawa, T. Tokuda, M. Nunoshita, J. Ohta, "Functional verification of pulse frequency modulation-based image sensor for retinal prosthesis by in vitro electrophysiological experiments using frog retina," *Biosens. Bioelectron.*, vol. 21, pp. 1059-1068, Jan. 2006.

[14] T. Tokuda, Y.-L. Pan, A. Uehara, K. Kagawa, M. Nunoshita, J. Ohta, "Flexible and extendible neural interface device based on cooperative multi-chip CMOS LSI architecture," *Sensors Actuators A*, vol. 122 pp. 88-98, May 2005.

[15] Ohta J, Tokuda T, Kagawa K, Terasawa Y, Ozawa M, Fujikado T, Tano Y. "LSI-based stimulus electrodes for retinal prosthesis," presented at the 2nd DOE Int. Symp. Artificial Sight, Ft. Lauderdale, Florida, USA, Apr. 29, 2005.

[16] O. Yadid-Pecht, E. R. Fossum, "Wide intrascene dynamic range CMOS APS using dual sampling," *IEEE Trans. Electron Devices*, vol. 44, pp. 1721-1723, Oct. 1997.

[17] T. Lulé, S. Benthien, H. Keller, F. Mütze, P. Rieve, K. Seibel, M. Sommer, M. Böhm, "Sensitivity of CMOS based imagers and scaling perspectives," *IEEE Trans. Electron Devices*, vol. 47, pp. 2110-2122, Nov. 2000.

[18] Y. Perelman, R. Ginosar, "A low-light-level sensor for medical diagnostic applications," *IEEE J. Solid-State Circuits*, vol. 36, pp.1553-1558, Oct. 2001.

[19] D. Stoppa, A. Simoni, L. Gonzo, M. Gottardi, G.-F. Dalla Betta, "Novel CMOS image sensor with a 132-dB dynamic range," *IEEE J. Solid-State Circuits*, vol. 37, pp. 1846-1852, Dec. 2002.

[20] E. Culurciello, R. Etienne-Cummings, K. A. Boahen, "A biomorphic digital image sensor," *IEEE J.Solid-State Circuits*, vol. 38, pp. 281-294, Feb. 2003.

[21] Y. Oike, M. Ikeda, K. Asada, "A 120 × 110 position sensor with the capability of sensitive and selective light detection in wide dynamic range for robust active range finding," *IEEE J. Solid-State Circuits*, vol. 39, pp. 246-251, Jan. 2004.

[22] H. Eltoukhy, K. Salama, A. El Gamal, M. Ronaghi, R. Davis, "A 0.18μm CMOS 10-6lux bioluminescence detection system-on-chip," in *Proc. IEEE Intl. Solid-State Circuits Conference ISSCC*, Feb. 2004, vol. 1, pp. 222-524.

[23] S. C. Lauxtermann, A. Biber, P. Schwider, P. Metzler, P. Seitz, "Megapixel CMOS imager with charge binning," in *Proceedings of SPIE*, Sensors and Camera Systems for Scientific,

Industrial, and Digital Photography Applications II, M. M. Blouke, J. Canosa, N. Sampat, ed.s, May 2001, pp. 85-92.

[24] R. Etienne-Cummings, P. Pouliquen, M.A. Lewis, “Single chip for imaging, colour segmentation, histogramming and template matching,” *Electron. Lett.*, vol. 38, p. 172-174, Feb. 2002.

[25] E. K. Bolton, G. S. Sayler, D. E. Nivens, J. M. Rochelle, S. Ripp, M. L. Simpson, “Integrated CMOS photodetectors and signal processing for very low-level chemical sensing with the bioluminescent bioreporter integrated circuit,” *Sensors Actuators B*, vol. B85, pp. 179-185, Jun. 2002.

[26] R.A. Yotter, M.R. Warren, D.M. Wilson, “Optimized CMOS photodetector structures for the detection of green luminescent probes in biological applications,” *Sens. Actuators B*, vol. 103, pp. 43-49, May. 2004.

[27] K. Salama, H. Eltoukhy, A. Hassibi, A. El Gamal, “Modeling and simulation of luminescence detection platforms,” *Biosens. Bioelectron.*, vol. 19, pp. 1377-1386, Jun. 2004.

Chapter 4

In vitro and In vivo Fluorescence Imaging

In this chapter, I describe the application of a packaged CMOS image sensor for in vitro and in vivo imaging. The 176×144-pixels (QCIF) CMOS image sensor fabricated and described in the previous chapter is used for this purpose. I demonstrated in vitro on-chip fluorescence imaging of a 400 μm thick mouse brain slice detailing the hippocampus. A morphological study using the image sensor compares favorably to the image captured by conventional microscopes. In order to study in vivo imaging, I also developed a brain phantom media. The medium has mechanical rigidity and optical property similar to the mouse brain. Feasibility of imaging the released fluorophore inside the phantom medium was demonstrated. It is shown that light scattering in the phantom medium does not reduce the image resolution considerably, if the depth is kept below 500 μm. Also, in situ fluorophore measurement shows that detection through the turbid medium up to 1 mm thickness is possible. Finally I have successfully demonstrated imaging deep into the hippocampal region of the mouse brain where quantitative fluorometric measurements was made. Although the device is designed specially for in vivo imaging of the mouse hippocampus to study its neuronal activity, a wide-range of applications are foreseen in the biomedical and pharmaceutical fields.

Keywords: CMOS image sensor, fluorescence, imaging, in vitro, in vivo, fluorometric, brain

4.1 Introduction

Bioimaging forms a subset of biosensing methods which are applied for studies in the biological world [1, 2]. As shown in the chart in Fig. 4.1, methods for biological imaging can be further classified into sacrificial and non-sacrificial methods. In vitro and in vivo imaging represents the opposite ends of the spectrum for these methods. Tissue slice is found where sacrificial methods are employed. From the tissue extracts, chemical composition can be further determined by using Fourier Transform Infrared Spectroscopy (FTIR), or Mass Spectrometry (MS). On the opposite end of the spectrum, non-sacrificial methods like functional magnetic resonance imaging (fMRI), positron emission tomography (PET), and optical tomography (OT) are widely used in the medical field for their diagnostic capability in studying the living body. These tools are the preferred method for imaging animals and are non-invasive and cause almost no injury the subject being studied. However, these tools are expensive and require the subject to be perfectly still during imaging. Compared to those methods, non-sacrificial but invasive methods enable chronic measurement of the living animal where injury the subject is minimized during observation. These methods include the use of electrodes and optical fibers. I focus our work in this area. Our approach is to use a CMOS image sensor for imaging.

Of the all living tissues, the brain must be the most studied due to our fascination with its functions and complexity since antiquity [3]. Efforts to unravel the secrets of the brain have led to the development of many imaging methods. Table 4.1 lists some of the existing brain imaging methods. Of these methods, the combination of in vitro and in vivo imaging with fluorescence methods has brought about great advances in this area. Currently, the tools available for fluorescence study are still limited to fluorescence microscopes. Many researchers have resorted to sacrificing an animal in order to study changes deep inside the structural layers of the brain.

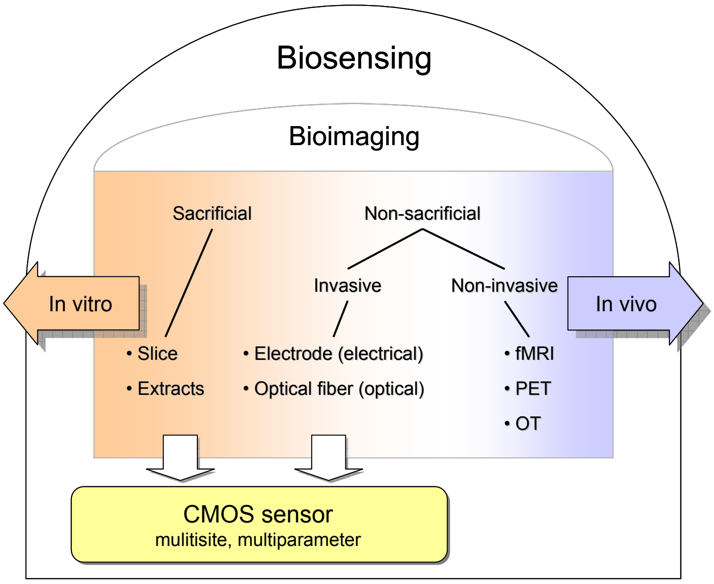

Fig. 4.1 Application using CMOS image sensor compared to current in vitro and in vivo imaging techniques

These methods involve staining live animal brains and extracting the brain for further study under the microscope. The limitation of this method is obvious, as data collected using these in vitro studies represent discontinuous stages whereby correlation between animal behaviors and functional activities that occur in the brain proves to be difficult and time consuming. Recently efforts to miniaturize these conventional microscopes have led to development of devices small enough to image the brain of small animals [5, 6]. However, due to the limitation of photon penetration depth into biological tissues, these devices cannot image deep inside the brain. Optical tomography has shown promise in imaging live animals but is limited to imaging of shallow depths below the surface and requires immobilization of the animal [7, 8]. Recently, light fiber for recording of intracellular calcium changes in deep brain structures had been reported [9, 10]. However, this method lacked 2D imaging capability in the spatial domain. The use of a bundled fiber for imaging is not an option as this will lead to severe damage and injury to the subject during invasive imaging of small animal brain.

Realizing that development of an alternative method for in vitro and in vivo real-time

Table 4.1 Comparison among existing brain imaging techniques [4].

Methods	Energy Source	Spatial resolution (mm)	Temporal resolution (s)	Constraints
Structural MRI	Radio	1	N/A	Immobilization
*f*MRI	Radio	4-5	4-10	Immobilization
MR spectroscopy	Radio	10	10-100	Immobilization
Optical Tomography	Near IR or vis	5	1	some immobilization
Nuclear (PET/SPECT)	X-ray	5-10	60-1000	Radiation danger
Transcranial magnetic stimulation	Magnetic	10	0.01	Immobilization
EEG/MEG	Electrical	10	0.01	Artifact, no localization

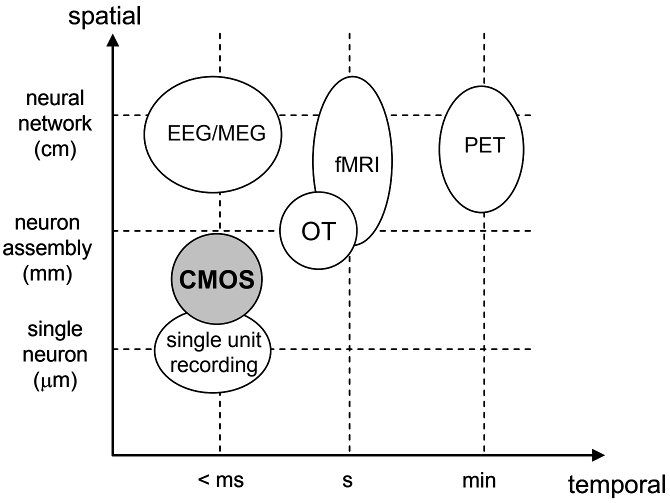

Fig. 4.2 Region of applicability of CMOS image sensor for brain imaging.

imaging of the brain would greatly benefit the neuroscience community, I am exploring the ways that a CMOS image sensor can be utilized. By implementing a CMOS image sensor for imaging the brain, a range of applications that lies between the established methods for in vitro observations and non-invasive in vivo imaging would be made possible. Furthermore, its region of applicability (both temporal and spatial characteristics has been described in detail in Chapter 3) lies beyond the serviceable area offered by existing imaging methods as shown in Fig. 4.2. Hence, there is a wide range of unexplored and yet to be identified applications that will benefit from its development once the method has been established.

In this chapter, work leading to the development and verification of a CMOS imaging device for in vivo imaging of the brain is presented. This includes a choice of the reaction model for fluorescence detection in the brain, and development of a brain phantom for in vivo imaging verification and in vitro brain slice imaging. Initially, much work was done to verify the capability of the imaging device in the in vivo environment. This was performed by using a suitable enzyme assay inside a specially prepared brain tissue phantom. Successful verification of this motivated me towards actual in vitro and in vivo imaging experiments involving the brain of the mouse. As described in this chapter, I have successfully imaged and quantitatively measured fluorescence in real time inside the intact mouse brain. This was accomplished by using the reaction model involving the serine protease fluorogenic substrate. In addition to the packaged device in Chapter 3, the imaging device was modified to include a microtube for injection of substrate in the brain.

4.2 Experimental Methods

As explained in Chapter 3, fluorescence imaging is a high specificity method for studying bio-molecular interactions. This work focuses on the application of a CMOS image sensor for fluorescence imaging. The final aim is to demonstrate viability of the CMOS image sensor for in vivo fluorescence imaging. In order to achieve this aim, experimental work progresses from in vivo verification using a brain tissue phantom which leads to the use of the CMOS image sensor for in vivo imaging. Apart from that, in vitro imaging using the device is also demonstrated.

4.2.1 Fluorophore used in Brain Imaging

In imaging of the brain, a number of fluorophore species are used. In particular, the UV excitable fluorophore, 7-amino-4-methylcoumarin (AMC) and the longer wavelength excitable fluorophore, 4-(4-(dihexadecylamino)styryl)-N-methylpyridinium iodide (DiA) are used. DiA is a lipophilic fluorescent dye which diffuses laterally within the plasma membrane, resulting in staining of the entire neuronal cell. Here, it is used as a generic staining dye to discern the brain structure, especially the hippocampus. Its peak excitation (absorbance) and emission wavelengths are 456 nm and 590 nm, respectively. These comparatively longer wavelengths enable the lights to penetrate deeper inside the brain (see Chapter 2).

AMC is a versatile molecule which is used in combination with other molecules to form a water soluble fluorophore substrate 4-methylcoumarin-7-amide (MCA) derivative. When used to prepare peptidase substrates, the amide has shorter wavelength absorption and emission spectra compared to the hydrolyzed amine (AMC) product [11]. This forms the basis for fluorometric studies using AMC derived substrates. The amine product when excited at 365 nm emits fluorescence with a maximum wavelength of about 470 nm. Two different reaction models were used to verify in vitro and in vivo imaging of the mouse brain.

4.2.2 AMC-derived substrate for functional study of serine protease

It has been established that serine protease plays a role in synaptic plasticity in the brain. And that brain plasticity is the basis for the brain memory and learning functions. The major intrinsic circuitry of the hippocampus consists of an excitory trisynaptic cascade of the dentate, CA3 and CA1 subregions. The expression of serine protease in the brain follows the mechanism as shown in Fig. 4.3. The most studied serine protease is the tissue-type plasminogen activator (tPA) [12]. In the normal brain serine protease is expressed naturally following certain neuronal

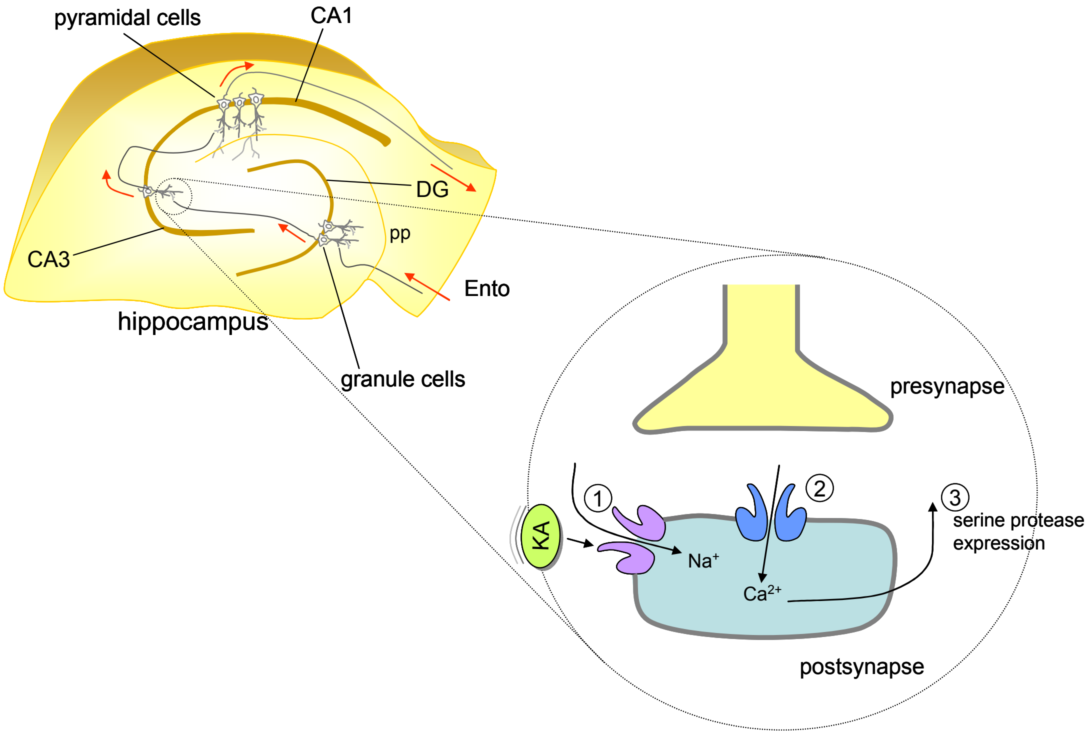

Fig. 4.3 Diagram of hippocampus structure (right hemisphere) showing its intrinsic trisynaptic connections. Fibers from the enthorhinal cortex (Ento) project through perforant path (pp) to the dentate gyrus (DG); granule cells from the DG project to the CA3 region, which in turn projects to the CA1 region; pyramidal cells from the CA1 region then project to the subiculum (SB), which then projects back to the entorthinal cortex. At the CA3 to CA1 cell synapse, the following molecular events is believed to take place; first, KA ligands to KA receptor ion channel which then opens to let Na^+ into the cell. This depolarizes the cell which then opens the voltage-gated Ca^{2+} channel (or NMDA receptor). This causes postsynaptic excitation which then leads to activation of serine protease via Ca^{2+} signalling mechanism.

stimulations. However, this can also be induced artificially using kainic acid (KA). It has been shown that tPA expression induced in such a way causes epileptic seizures in normal mouse [13]. Another form of serine protease, neuropsin (NP, also known as Kallikrein-8, Brain Serine Protease-1, or neurotrypsin, etc) is believed to play a role in plasticity of the brain [14, 15]. While tPA can be found in the entire brain, NP is relatively localized in the hippocampus only. Two types of reaction models are used to study these serine proteases. One involves the use of a synthetic fluorogenic substrate with a QGSK oligopeptide and the 4-methylcoumarin-7-amide (MCA) fluorogenic derivative. This substrate identified as QGSK-MCA is used as a substitute material to simulate NP activity in vitro. Because QGSK-MCA can be used as a surrogate material to study NP activity in vitro, this reaction model is a convenient tool when used for in vivo fluorescence imaging verification. The other reaction model uses the Boc-Val-Pro-Arg-4-methylcoumarin-7-amide (VPR-MCA) and Pyr-Gly-Arg-4-methylcoumarin-7-amide (PGR-MCA). These substrates are used to detect the presence of tPA and NP in vivo.

4.2.3 QGSK-MCA: The 1st Reaction Model

The serine protease, neuropsin is believed to play a major role in synaptic plasticity in the hippocampus. Neuropsin is secreted into the extracellular space in an inactivate precursor form and is activated by the processing of a 4-amino acid peptide (QGSK) after its release. NP is believed to be activated by an unidentified NP activator (NPA) after theta-burst stimulation in the hippocampus. In this study, a synthetic fluorogenic substrate, QGSK-MCA is used to simulate neuropsin. Detection of this substrate is performed by treatment with a peptidase, lysyl endopeptidase (lys-C) which cleaves the peptidal bond, hence releasing the fluorometrically detectable aromatic amine, AMC as shown in Fig. 4.4. In a separate experiment, it was found

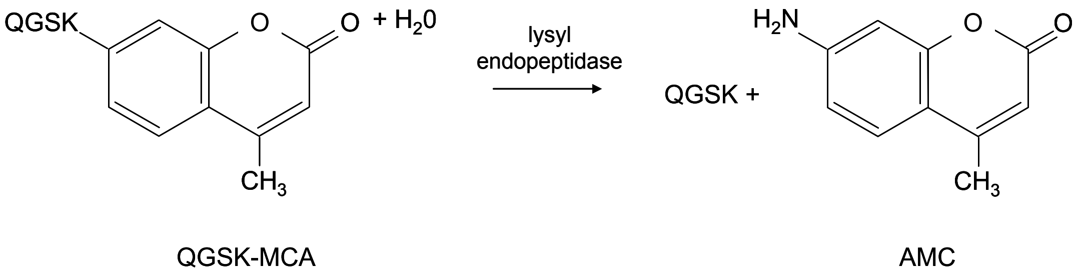

Fig. 4.4 Cleaving of synthetic substrate, QGSK-MCA by lysyl endopeptidase releases AMC which can be detected fluorometrically.

that this substrate has similar response to NP in its activated state whereby it was specifically cleaved by lys-C in vivo. Due to its highly fluorescence product, this substrate is used in combination with lys-C to serve as a convenient enzyme assay whereby imaging and quantitative measurement can be made. A specially prepared brain tissue phantom medium that can be used as an in vitro surrogate for in vivo brain tissues is developed as the platform for verifying fluorescence from the released AMC can be detected using the CMOS image sensor.

4.2.4 VPR-MCA and PGR-MCA: The 2nd Reaction Model

VPR-MCA and PGR-MCA are highly sensitive detectors for the serine protease tPA and activated NP, respectively. Once the proteases are expressed cellularly as described in Fig. 3, they can be detected immediately using these fluorogenic substrates. The substrates are hydrolyzed by the presence of the specific serine protease, whereby the AMC amine is released.as shown in Fig. Fig. 4.5. Fluorometric detection of AMC can then be used as a measure of the presence of the serine protease. It has been known that the expression of the serine protease can be induced artificially using KA. However, current methods employed to study the effect of KA induced serine protease activity does not allow the exact time course of

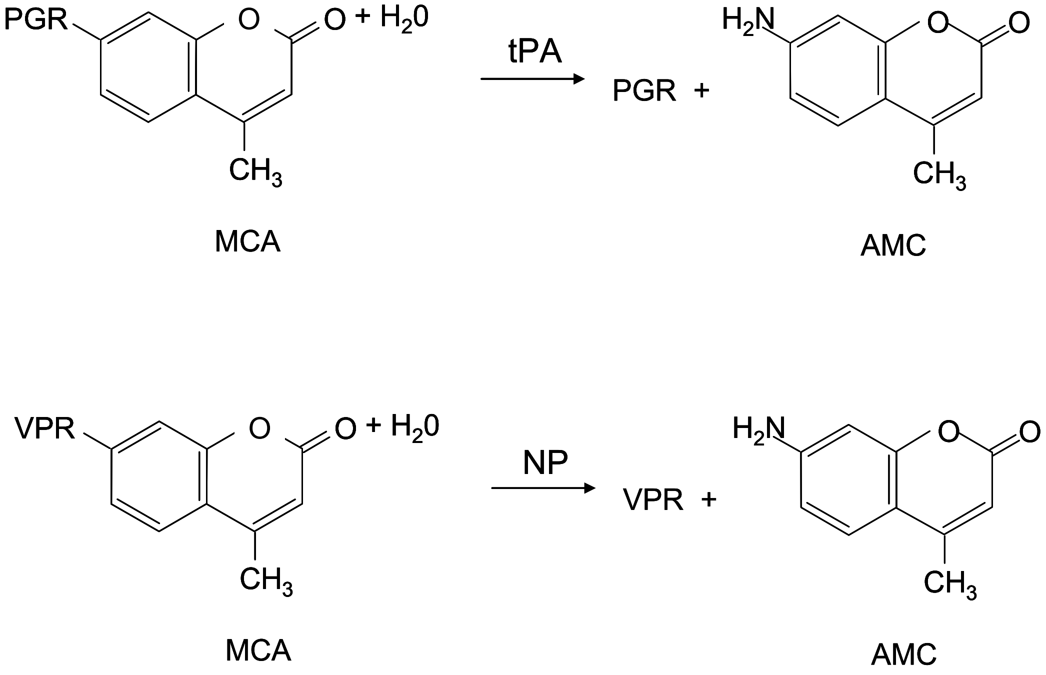

Fig. 4.5 The presence of tPA and NP causes the PGR-MCA and VPR-MCA substrates to release the AMC molecule which can be detected fluorometrically.

the events to be ascertain. Hence, development of a method to verify these events in real time would be greatly beneficial. Here, detection of serine protease in vivo is used as a model reaction to validate and verify the capability of the CMOS imaging device for generating useful results with regards to the function study of the brain. This study will be used as a platform to enable other work where molecular signaling pathways including brain plasticity can be independently verified.

4.3 Brain Tissue Phantom

In order to simulate the imaging condition inside the brain, a brain tissue phantom medium is developed. In this work, the phantom medium is used with the first reaction model as described in §4.2.3 to simulate in vivo imaging conditions inside the mouse brain.

4.3.1 Development of Brain Tissue Phantom and Comparison with Brain Tissue

The phantom medium prepared from agarose gel (Agarose S Nippon Gene, Japan) and skim milk (Snow Brand Milk Products, Japan) was used. A bulk gel block with a 1% agarose gel content was prepared by dissolving the gel in Tris buffer solution (pH7.5 100 mM). The content of skim milk in the gel was varied from 1% to 20%. In preparing the gel, vigorous shaking is required to ensure that the colloidal mixture of milk in the gel is uniform. The hardened gel block was then sliced into 400 μm thick slices by using a linearslicer (DSK-Pro7 Dosaka, Japan).

For comparison, brain samples from adult male ddY mice (SLC Co., Hamamatsu, Japan; 9 weeks old) were used. The animal was decapitated under urethane anesthesia and the brain was quickly removed and immersed in ice-cold artificial cerebrospinal fluid (ACSF) containing the following (in mM): 127 NaCl, 1.6 KCl, 1.24 KH_2PO_4, 1.3 $MgSO_4$, 2.4 $CaCl_2$, 26 $NaHCO_3$, and 10 glucose. It was then cut into coronal slices of 400 μm thickness with the linearslicer. The slices are fixed in 4 % paraformaldehyde in 0.1 M phosphate-buffered saline (PBS), and then washed with 0.1 M PBS. The slices of interest from the caudal diencephalon region were selected. From these slices, the transmittance of the gel and the brain slices was measured. A total of five brain slices were measured and their values averaged.

A collimated beam from a monochromator (M10-T Jasco, Japan) using a mercury lamp light source (VB-L10 Keyence, Japan) was directed onto the slice. The lamp was used due to the relatively high power in the UV wavelength region. The wavelength was scanned from 350 nm to 700 nm. The beam size was kept much smaller than the sample area to prevent side

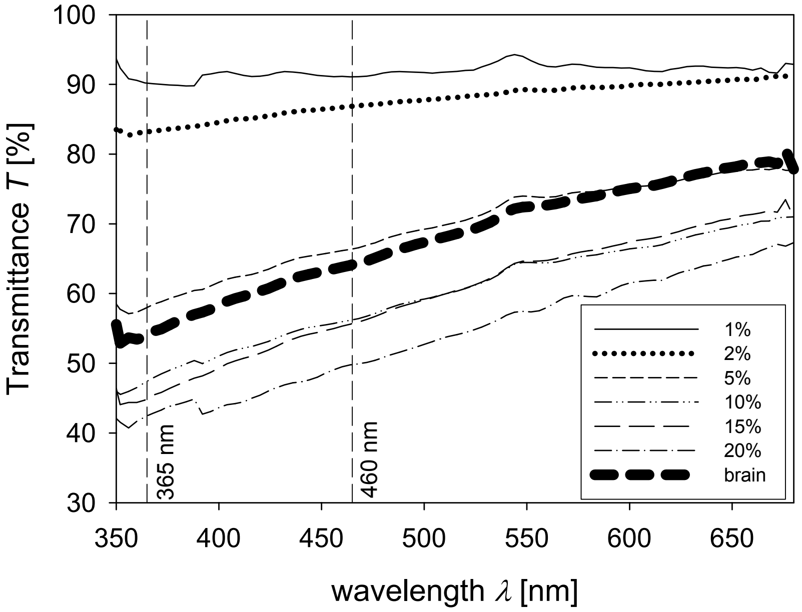

(A)

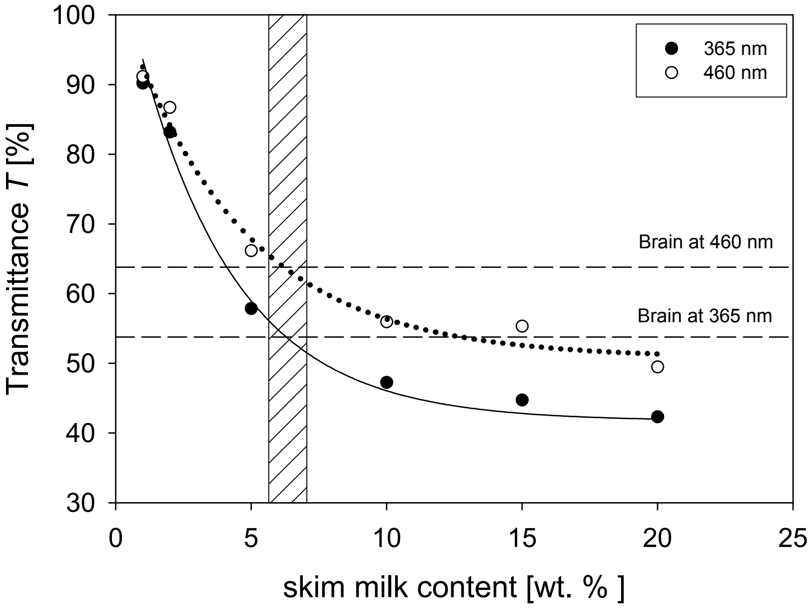

(B)

Fig. 4.6 (A) Transmittance spectrum of 400 µm thick phantom medium for various skim milk content. (B) Transmittance at 365 and 460 nm for 400 µm thick gel with various skim milk content. Comparison with brain transmittance at the same wavelengths shows that a skim milk content of 6.4 ± 0.2% enables a closest fit.

(boundary) effects but large enough to avoid microstructures in the tissue. The beam emerging from the opposite side of the slice was collected by a photodetector (S2281 Hamamatsu, Japan) and the photocurrent measured using a picoammeter (6514 Keithley Instruments, USA). The ratio between the photocurrent corresponding to the incident light and the emitted light was calculated for the entire scanned wavelength to obtain the transmittance spectrum. The transmittance spectrum for the gel and brain slices are shown in Fig. 4.6 (A). The readings within the measurement range shows that the transmittance of the phantom media varies in accordance to that of the brain slice as the wavelength increases. This verifies that the phantom medium can be used as a substitute for the brain in the subsequent experiments. When the transmittance values were plotted for different skim milk content as a parameter of the two wavelengths 365 and 460 nm corresponding to the maximum absorbance and emission wavelength of AMC respectively, a milk content of 6.4% with offset of about ± 0.2% is found to give the same transmittance value as that of the brain as shown in Fig. 4.6 (B).

4.3.2 Verification for In vivo Imaging

The purpose of performing in situ AMC imaging is to ascertain if the released AMC from the QGSK-MCA substrate can be detected by the image sensor. This will verify feasibility for in vivo biofluorescence imaging. Initial experiments which determine the dependence of the gel thickness were performed. This will give an indication for the optimal distance between the fluorescence source and the imaging device. Next, the lys-C concentration was varied to determine the minimum detectable level for a given experimental condition. Finally, using the information obtained, verification of in vivo imaging was performed using a mock-up system to mimic the imaging condition inside the brain. All the experiments were performed at room temperature.

Light propagation in biological tissues plays an important role in optical imaging. Due to the fact that a shorter light wavelength is more strongly diffused and scattered in the turbid medium, the optical fiber was positioned relatively far (1.5 mm) from the surface of the imaging device. In this position, the excitation light from the fiber was diffused and illuminated the entire image sensor surface. As the fluorescence emission light falls in the longer wavelength region, it is less likely to be scattered and therefore the fluorescence image will likely remain sharp. However, it was shown that superposition of fluorescence images results in image blurring. This problem is less pronounced for thin slices with thickness of less than 500 μm. For imaging in a bulk material, the problem may require a more complicated solution. One way to address this issue is by using a scanning light source and performing image reconstruction similar to the method employed in optical diffusion tomography. This way, a 3-D volume fluorescence image can be acquired [8]. The scanning light source can be realized using a bundled fiber and a fiber switch system to relay light or by mechanical scanning as demonstrated elsewhere [5]. In the current setup, by limiting the distance between the single fluorescence light source and the imaging device, imaging in the bulk material was demonstrated and quantitative data obtained.

i) Gel Thickness Dependence

In this experiment, two variables were studied; clear gel (agarose without milk content), and opaque gel (phantom medium) thickness. The first experiment involving clear gels served as visual verification of the fluorescence emission for the subsequent experiments using the opaque brain phantom. Because fluorescence light could be visually identified using a separate sensor and also by the naked eye. It was confirmed that the enzyme assay produced the desired fluorescence signal from the AMC. This served as the basis that can be

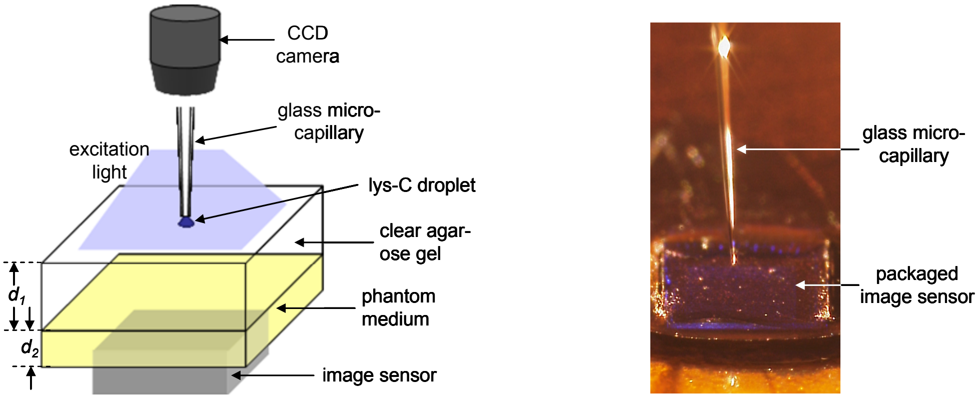

(A) (B)

Fig. 4.7 (A) In situ detection of AMC fluorescence using gel of different thicknesses. (B) Image of glass capillary positioned close to the imaging device used in the experiment. The capillary tip diameter is about 10 μm.

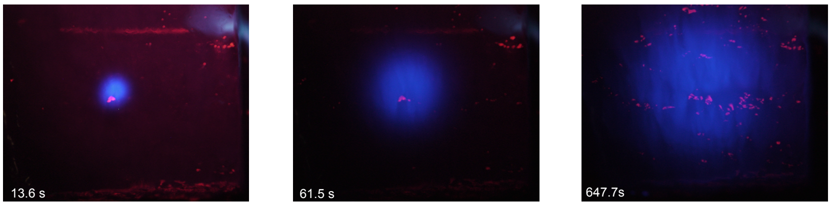

CCD Image

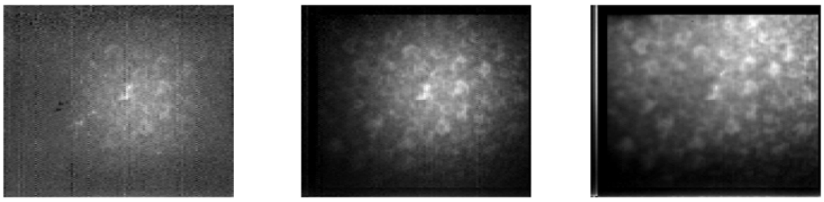

CMOS image

Fig. 4.8 Comparison between images captured by CCD and CMOS image sensor during in situ AMC detection. Images show gradual increase in spot size as the lysyl endopeptidase diffuse into the gel and reacts with the QGSK-MCA substrate to release AMC. Images for clear gel of thickness 1 mm are shown. Time (in s) after spotting of lys-C is shown on bottom left of each image.

used as a comparison for the subsequent experiments. In this experiment, 1% clear agarose gel with 0.1 mM QGSK-MCA was prepared. Because high temperature will denature the enzyme substrate, the pre-hardened agarose gel was left to stabilize at 45°C before addition of the QGSK-MCA solution. The phantom media of different thickness was placed under the clear gel. The stacked gel with a size of about 1 cm^2 was then placed onto the imaging device. The uniform excitation light from a 120 W mercury lamp filtered at 365 nm was illuminated onto the gel slice. The experimental setup is shown in Fig. 4.7. A glass capillary was used to spot a droplet of 1 mg/ml lys-C (Wako Pure Chemical Industries, Japan) onto the gel surface positioned directly on the center of the image sensor array. The capillary was positioned using a tri-axial micropositioner capable of 0.01 mm resolution.

In this experiment, the thickness of clear gel d_1 was varied from 300 to 2000 μm. The AMC fluorescence signal was measured and recorded after spotting of lys-C onto the gel surface. Immediately after spotting of lys-C, a bright spot on the gel surface was observed. This bright spot was due to the fluorescence of the released AMC. The signal from the image sensor was recorded at 5 different positions within the center of the array and the values were averaged. The frame time was set at 0.17 s. The fluorescence spot size was observed to grow with time. This was captured by the image sensor device as well as a CCD camera (VB-7010 Keyence, Japan) as shown in Fig. 4.8. The signal for different gel thickness as time progress is shown in Fig. 4.9 (A). When the signal at 200 s is plotted, the plot shows an increasing signal as the thickness increased before decreasing after a maximum value as shown in Fig. 4.9 (B).

In the next experiment, the thickness of the phantom medium d_2 was varied from 0 to 1000 μm, while keeping d_1 at 1000 μm. Because the phantom medium does not contain QGSK-MCA, this experiment gave an independent measurement for the thickness variable only. The spotting experiment was then repeated, and imaging was performed at a frame time of 1.62 s. Fig. 4.9

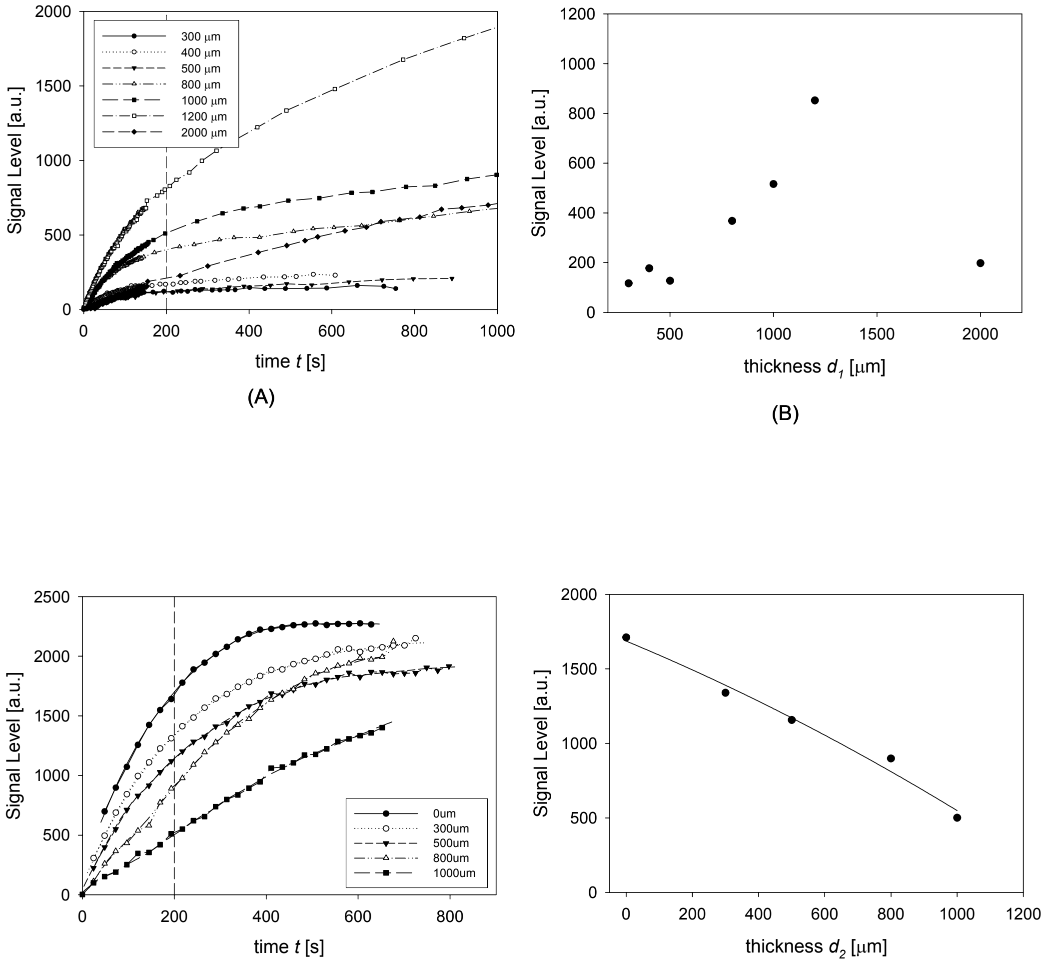

(C) (D)

Fig. 4.9 (A) Signal from image sensor as a function of time for different clear agarose gel thickness d_1, and (B) signal level for various gel thickness 200 s after lysyl endopeptidase spotting. (C) Measured signal for different phantom medium thickness d_2, and (D) signal level for various phantom thickness 200 s after lysyl endopeptidase spotting.

(C) shows the measured result as time progressed. When the signal at 200 s is plotted, the resulting plot shows a monotonous decrease in signal level as the thickness of the phantom medium increases (Fig. 4.9 (D)) with the maximum signal level at zero thickness.

ii) Lysyl Endopeptidase Concentration Dependence

Another experiment was performed to determine the minimum lys-C concentration for AMC fluorescence detection. In this experiment, a 1000 μm thick clear gel was used. Two different frame times were used to image the experiment; a faster 0.1714 s frame time and a slower 1.615 s. The increase in AMC fluorescence signal was captured over time and the signal level at 200 s is plotted in Fig. 4.10. It is observed that the detection sensitivity for the slower frame time is higher as indicated by the steeper slope. This confirms that the image sensor sensitivity can be tuned by changing the frame time. From the result, it can be concluded that a lys-C minimum concentration of 0.01 mg/ml can be detected.

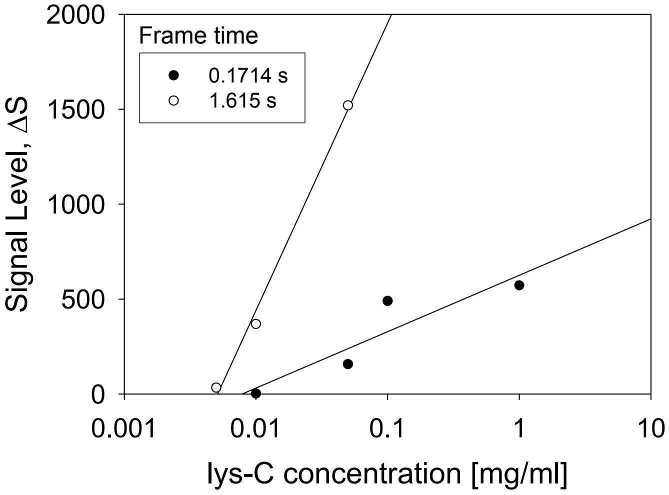

Fig. 4.10 Graph showing lys-C concentration dependence. A decrease in integration time from 0.1714 s to 1.615 s results in increase in sensor sensitivity thus enabling lower intensity fluorescence to be detected.

iii) In vivo Imaging Verification

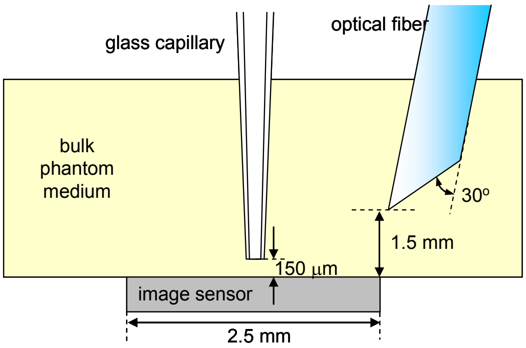

Fig. 4.11 In situ AMC fluorescence imaging experiment in bulk phantom medium demonstrating in vivo imaging.

In order to confirm that the sensor can be used for in vivo imaging, an experiment to simulate the imaging condition inside the brain was performed as shown in Fig. 4.11. In the experiment, a bulk phantom medium was prepared with 0.1 mM of QGSK-MCA in 6.4 % skim milk gel. A 500 µm diameter PMMA optical fiber was inserted into the phantom medium. The fiber edge was tapered at 30^o to the fiber axis and polished to avoid damage to the sample during insertion. Using a tri-axial micropositioner, the tip of the fiber was brought to about 1.5 mm from the edge of the image sensor. The filtered monochromatic light from the mercury lamp was coupled into the fiber. The measured output light power was about 20 µW at 365 nm. When the fiber was in position (at time t = -24 s, and distance 1.5 mm from the image sensor), the diffused light from the fiber light source could be clearly seen. The image was captured and background cancel operation was performed once. By doing so, subsequent changes in the captured image can be clearly distinguished. Next, another micropositioner was used to position the glass capillary such that the tip is about 150 µm from the device surface. This distance was determined from the fact that higher output signal was obtained by bringing the fluorescence source closer to the sensor as shown in Fig. 4.9 (D). However, there existed a minimum

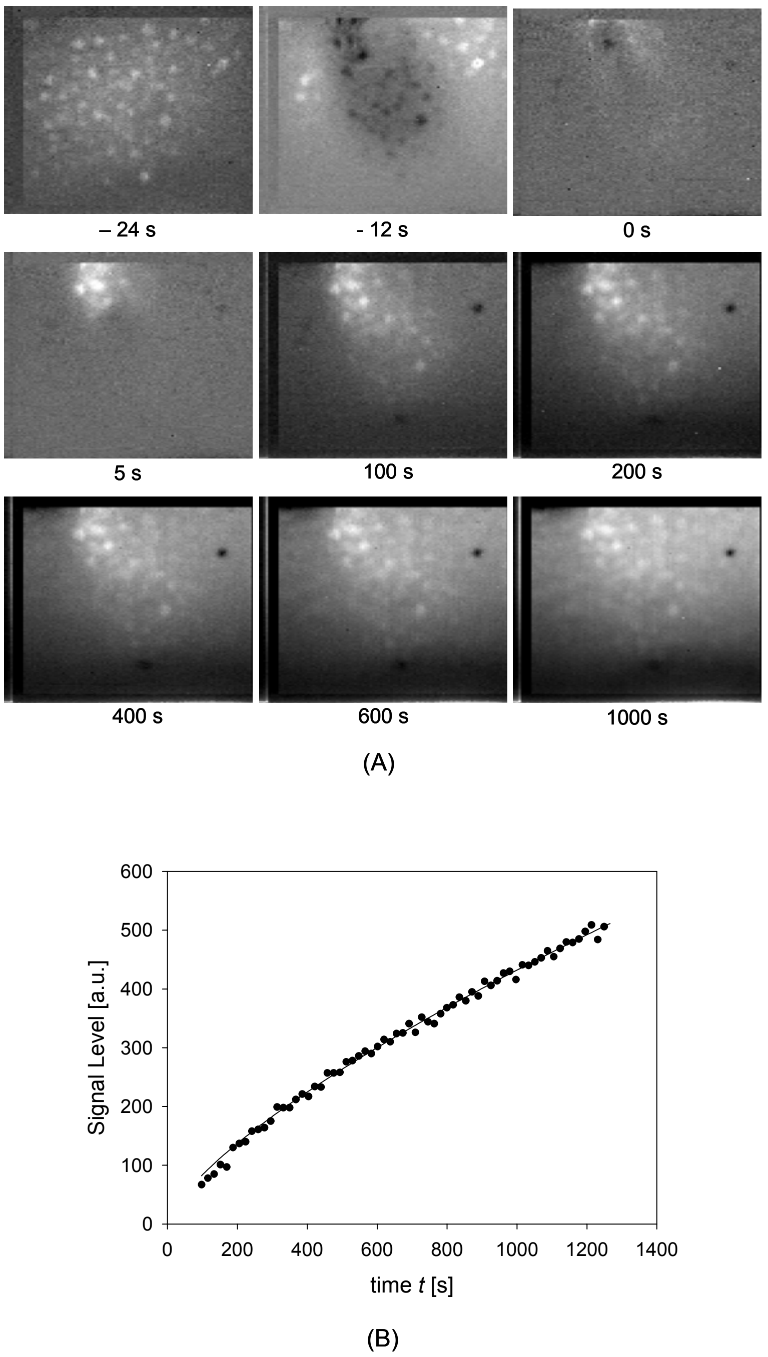

Fig. 4.12 (A) Consecutive images from in situ AMC fluorescence imaging experiment. Image at -24s shows light fiber in position and image at -12 s shows injection of lysl endopeptidase. Measurement time starts when image has stabilized with continuous background cancel and auto-balance operation, and (B) detected signal after lysyl endopeptidase injection inside the phantom medium. The signal shown is taken for the pixel with highest value.

position before the capillary tip breaches the gel surface. It was found that a distance of 150 μm gave optimum and repeatable results. To prevent image artifact due to the initial contact of the capillary with the phantom medium which releases a small amount of lys-C onto the gel surface, a small air bubble was trapped at the tip of the capillary tube after dipping into lys-C. The concentration of lys-C used was 0.1 mg/ml. Once the lys-C was injected via a microsyringe (at time $t = -12$ s), the background cancel operation was repeated, and the image and data recording started. The change in the fluorescence signal was monitored and captured continuously as time progressed. Imaging was performed at a frame time of 0.17 s. The captured images are shown in Fig. 4.12 (A). The images show an increase in the recorded signal as the lys-C reacted with the substrate and AMC was released in the same manner as observed for the gel slice experiment (Fig. 4.12 (B)). This experiment vefified that in vivo fluorescence imaging using the imaging device is possible.

4.4 Animal Imaging Protocol

Experiments involving animals were performed in accordance to the guidelines laid down by the Nara Institute of Science and Technology which is based on the procedures approved by the Institutional Ethical Committee for Experimental Animals.

4.4.1 In vitro Imaging

A lipophilic fluorescent dye, DiA, was used in this experiment. Once applied to cells, the dyes diffused laterally within the plasma membrane, resulting in staining of the entire neuronal cell. DiA crystals with a grain size of diameter < 0.5 mm were inserted into both the left and right hippocampal regions using a glass micropipette. After the procedure, the skull was capped

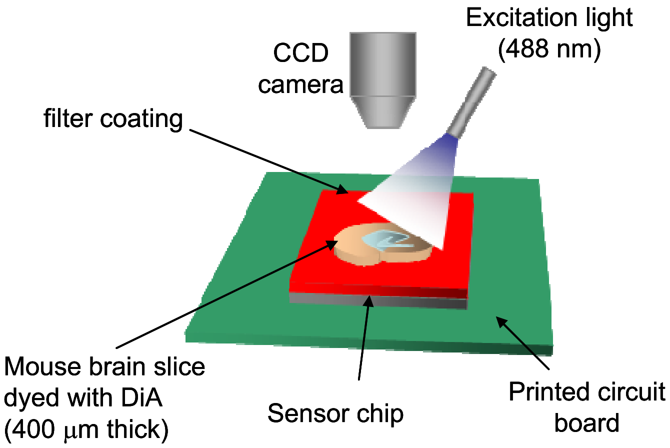

Fig. 4.13 Experimental setup for in vitro brain slice imaging experiment.

and the animal was returned to its cage and kept alive for 4 days prior to the imaging experiment. This was to allow sufficient time for transport of the dye into the neuronal membranes. The condition of the mouse was monitored for abnormal activities. After 4 days, the animal was decapitated under urethane anesthesia. The same procedure as described in §4.3.1 was used to slice the brain. The slice of interest from the caudal diencephalon region was selected for imaging. The prepared brain slice was then placed on the surface of the image sensor as shown in Fig. 4.13. Excitation light passing through a 488 nm filter from a mercury lamp was used to uniformly illuminate the sample. The image sensor was operated at 15 fps and lighting conditions were optimized. The slice was carefully positioned, allowing part of the CA1 and dentate gyrus (DG) areas of the hippocampus to fit within the image sensor array. The light captured by the image sensor originates from the fluorescence emitted from the slice. As a comparison, the image from the upside slice was captured using a CCD camera.

4.4.2 In vivo Imaging

Two separate in vivo imaging experiments were performed. The first experiment involves

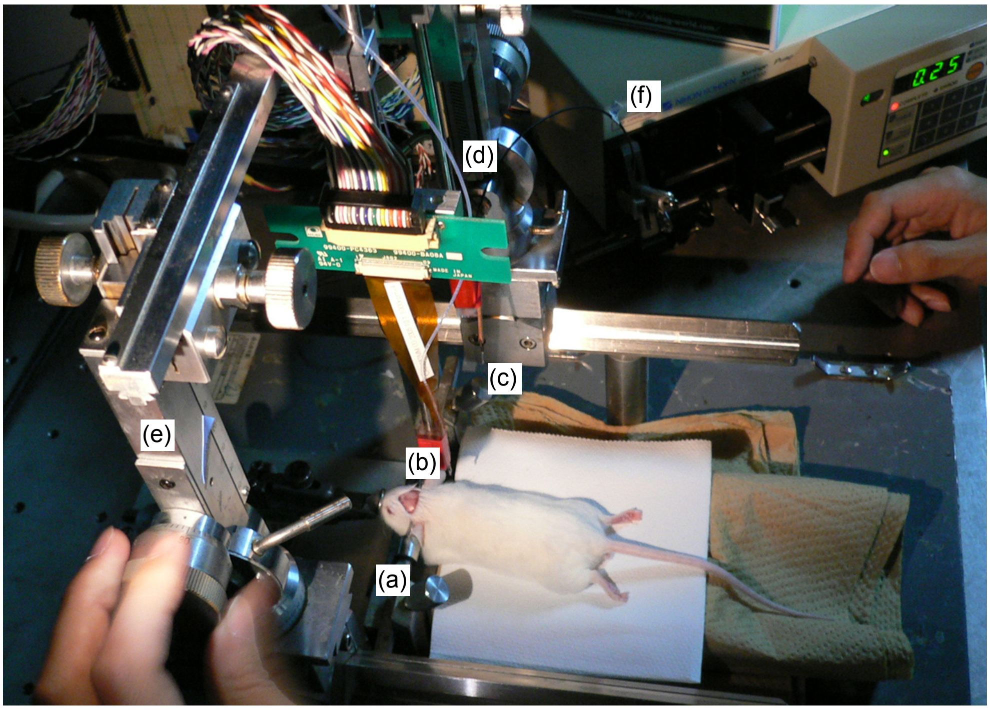

Fig. 4.14 Photograph of apparatus for in vivo imaging experiment showing; (a) stereotaxic head holder, (b) image sensor device, (c) optical fiber, (d) teflon tube, (e) 5 axis micropositioner, (f) syringe pump.

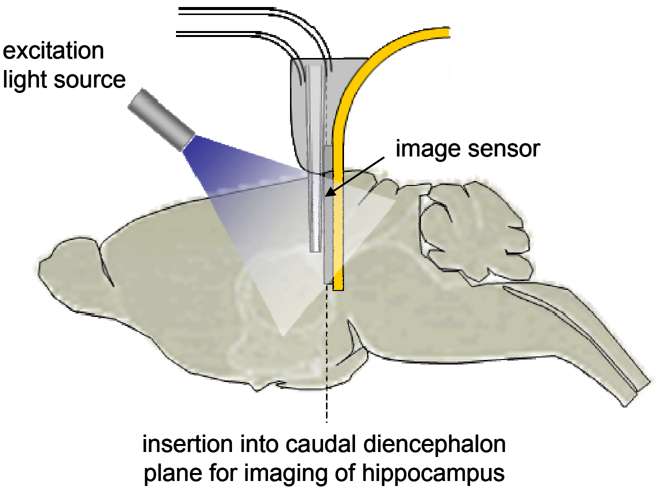

Fig. 4.15 Diagram showing cross sectional view of mouse brain with fiber and image device in position (drawing not to scale). The device was inserted along the caudal diencephalon plane for imaging of the hippocampus.

imaging of the fluorescence dyed-brain 4 days after insertion of the DiA crystals. This experiment is used to verify capability of the imaging device for fluorescence imaging inside the brain. In the second experiment, I attempted fluorometric measurement of the physiological changes in the brain due to externally induced serine protease activity. This demonstration serves to prove the capability of the image sensor for in vivo functional studies of the brain. Fig. 4.13 shows the experimental setup for in vivo imaging.

For the first experiment, a packaged chip incorporating the red filter (see Chapter 3) was used. Four days after the staining procedure, the animal was anesthetized and positioned on the stereotaxic head-holder. The skull of mouse was exposed and cleaned, and a rectangular cranial window (3 mm × 2 mm) was bored on both the left and right sides of the skull. With the center of the chip positioned at 2.46 mm posterior and 2.0 mm lateral to bregma, it was then slowly inserted into the brain until the entire image sensor array reached the hippocampus as shown in Fig. 4.15. The exposed brain was externally illuminated with excitation light from a

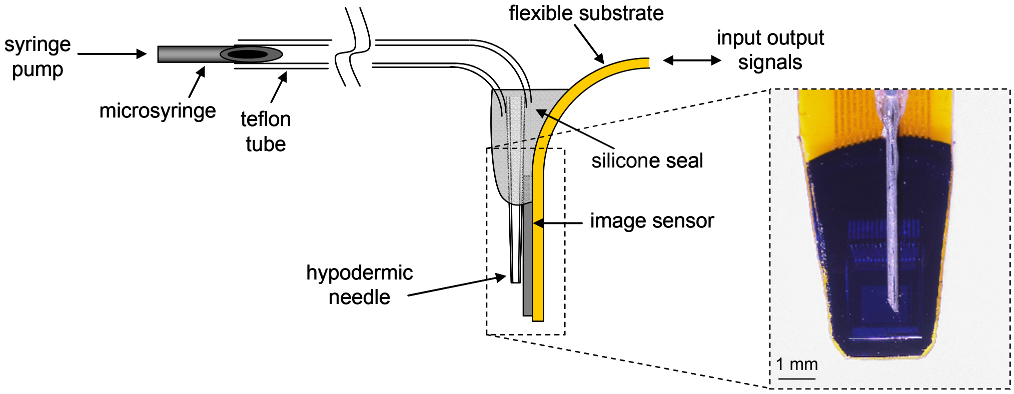

Fig. 4.16 Schematic showing cross sectional view of the device with electrical and fluidic connections. Inset shows top view of the hypodermic needle attached to the fully packaged CMOS image sensor.

120 W mercury lamp, filtered with a 470 nm filter. Due to the weak light conditions inside the brain, imaging frame rate was reduced to 5 fps to increase sensitivity. The captured images were constantly auto-balanced to stretch the contrast as the lighting condition varied appreciably during the experiment. After the experiment, the brain was removed into ice-cold 0.1 M phosphate-buffered saline (PBS) and coronally sliced to about 1 mm thickness. The region facing the image sensor was examined under a fluorescent microscope.

For the second experiment, an additional syringe was required to inject a fluorogenic substrate close to the surface of the imaging array. A hypodermic needle (27G×3/4 Terumo, Tokyo) was used for this purpose. It was connected to a microsyringe (1001RN Hamilton, USA) via a Teflon tube. A syringe pump (CFV-2100 Nihon Kohden, Japan) was used to control the injection flowrate. Fig. 4.16 shows the fully fabricated device when used for the second in vivo imaging experiment. A mercury lamp (VB-L10 Keyence, Japan) was used as the light source. A bandpass filter (OP42311 Keyence, Japan) was used to selectively transmit monochromatic light at 367 nm with a 28 nm bandwidth, which was then coupled into a 500 μm diameter PMMA

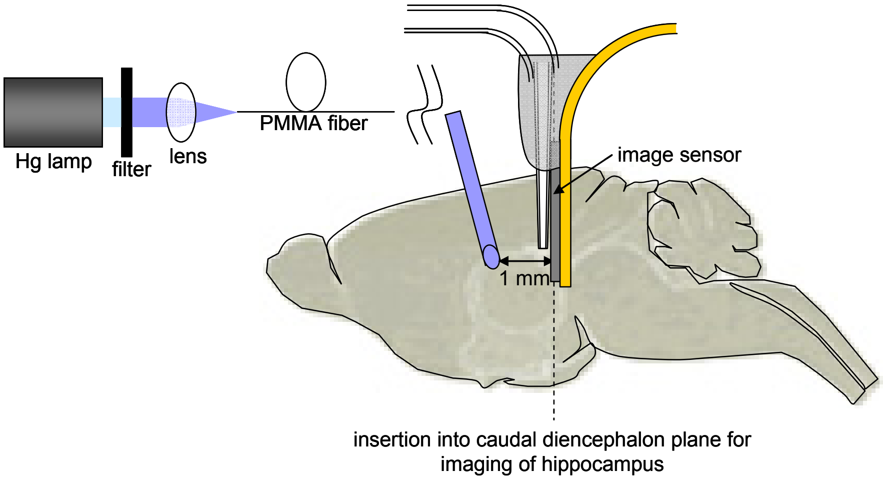

Fig. 4.17 Cross sectional schematic showing position of fiber and image device in vivo (drawing not to scale). The device is inserted along the caudal diencephalon plane for imaging of the hippocampus.

jacketed fiber (SK-20 Mitsubishi Rayon, Japan). The fiber was used to guide the excitation light into the mouse brain. It was found that the position of the fiber tip at a distance of about 1 mm from the sensor surface provides the optimum lighting condition. Due to scattering of light inside the brain, a fairly uniform illumination was obtained. The fiber tip was tapered at 30^o from the fiber axis and polished for maximum delivery of light as well as to ease insertion into the brain. The measured output power was approximately 20 µW at a wavelength of 365 nm. In this experiment, the synthetic substrates VPR-MCA and PGR-MCA (3093-v and 3145-v respectively Peptide Institute, Japan) were used. A 1:1 mixture of 1 mM VPR-MCA and 1 mM PGR-MCA in 50 mM Tris buffer (pH 8.0) was prepared. This substrate solution was used to maximize the available fluorescence signal in the brain. The substrate was pumped at a rate of 0.08 µl/min for one hour. KA was injected into intraperitoneally and transported by blood stream to the brain. Fifteen minutes after substrate pump started, 800 µl (20 mg/kg) of KA at 1 mg/ml concentration was injected. Serine protease activity was measured continuously for 5 hours after the KA injection. At the end of the experiment, the brain was extracted, sliced and observed using a fluorescence microscope. During the initial stage where the imaging device was inserted into the brain, the image sensor was operated at a high frame rate of 10.8 fps. This enabled visual feedback at near video rate. Once the device was fully inserted into the hippocampal region, illumination was provided by excitation light from the fiber only. The frame rate was then dropped to a slower 3.85 fps to increase measurement sensitivity. Another experiment was performed as the control experiment where only the substrate is injected and changes in fluorescence signal measured. For detection of AMC fluorescence, the imaging device was coated with the blue filter. Fig. 4.17 shows the relative position of the fiber to the image sensor inside the mouse brain.

4.5 Imaging and Measurement Results

4.5.1 Morphological Study from In vitro Imaging

Fig. 4.18 (A) shows the captured static images. From the image captured by the image sensor, the morphological features of the hippocampus can be observed. There is a bright spot in the center region caused by uneven thickness of the slice in that area resulting in high pixel values. A plot of the pixel values along the same section for the CCD image and the image captured by the CMOS image sensor is shown in Fig. 4.18 (B). From this plot, a clear correlation between the two images can be seen. The polymorphic layer (po) area which lies closest to the site of the embedded DiA crystal, thus most heavily stained, shows the highest pixel value. Next to it, a drop in the pixel value indicates the granule cell layer (sg). Further away, the molecular layer (mo) and stratum lacunosum moleculare (slm) show a corresponding

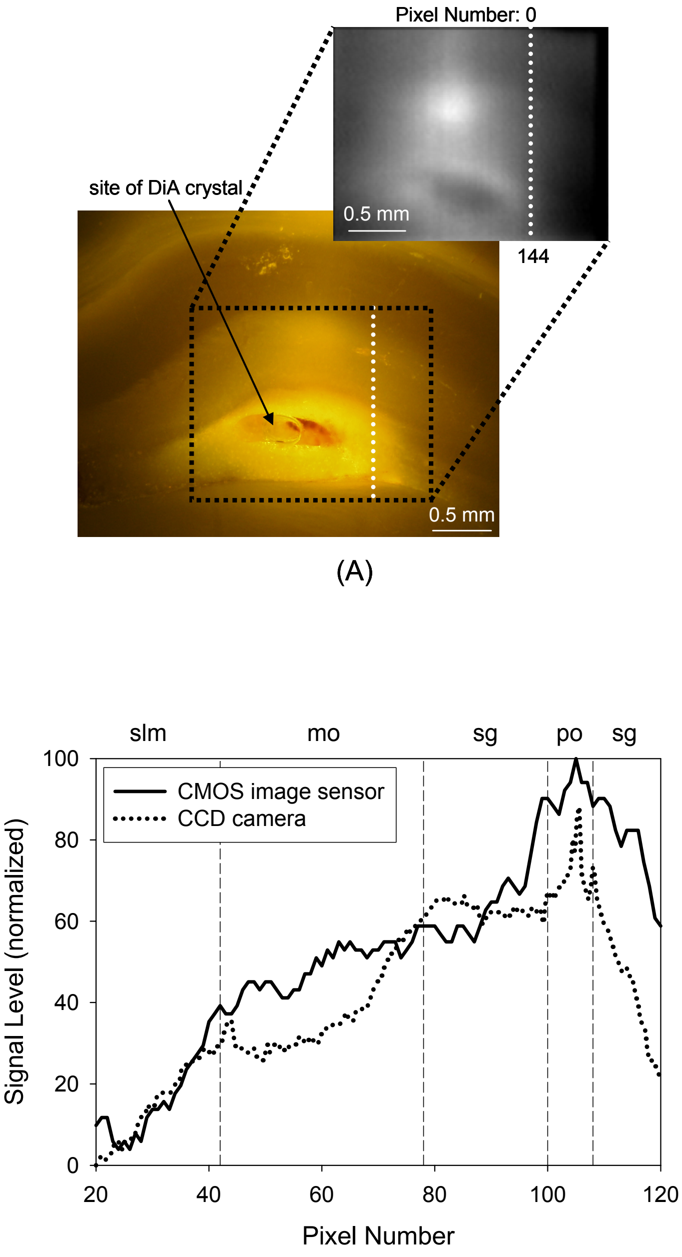

(A)

(B)

Fig. 4.18 (A) Brain slice image captured by CCD camera and image sensor (inset). (B) Pixel value plot of region of interest (dotted white line) showing correlation between the captured images. The different hippocampal morphologies can be clearly distinguished (stratum lacunosum moleculare, slm, molecular layer, mo, granule cell layer, sg, polymorphic layer, po).

reduction in pixel values. The images taken by the CCD camera and the image sensor are not identical due to the fact that opposite sides of the slice are captured. For the image sensor, absence of focusing optics causes overlapping of fluorescence images onto the photosensing array. This inadvertently reduces the image quality. Furthermore, diffused and scattered fluorescence photons further away from the image sensor into the tissue contribute in a non-uniform manner to the background level which causes image degradation. The image quality, however, can be improved preparing a thinner specimen.

4.5.2 In vivo Structural Imaging

In the first in vivo imaging experiment, the imaging device was slowly inserted into the dyed brain four days after insertion of the DiA-dye crystal. Fig. 4.19 shows successive images captured during the insertion of the CMOS image sensor into the brain. Initially, as the image sensor was inserted into the brain, the interface between the brain surface and air could clearly be seen. As the image sensor was inserted further, darker shades of the unstained region of the brain could be seen to move relative to the image sensor. When fully inserted, fluorescence emission from the stained region in the hippocampus was captured. The image of the hippocampus structure shows the darker molecular layer which is relatively unstained compared to the heavily stained CA1 region. A faint outline of the hippocampal fissure is also observed. At the end of the experiment, the brain was extracted and the slice facing the image sensor was observed under a microscope. It was confirmed that, injury to the brain during the imaging experiment was limited to the cortical area only. Also, throughout the experiment, although the animal was breathing normally and no artifacts from heartbeats were observed. This is one advantage of on-chip imaging as the sensor is in contact with the surface of the object resulting in no relative motion.

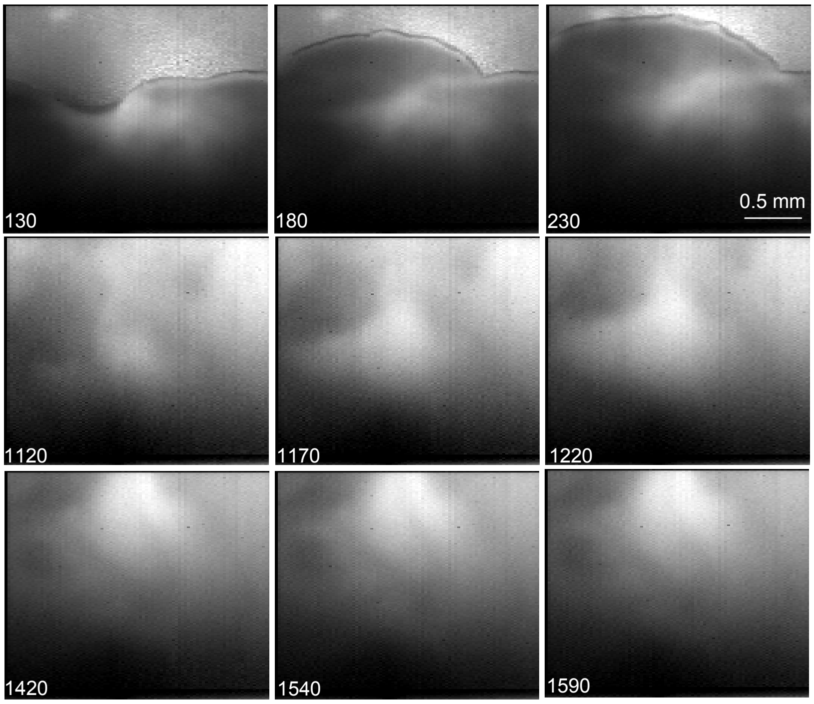

Fig. 4.19 Successive real-time images during in vivo imaging experiment. (frame numbers are shown at bottom left corner). The top 3 images (frames: 130, 180, 230) show the start of experiment where the sensor chip start to penetrate the brain surface. The brain-air interface is clearly observed. The middle 3 images (frames: 1120, 1170, 1220) show insertion in progress. Movement through the cortex is verified by darker shades of unstained region of the brain. The bottom 3 images (frames: 1420, 1540, 1590) are the final images after the sensor chip has stopped at the hippocampus.

Although in vitro imaging of the brain slice easily showed the stained structure of the hippocampus, imaging inside the brain was somewhat more complicated. This is because fluorescence from the entire bulk stained region in front of the sensor is superimposed due to the external illumination light in which the entire brain area is bathed. As shown in Chapter 3, imaging inside the brain tissue phantom, light scattering does not reduce the image resolution considerably, if the imaging depth is kept below 500 µm. Hence by locating a light fiber close to the fluorescence source at about 1 mm, the diffuse excitation from the fiber can introduce uniform illumination and reduce image blurring. Moreover, once the region of interest is specified, the light falling onto a single pixel can be measured with great temporal resolution. This will enable the localized area to be further studied.

4.5.3 In vivo Functional Imaging and Biofluorometric Measurement

In the second experiment, imaging and measurement of the AMC fluorescence were performed in real time. The images captured during each event from the start as the imaging device was inserted into the brain, to the induction of serine protease by KA which was detected by the fluorogenic substrate are shown in Fig. 4.20 (A). Initially the brain-air interface can be discerned as illumination light was provided by a halogen lamp externally. As the sensor was further inserted into the brain, the shadow of the needle can be seen. Once the device was fully inserted into the hippocampal region, illumination was provided by the excitation light from the fiber only. Five locations near the outlet of the needle were selected and plotted. I observed similar trend from all of the five locations. A plot of the signal level from a single location is shown in Fig. 4.20 (B). As can be seen from the plot, an abrupt increase in the signal is observed at 1 hr 28 min after the KA injection. Subsequently, the recorded signal showed a sustained and gradual increase above the initial increase throughout the entire experimental recording period

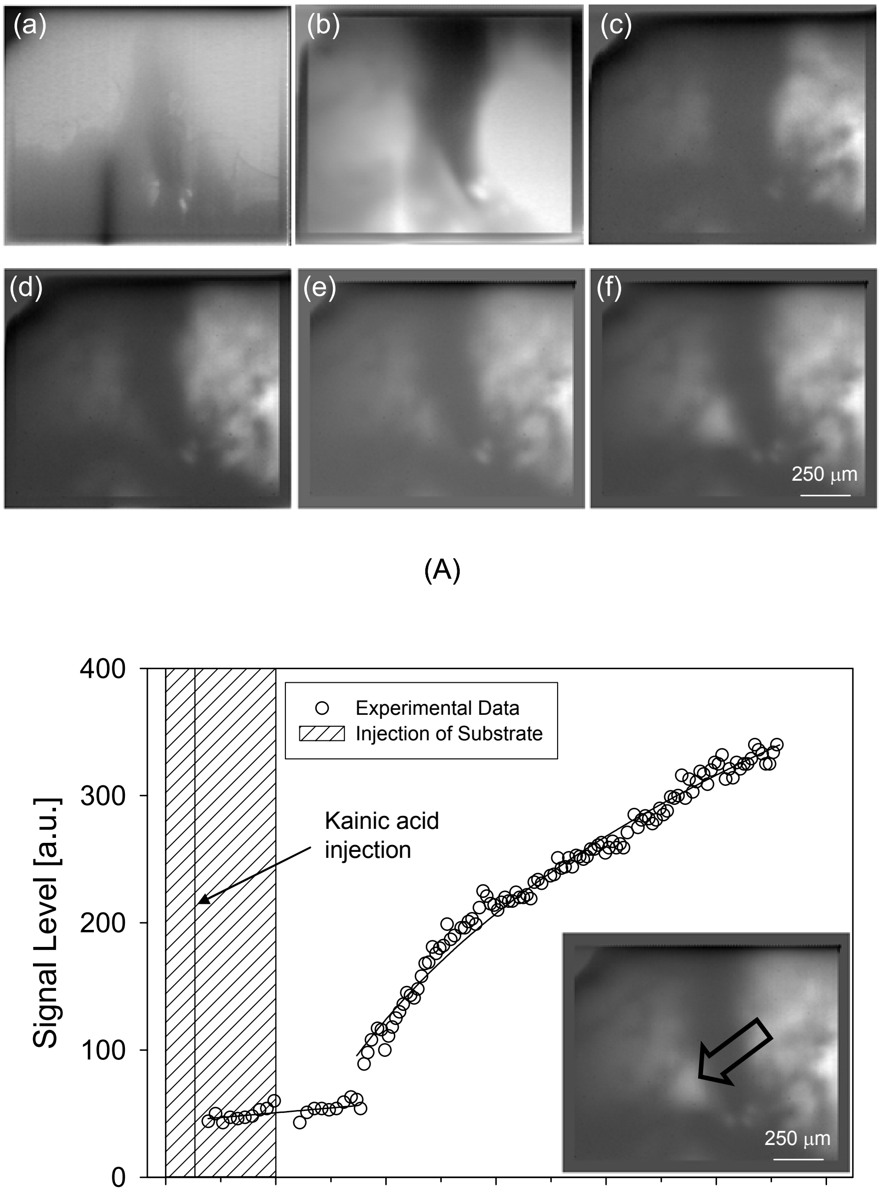

(A)

(B)

Fig. 4.20 (A) Captured images as image sensor is inserted into the brain and imaging of released AMC from the fluorophore substrate. The dark area is the needle shadow. (a) insertion of sensor into brain and imaged under visible light. (b) Sensor fully inserted at the hippocampus. (c) pumping of substrate start, illumination from fiber light. (d) injection of kainic acid after 15 min. (e) substrate pumping stop after 1 hr. (f) image captured after 3 hr 25 min. (B) Measured fluorescence signal from the pixel with location shown with arrow at inset image.

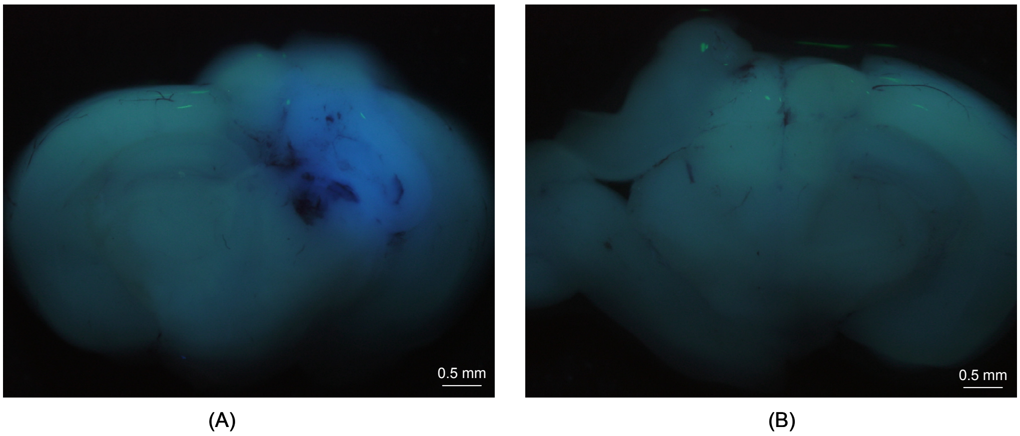

(A) (B)

Fig. 4.21 Image of brain slices after experiment. (A) slice in front of sensor, (B) slice behind sensor. Note that AMC fluorescence is localized at the hippocampus where the substrate is injected.

which lasted slightly longer than 5 hours. This result indicates that serine protease is activated by the KA injection. Furthermore, the brain slice, at the end of the experiment, indicated positive AMC fluorescence which was localized at the hippocampus only where the substrate was injected as shown in Fig. 4.21. This served as a visual confirmation for the serine protease activity recorded in vivo. The control experiment performed to verify signal stability during the substrate injection alone registered about half of the observed signal increase. Also, the control experiment performed to verify changes in the recorded signal during substrate injection alone registered only a slight increase in the signal which remained constant throughout the entire experiment. This can be accounted for by considering the emission from the substrate. From this result I was able to observe in real time, the time scale of KA induced serine protease activity as it progressed from its onset.

4.6 Discussion

4.6.1 Brain Tissue Phantom

The phantom medium developed enabled close resemblance to the brain tissue in terms of two properties; mechanical and optical. Although an exact replica of the brain is difficult, sufficient mechanical rigidity can be obtained by preparing the medium with the appropriate gel content. I tested several preparations and found that a 1% agarose gel when hardened, formed a semi-solid state that was ideal for our experiment. This was demonstrated by infusion and diffusion of lys-C in the experiment that will be described below. The same conclusion has been reported elsewhere [16]. Apart from ease of handling and storage, the preparation is very repeatable and can be made highly homogeneous. In the transmittance measurement, thin sample slices were used due to the relatively weak light from the monochromator. In order to increase the signal-to-noise ratio and compensate for the weaker light, a photodiode with a large viewing angle of about 0.01 sr was used. The disadvantage of this is, a proportionally large amount scattered light was also collected. This overestimates the collected power by the photodiode which results in a higher than expected transmittance value [17]. However, because the same optical setup was used to compare the brain and phantom slices, the reliability of the method is assured. The increase in transmittance as wavelength increases confirms the larger penetration depth of longer wavelengths in tissue as predicted and reported elsewhere [18-20]. In developing the brain phantom, many materials and scattering medium (including TiO_2 etc) were tried and I found that that combination of skim milk in agarose gel to produce the most reliable and repeatable result. Because transmittance measurement over the spectrum of interest is measured for the phantom brain, and compared to the actual brain slice which contained traces of blood inside capillaries, I believe that result is sufficiently justified. Further work which includes blood inside the scattering medium would be conducted to generate a database whereby a better brain phantom can be developed.

4.6.2 In vivo Verification Experiment

The in situ AMC detection experiments showed that lys-C diffused into the gel and reacted strongly with the QGSK-MCA substrate even without elevating the surrounding temperature. Also, the amount of fluorescence detected was directly proportional to the concentration of AMC released. During the experiment, both lateral and vertical diffusion of the lys-C into the gel were observed. The experiment involving QGSK-MCA in clear agarose gel shows that the reaction is highly dependent on gel thickness. As the thickness increased, the amount of QGSK-MCA substrate also increased. Thus a larger amount of AMC was released when treated with lys-C. In this stage, the signal is substrate limited. However, the fluorescence signal starts to fall after a maximum value. This can be explained by the fact that as the gel thickness approaches a certain maximum value, the effect of optical attenuation of the fluorescence signal reaching the image sensor can no longer be ignored. The signal starts to fall as the thickness is increased further. In this region, the signal is thickness limited. In the experiment involving the phantom medium, the signal is completely independent of the amount of substrate available. Here, the effect of signal attenuation due to light scattering and absorption plays the major role in determining the amount of fluorescence signal measured. As expected, as the fluorescence source is nearer to the image sensor, a stronger signal is recorded. Hence, in the experiment to verify in vivo fluorescence imaging, the point of release is placed as close as possible to the image sensor. In the present case, the tip of the glass capillary was positioned 150 μm from the image sensor. Although these experiments were performed to verify in vivo imaging conditions, the result which shows that there exists a maximum fluorescence signal in the clear gel is interesting enough to warrant further investigation. This would prove useful in work related to assaying a high density array of chemicals related to pharmaceutical and biological research.

4.6.3 In vivo Imaging Functional Imaging

Throughout the entire in vivo functional imaging experiment, the background signal was recorded at six instances with intervals of about 30 minutes. It was found that fluctuation of the background signal was less than 1% of the initial signal. This confirms that there is minimum signal drift during the experiment and that the signal drift does not affect the measured result in any significant way. Also, physical movement of the light source inside the brain was measured to determine its effect on the measured signal. At 1 mm from the sensor, a 1 μm movement towards and away from the sensor resultant in a change in signal level of about 0.06 %. This is far less than the changes recorded during the in vivo imaging experiment, which confirms that the signal measured is not due to relative motion between the sensor and the light source. Also, throughout the experiment, although the animal was breathing normally, no rhythmic artifact from heartbeats was observed. This was verified from the measurement result in Fig. 4.21. This shows that, in principle the device can be used for monitoring a freely moving animal carrying such a device on its body. Also, the mouse body temperature was monitored closely throughout the entire experimental period which lasted about 6 hours. It is believed that a recording period that last for days is possible when the body temperature is maintained.

The brain slices after the imaging experiment showed that there is no blood coagulation inside the brain. Also, superficial injury is observed to be limited to the cortical area only. This suggests that the invasive operation inflicts minimal injury to the brain. Although, the cellular layer directly in contact with the image sensor may have been insulted, beyond this layer, the neuronal cells remained unaffected. This is confirmed by the increase in fluorescence signal during in vivo imaging where the unaffected cells continue to function and respond normally.

The results of this experiment have several implications. First, I have demonstrated the capability of the imaging system for detecting brain activity in real time. I believe that this is the first report of simultaneous high resolution imaging and fluorometric measurement. Second, I have independently verified findings which reported the increase in tPA expression due to KA which was achieved by in vitro methods [21, 22]. It was reported that tPA activity gradually increases starting from 4 hours and up to 8 hours after KA injection into the brain. Our result not only confirms these reported results but is able to provide high temporal resolution data as well. Third, by using the same model reaction for detection of specific serine protease, the locus distribution and function of these protease species in the brain can be further studied. In the experiment, although a relatively high concentration of substrate and KA was used, I demonstrated that it is possible to detect serine protease activity in vivo using the imaging device. Being a prototype for demonstrating in vivo imaging, further improvement in device sensitivity can be expected.

The result of this experiment has several implications. First, I have demonstrated the capability of the imaging system for detecting brain activity in real time. I believe that this is the first report of simultaneous high resolution imaging and fluorometric measurement. Second, I have independently verified findings which reported the increase in tPA expression due to KA which was achieved by in vitro methods [21, 22]. It was reported that amount of tPA activity gradually increases starting from 4 hours and up to 8 hours after KA injection into the brain. Our result not only confirms these reported results but is able to provide high temporal resolution data as well. Third, by using the same model reaction for detection of specific serine protease, the locus distribution and function of these protease species in the brain can be further studied. In the experiment, although a relatively high concentration of substrate and KA was used, I demonstrated that it is possible to detect serine protease activity in vivo using the

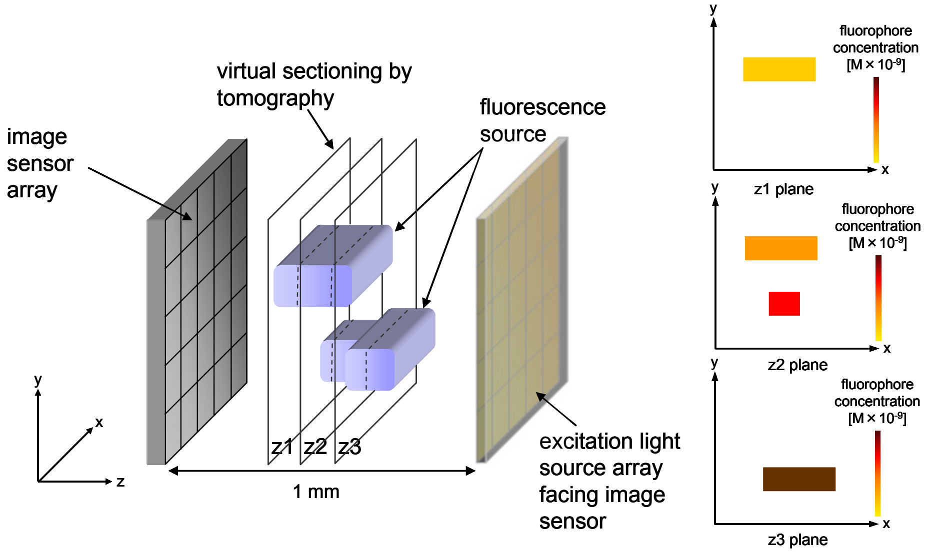

Fig. 4.22 Proposed schematic for implementing three dimensional fluorescence imaging.

imaging device. Being a prototype for demonstrating in vivo imaging, further improvement in device sensitivity can be expected.

One aspect that requires some thought is regarding the extendibility of the device for use in three dimensional imaging. Although the current setup only enable two dimensional imaging, depth information can be obtained by employing a computation technique borrowed from tomography imaging. In order to achieve that, an arrayed illumination light source would be required. A schematic for implementing three dimensional fluorescence imaging is shown in Fig. 4.22. Using this method, virtual sectioning of the fluorescence imaging can be performed. The images can then be combined to form a three dimensional image.

Although invasive in nature, this imaging method offers advantages which make it attractive for many bioimaging applications. As mentioned in §4.1, it is capable of arbitrary imaging depth. This overcomes the photon penetration depth limitation found in conventional microscopic techniques. Also, the capability of continuous imaging in vivo represents a great improvement over existing in vitro techniques. When combined with fluorescence techniques,

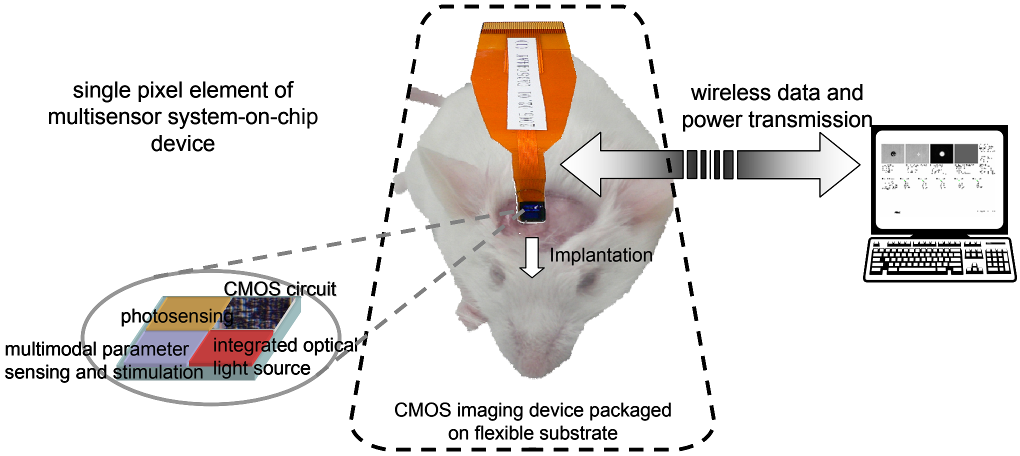

Fig. 4.23 Schematic of proposed of wireless multimodal CMOS imaging system for imaging of freely moving animal. Scope of this work is shown in the dotted line.

high specificity and high resolution imaging is possible. This is in contrast to in vivo imaging techniques such as MRI and PET which has limitations in terms of resolution and specificity. Finally, the imaging device has potential for multimodal parameter imaging as described in Chapter 2.

Ultimately, this work is expected to lead to a promising new tool where imaging and measurement can be made using a device where power and data are transferred wirelessly as shown in Fig. 4.23. It will consist of a single system-on-chip device that implements multimodal parameter sensing with integrated light source and possibility of electrical stimulation. This will lend itself greatly by complementing existing methods for studying freely moving animals. In the future, when the device is operated wirelessly, chronic monitoring for periods lasting up to several days may not be impossible. Development of on-chip illumination may then be the limiting factor for the device design.

4.7 Summary

I have demonstrated the capability of a CMOS imaging device for both in vitro and in vivo imaging of the mouse brain. This device has the ability to perform on-chip imaging of brain slices and imaging inside the intact brain. In vitro morphological study shows that the image captured by the imaging device is comparable to images from conventional fluorescence microscopes. When extended to in vivo imaging, the device confirms that imaging inside the brain is possible. Furthermore, quantitative measurement of the fluorescence signals enables highly specific functional studies of the brain.

References

[1] L. J. Blum, P. R. Coulet, “Bio-, chemi-, and electrochemiluminescence for fiber-optic biosensors,” in *Biosensors*, 2nd ed., J. M. Cooper, A. E. G. Cass, ed.s Oxford: Oxford University Press, 2003, pp. 97-108.

[2] D. M. Fraser, “An introduction to in vivo biosensing,” D. M. Fraser, *Biosensors in the body: continuous in vivo monitoring*. West Sussex: Wiley, 1997, pp. 1-42.

[3] S. Finger, *Origins of Neuroscience: A History of Explorations into Brain Function*. Oxford: Oxford University Press, 1994, pp. 3-15.

[4] J. C. Massiotta, “Time and Space,” Brain Mapping: the Methods, 2nd ed., A. W. Toga, J. C. Mazziotta ed.s, San Diego: Academic Press, 2002, pp. 33-45.

[5] F. Helmchen, M. S. Fee, D. W. Tank, W. Denk, “A miniature head-mounted neurotechnique two-photon microscope: high resolution brain imaging in freely moving animals,” *Neuron*, vol. 31, pp. 903-12, Sep. 2001.

[6] A. Mizrahi, J. C. Crowley, E. Shtoyerman, L. C. Katz, “High-resolution in vivo imaging of hippocampal dendrites and spines,” *J. Neurosci.*, vol. 24, pp. 3147-3151, Feb. 2004.

[7] V. Ntziachristos, C.-H. Tung, C. Bremer, Ralph Weissleder, “Fluorescence molecular tomography resolves protease activity in vivo,” *Nature Medicine*, vol. 8, no. 7, pp. 757-760, July 2002.

[8] S. V. Patwardhan, S. R. Bloch, S. Achilefu, J. P. Culver, “Time-dependent whole-body fluorescence tomography of probe bio-distributions in mice,” *Opt. Exp.*, vol. 13, pp. 2564-2577, Mar. 2005.

[9] M. D. Davis, J. J. Schmidt, “In vivo spectrometric calcium flux recordings of intrinsic caudate-putamen cells and transplanted IMR-32 neuroblastoma cells using miniature fiber optrodes in anesthetized and awake rats and monkeys,” *J. Neurosci. Methods*, vol. 99 , pp. 9-23, Mar. 2000.

[10] A. D Mehta, J. C. Jung, B. A. Flusberg, M. J. Schnitzer, “Fiber optic in vivo imaging in the mammalian nervous system,” *Curr. Opin. Neurobiol.*, vol. 14, pp.617–628, Sep. 2004.

[11] R. P. Haughland, *Handbook of fluorescent probes and research products*, 9th ed., Eugene:

Molecular Probes, 2002, pp. 401-439.

[12] Z. Qian, M. E. Gilbert, M. A. Colicos, E. R. Kandel, D. Kuhl, "Tissue-plasminogen activator is induced as an immediate−early gene during seizure, kindling and long-term potentiation," *Nature*, vol. 361, pp. 453-457, Feb. 1993.

[13] S. E. Tsirka, A. Gualandris, D. G. Amaral, S. Strickland, "Excitotoxin-induced neuronal degeneration and seizure are mediated by tissue plasminogen activator," *Nature*, vol. 377, pp. 340-344, Sep. 1995.

[14] Z. L. Chen, S. Yoshida, K. Kato, Y. Momota, J. Suzuki, T. Tanaka, J. Ito, H. Nishino, S. Aimoto, H. Kiyama, S. Shiosaka, "Expression and activity-dependent changes of a novel limbic-serine protease gene in the hippocampus," *J. Neurosci.*, vol. 15, pp. 5088-5097, Jul. 1995.

[15]Y. Momota, S. Yoshida, J. Ito, M. Shibata, K. Kato, K. Sakurai, K. Matsumoto, S. Shiosaka, "Blockade of neuropsin, a serine protease, ameliorates kindling epilepsy," *Eur. J. Neurosci.*, vol. 10, pp. 760-764, Sep. 1998.

[16] Z. J. Chen, G. T. Gillies, W. C. Broaddus, S. S. Prabhu, H. Fillmore, R. M. Mitchell, F. D. Corwin, P. P. Fatouros, "A realistic brain tissue phantom for intraparenchymal infusion studies," *J. Neurosurg*., vol. 101, pp. 314-322, Aug. 2004.

[17] A. Taddeucci, F. Martelli, M. Barilli, M. Ferrari, G. Zaccanti, "Optical properties of brain tissue," *J. Biomed. Opt*., vol. 1, pp. 117-123, Jan. 1996.

[18] L. O. Svaasand, R. Ellingsen, "Optical properties of human brain," *Photochem. Photobiol*., vol. 38 pp. 293-299, Mar. 1983.

[19] F. Bevilacqua, D. Piguet, P. Marquet, J. D. Gross, B. J. Tromberg, C. Depeursinge, "In vivo local determination of tissue optical properties: application to human brain," *Appl. Opt*., vol. 38, pp. 4939-4950, Aug. 1999.

[20] W.-F. Cheong, S. A. Prahl, A. J. Welch, "A review of the optical properties of biological tissues," *IEEE J. Quantum Electron*., vol. 26, pp. 2166-2185, Dec. 1990.

[21] N. Nagai, T. Urano, A. Endo, H. Takahashi, Y. Takada, A. Takada, "Neuronal degeneration and a decrease in laminin-like immunoreactivity is associated with elevated tissue-type plasminogen activator in the rat hippocampus after kainic acid injection," *Neurosci. Res*., vol. 33, pp. 147-154, Dec. 1999.

[22] Y. Matsuoka, Y. Kitamura, T. Taniguchi, "Induction of plasminogen in rat hippocampal

pyramidal neurons by kainic acid," *Neurosci. Lett.*, vol. 252, pp. 119-122, Jul. 1998.

Chapter 5

Electrical Stimulation and Effect of Mechanical Strain

A dedicated CMOS sensor chip has been developed using standard CMOS technology in order to study its capability for electrical stimulation of biological tissues. Image sensing and electrical stimulus are integrated onto the same chip thus forming a 16 × 16 pixel imaging and stimulus electrode array. The imaging circuit is based on the pulse frequency modulation photosensing circuit. An immediate application for the device is electrical stimulation of the degenerated retinal cells. Using the device, biphasic current stimulus pulses at above threshold levels of the human retina (500 μA) at varying frame rates (4 Hz to 8 kHz) is demonstrated. The generation of electrical current stimulation with flexible and programmable waveform is useful not only for retinal stimulation but also for stimulation of other biological tissues like the brain. Furthermore, in order to implement the image sensor as a retinal prosthesis inside the human eye, the sensor chip needs to be bent to the eyeball curvature. The effect of mechanical strain on simple semiconductor transistor devices and the more complicated pulse frequency modulation-based photosensor were studied. Based on the results of this study, we explained the behavior of the photosensor under compressive and tensile bending. It is found that the maximum frequency variation of the photosensor to bending is about +4 % when extrapolated to the curvature of the human eye. Due to the generality of this study, the same conclusion can be extended to other larger scale integrated circuits subjected to mechanical strain.

Keywords: CMOS, photosensor, image sensor, pulse frequency modulation, subretinal implant, retinal prosthesis, bending effect, strain

5.1 Introduction

In the previous chapters, the CMOS image sensor is used in combination with fluorescence detection method to study biological cells. In this chapter, another important modality which is electrical stimulation capability of the CMOS chip is studied. As described in Chapter 2, one attractive feature of the CMOS chip is the capability of generating electrical stimulus and electrical potential recording on a 2D high spatial resolution array. This is useful for a variety of biological applications. For scientific research, such a device would be useful for interfacing with neuronal cells which form a direct coupling with the electrodes [1-3]. From the medical perspective, a device capable of electrical stimulus current exceeding the threshold of the retinal cells can potentially be used as a retinal prosthesis [4-6]. Fig. 5.1 shows the proposed CMOS sensor chip. In this work, a dedicated CMOS image sensor is developed to address the issue of generating stimulus current suitable for use as a retinal prosthesis. Coupled to the fluorescence imaging capability as described in earlier chapters, this work is expected to lead to a device to study the live intact brain in vivo.

Our aim is to develop a device that captures the image that falls onto the retina and deliver the necessary spatial and temporal electrical stimulus to the retina cells as shown in Fig. 5.2. The system proposed for developing the retinal implant chip is based on the PFM photosensor circuit [7]. With the PFM photosensor, we can implement photosensitivity adaptation very much like that of the mammalian retina [8]. This has been demonstrated in our previous work [9]. Due to the digital nature of the PFM output pulse, pulse image processing has also been shown [10]. A dedicated CMOS chip which is capable of photosensing and electrical stimulus has been developed. With this chip, we have demonstrated digital pulse output images that are suitable for retinal cell stimulation. Electrical stimulation of the retinal cells is generated via a

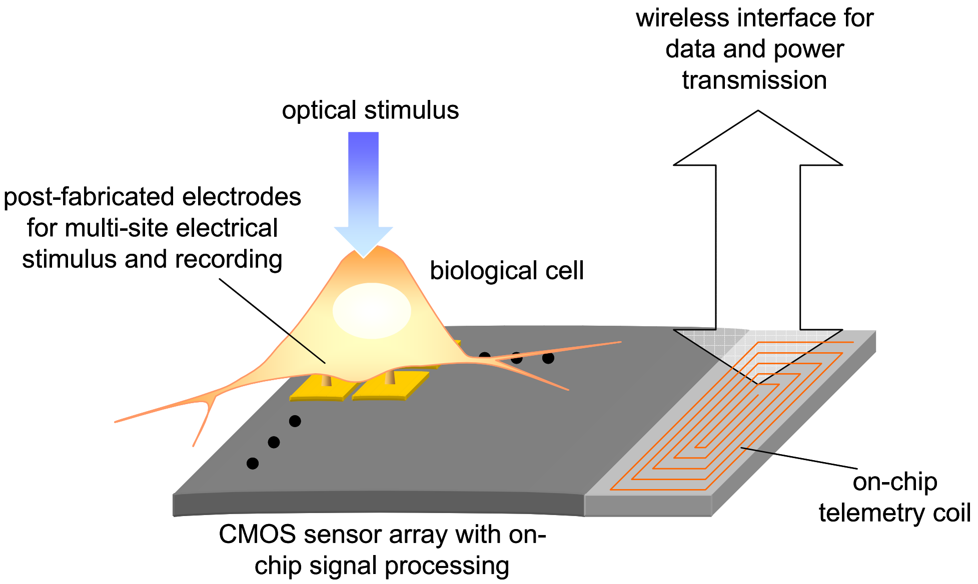

Fig. 5.1 Diagrammatic representation of the proposed CMOS sensor chip for neuroelectronic interfacing.

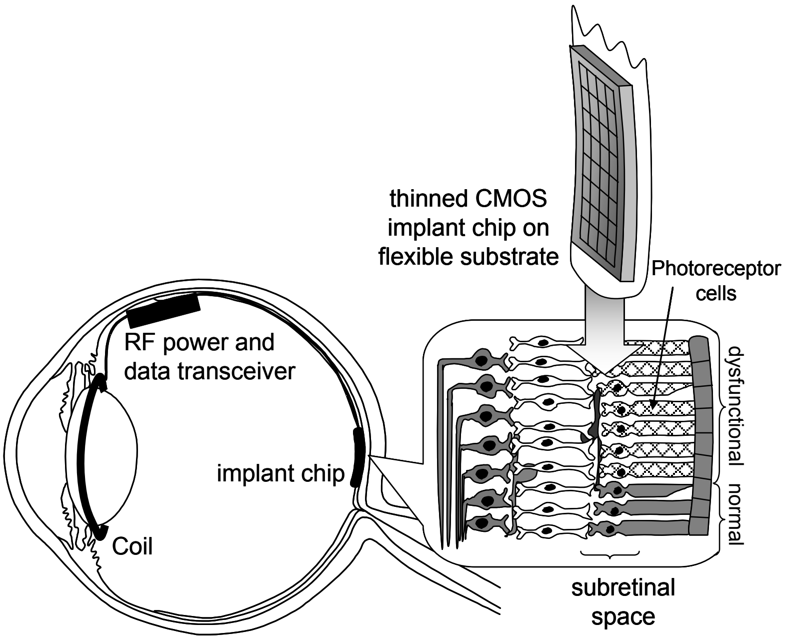

Fig. 5.2 The retinal implant chip is surgically implanted in the space occupied by the dysfunctional photoreceptor cells. It is powered wirelessly via a RF power and data to and from the chip is transitted wirelessly. In the implanted state, the chip would need to be compliant to the curvature of the eyeball.

programmable waveform generator that controls the stimulus current in a linear and exponential fashion.

A lot of research has focused on designing a retinal implant chip [11-13]. Many schemes were proposed and some chips have been implanted into various test subjects to assess their acute and chronic characteristics. Not much work, however, has gone into observing the effect of bending on the performance changes of these chips. In the implanted state, the chip must be bent to follow the curvature of the retina. This is to reduce injury to the eye as well as ensure a close and uniform contact with the cells for stimulation. By studying the semiconductor devices, we explain the behavior of these devices under bending. The main objective of this study is to determine the effect of bending on the characteristics of the CMOS circuit. The goal of bending is to reach the human retina curvature of about 0.08 mm^{-1}. By understanding this effect we hope to be able to design a retinal implant circuit to minimize the effect of bending. The basic MOS transistor was used in this work. Furthermore, the PFM photosensor was used as the case study in this work. We have experimentally determined the dependence of the PFM-based photosensor circuit on strain. We found that the PFM characteristic is dependent on the direction of bending. We have verified that a thinned-down microelectronic chip, when bent to the curvature of the human eye, shows negligible change in circuit characteristics.

5.2 Pulse Frequency Modulation CMOS Photosensor

In this work, the pulse frequency modulation photosensing (PFM) circuit is used extensively. Two versions of the PFM are utilized. One is suitable for implementation as a digital circuit, while the other permits operation with different source voltages. The former is used in the subretinal implant chip while the latter is used for studying LSI circuits under

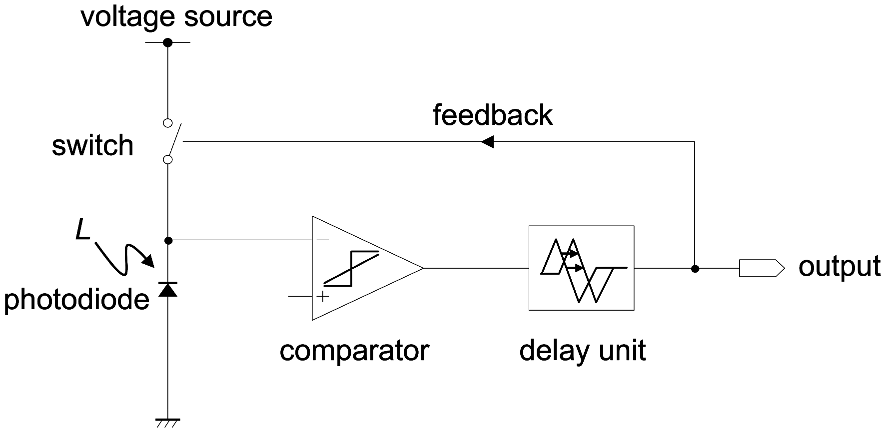

Fig. 5.3 Schematic of a general PFM photosensor circuit.

mechanical strain. As described in Chapter 2, the PFM circuit produces output pulses with frequency that is proportional to the intensity of incident light onto the photodiode [14, 15]. Generally, the circuit consists of photodiode with a reset switch that is controlled by feedback signal from the output. A comparator and a delay unit downstream of the photodiode completes the simple circuit as shown in Fig. 5.3. Two different implementation of the PFM circuit is studied; the digital and the analog PFM circuit.

The complementary metal oxide semiconductor (CMOS) photosensor, operating in pulse frequency modulation (PFM) mode, has several advantages over other methods as a retinal implant. It produces output pulses with frequency directly related to the intensity of incident light. Its dynamic range is relatively large, which is highly effective in the replacement of photoreceptors. In addition, it can operate at a very low voltage without decreasing the signal-to-noise ratio. We hope to be able to use this chip as a subretinal implant prosthesis in as well as other bioimaging applications in the future.

5.2.1 Digital PFM circuit

The digital PFM circuit is shown in Fig. 5.4. In this circuit, the comparator was implemented using an inverter, Inv. The D flip-flop forces the output of the PFM circuit to be synchronized to the input clock, PCLK, and also delays the feedback signal, rendering enough time for resetting the photodiode. The reset signal controls the reset switch, Mr, which is an n-channel MOSFET. The dynamic range of the PFM can be very large, with output frequency limited only by the switching speed of the reset transistor and the D flip-flop.

In order to determine the output frequency f_{out}, we model the photodiode as a simple current source and a capacitor connected in parallel. The photodiode is initially reset and charged to the maximum value of V_{DD}-V_{ThI}, where V_{ThI} is the threshold voltage of the reset transistor. Due to the capacitive load of the photodiode and inverter which are connected to the reset transistor, the maximum value of the photodiode voltage V_{PD} for a dynamically operated circuit such as the PFM or an active pixel sensor circuit never really reaches the source voltage V_{DD}. Instead, it peaks at a value which is lower. This can be verified by considering a NMOS transistor operating in the saturation region with its source terminal connected to a capacitor. As the photocurrent i_L, discharges the photodiode V_{PD} starts to fall. The moment V_{PD} reaches the inverter threshold voltage V_{ThI}, the inverter changes state. This is captured by the D flip-flop and its output switches high. The output signal is fed back to the reset transistor which resets the photodiode, which in turn causes the D flip-flop to go low on the next input clock. And the cycle repeats. A typical output of the PFM photosensor circuit is shown in Fig. 5.5. Using the simple capacitor model for the photodiode,

$$\frac{dV_{PD}}{dt} = -\frac{i_L}{C_{PD}}. \tag{5.1}$$

Assuming a linear voltage drop of V_{PD}, a valid assumption for short periods, we have

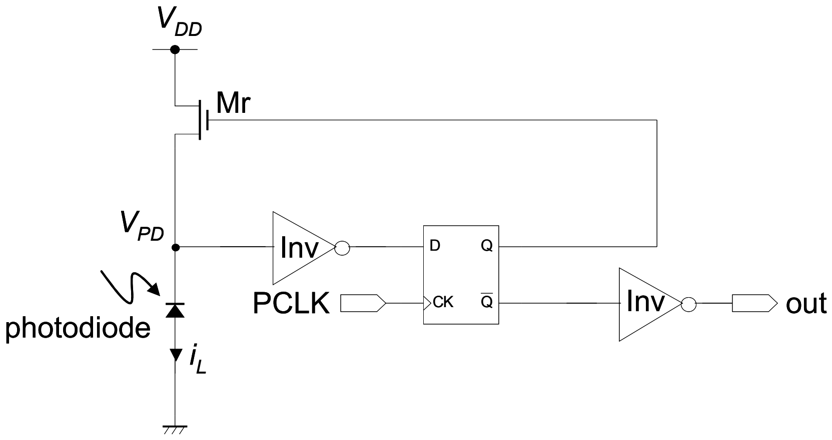

Fig. 5.4 Circuit of digital PFM photosensor implementation using inverter and D flip-flop.

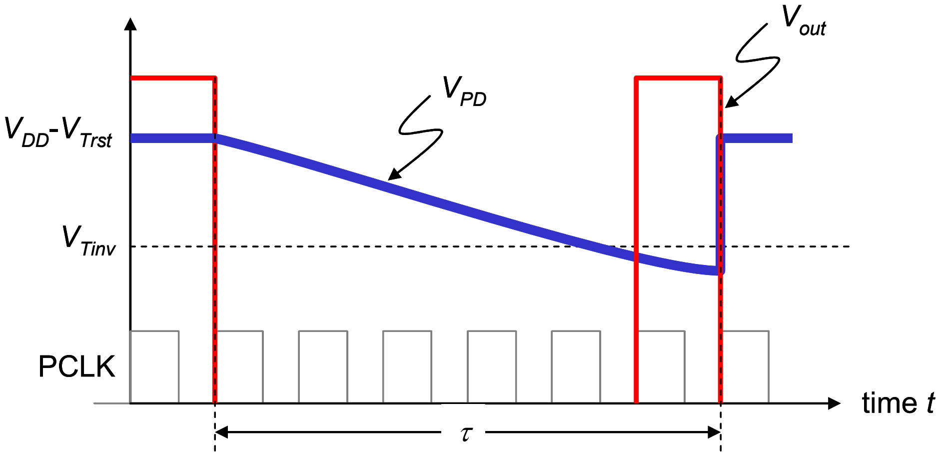

Fig. 5.5 Output of the digital PFM circuit.

$$\frac{\left(V_{DD}-V_{ThR}\right)-V_{ThI}}{\tau-\frac{1}{f_{clk}}}=\frac{i_L}{C_{PD}}, \tag{5.2}$$

which is simplified to give

$$f_{out}=\frac{F}{1+\frac{F}{f_{clk}}}, \tag{5.3}$$

where the output frequency

$$f_{out}=\frac{1}{\tau}, \tag{5.4}$$

and

$$F=\frac{i_L}{C_{PD}}\frac{1}{\left(V_{DD}-V_{ThR}-V_{ThI}\right)}, \tag{5.5}$$

Following a similar argument as discussed in Chapter 3, the photocurrent can be related to the incident illumination by the following equation,

$$L^{\gamma}=\frac{i_L}{A\cdot q\cdot\eta}, \tag{5.6}$$

where the photocurrent is related to the illumination light L, with the power correction factor $1/\gamma$. Here, A is the effective photodiode area, while q is the electron charge and η the quantum efficiency. Substituting (5.6) into (5.2) gives

$$f_{out}=\alpha\cdot L^{\gamma}, \tag{5.7}$$

where the constant,

$$\alpha=\frac{\left(A\cdot q\cdot\eta\right)}{C_{PD}}\frac{1}{\left(V_{DD}-V_{ThR}-V_{ThI}\right)}. \tag{5.8}$$

The pulse output pulses from the PFM circuit are almost comparable to the electrical signal used for eliciting neural response from the human retina [Margalit02, Ziegler04]. Due to its digital-like output pulse, only simple signal processing is required to produce biphasic current stimulation and image processing. The PFM circuit is simple and effective, making it the logical choice for implementation in a retinal implant chip.

5.2.2 Analog PFM circuit

A schematic of the analog PFM photosensor is shown in Fig. 5.6 (A). Here, the comparator is replaced by a Schmidt trigger inverter, and two inverters are used as the delay element. As will be shown later, the output from this PFM circuit is more dependent on the voltage sources. The same basic operation as described for the digital PFM circuit can be used to explain the operation of this analog circuit. However, compared to the macro level model involved in the digital PFM circuit, here, device level modeling is needed to describe the relationship of the PFM output to the various device parameters such as voltage source and carrier mobility. Furthermore, time dependency of the device characteristics need also be considered. For example, the reset transistor, Mr alternates between two operating states as shown in Fig. 5.6 (B). The photodiode is constantly being charged when the reset transistor, Mr, is in the on state and discharged when Mr is in the off state.

We start by considering Kirchoff's current law at C. Assuming current flow into the Schmitt trigger inverter, STInv is zero,

$$i_R + i_{PD} = 0, \tag{5.9}$$

where i_R is the drain current of the reset transistor Mr, and i_{PD} the photodiode current. This equation is valid for all time dependent (dynamic) and time independent conditions (static). Further, the reset transistor is assumed to be always operating in the linear region due to the dynamic characteristic of the circuit. Following the current-voltage characteristics of an n-channel MOS transistor, the drain current is given by,

$$i_r = \mu_N C_{ox} \left(W / L \right) \left[\left(V_{GS} - V_{ThR} \right) V_{DS} - V_{DS}^2 / 2 \right], \tag{5.10}$$

where, μ_N is the mobility of Mr, C_{ox} the gate oxide capacitance of Mr, W/L the width-to-length ratio of Mr, and V_{ThI} is the threshold voltage of Mr. Further, we note that

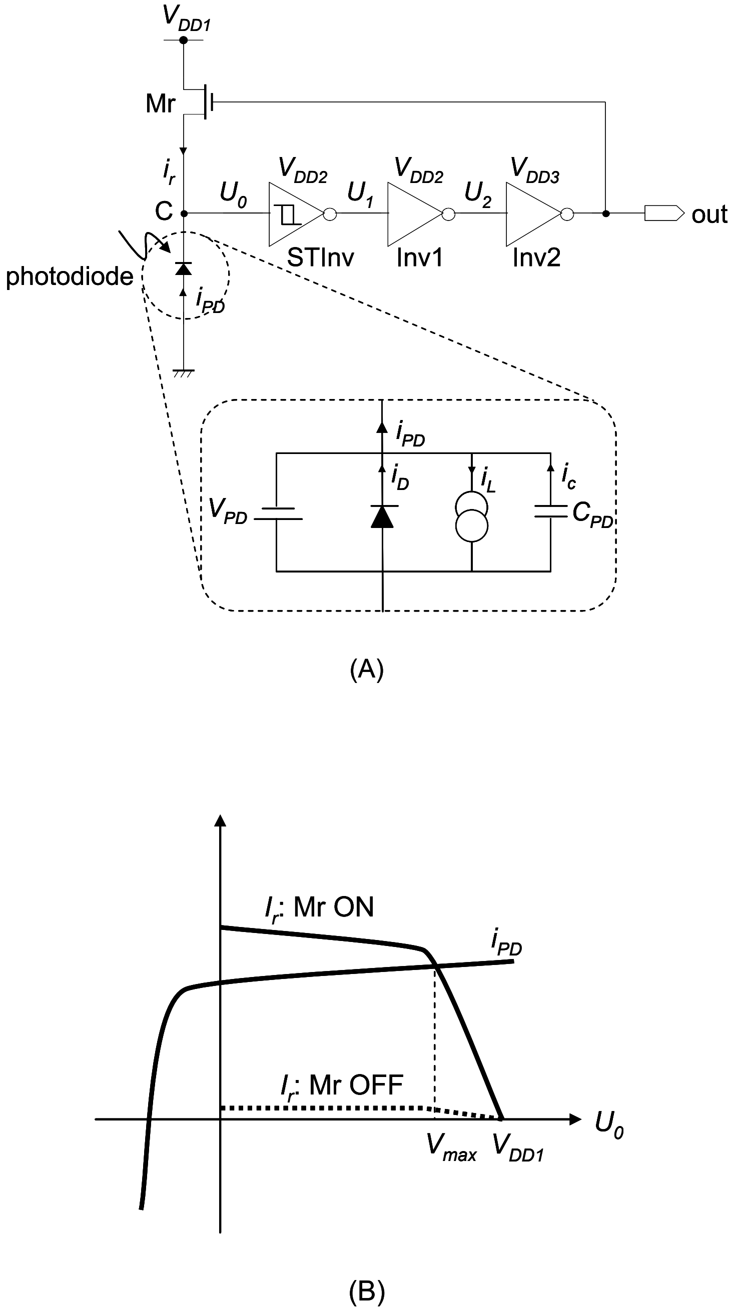

Fig. 5.6 (A) Analog circuit of PFM photosensor implemented using a Schmitt trigger inverter, STInv, and two inverters, Inv1 and Inv2. V_{DD1}, V_{DD2}, and V_{DD3} are the supply input voltages while VOUT is the output voltage. (B) Diagramatic representation of reset transistor current i_r and photodiode current i_{PD}.

$$V_{GS} = V_{out} - U_0, \tag{5.11}$$

and,

$$V_{DS} = V_{DD1} - U_0, \tag{5.12}$$

where, U_0 is the voltage at point C. The photocurrent i_{PD} can be described by using a combination of current terms as shown in Fig. 6. It takes the following form

$$i_{PD} = I_S\left(e^{(-U_0/V_{ther})} - 1\right) - i_L - C_{PD}\frac{dU_0}{dt}, \tag{5.13}$$

where I_S is the saturation current of the photodiode, V_{ther} the thermal voltage, i_L the photo generated current, and C_{PD} the photodiode capacitance. For the static case, i_{PD} can be approximated as i_L due to the larger magnitude of this term compared to other terms. However, this is not always true for the dynamic case.

A typical output of the analog PFM circuit is shown in Fig. 5.7 (A). Three distinct voltages, V_{max}, V_{limit}, and V_{min}, can be seen on the graph. The maximum voltage V_{max}, is theoretical maximum value of U_0. It is obtained by substituting eq. (5.10) and eq. (5.13) into eq. (5.9) and by equating $dU_0/dt=0$. This condition is equivalent to the case where the system has been sufficiently stabilized after a long time. However, for the PFM circuit that is constantly in operation, U_0 never reaches this theoretical maximum value. Instead, it is limited to V_{limit}. V_{limit} can be approximated by considering that the drain current in eq. (5.10) to zero on reset. By solving this equation, we obtain,

$$V_{DS} = 0, \tag{5.14}$$

and

$$\left(V_{GS} - V_{ThR}\right) - \frac{V_{DS}}{2} = 0. \tag{5.15}$$

By substituting eq. (5.11), and (5.12) into these eq. (5.14) and (5.15), we obtain

$$V_{\text{limit}} = U_0 = \max\begin{cases} V_{DD1} \\ 2\left(V_{DD3} - V_{ThR}\right) - V_{DD1} \end{cases}, \tag{5.16}$$

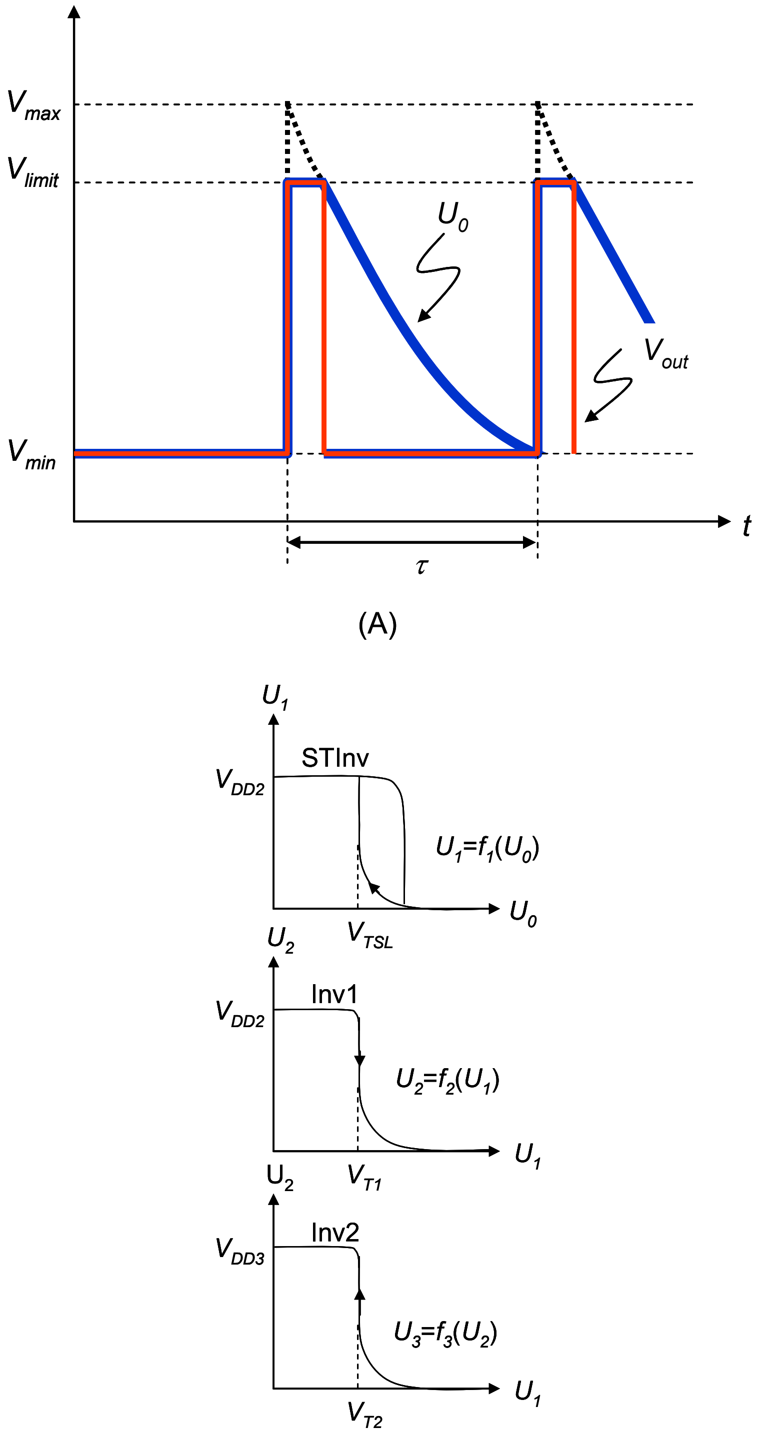

(A)

(B)

Fig. 5.7 (A) Output of analog PFM showing pulse width τ. (B) The input-output functions of STInv, Inv1 and Inv2 are given by *f1*, *f2*, and *f3*, respectively. V_{TSL}, V_{T1}, V_{T2} are the threshold voltages of STInv, Inv1 and Inv2, respectively.

where V_{limit} takes the maximum value of U_0. Next, V_{min} can be obtained by considering the voltage propagation along the circuit as shown in Fig. 5.7 (B). The voltage equivalent to V_{min} is when Mr is just turned on by V_{out},. This can be found by solving through the Schmitt trigger inverter and the inverter input-output functions, *f1*, *f2* and *f3*, respectively. In this case,

$$V_{\min} = U_0 = f_1^{-1} f_2^{-1} f_3^{-1} \left(V_{DD3} \right). \tag{5.17}$$

By approximation, it can be shown that $V_{\min} = f_1^{-1}\left(V_{DD2}\right)$ where V_{DD2} is the input voltage as shown in Fig. 5.6 (A).

Finally the PFM output can be found by approximating the photodiode to a simple capacitor model. In this model, the current drop across the capacitor is linear as a function of time which yields,

$$t = \frac{C_{PD}}{i_L}\left(V_{\max} - U_0\right), \tag{5.18}$$

where V_{max} is the initial voltage across the capacitor. At $t = \tau$, $U_0 = V_{min}$, and the frequency of the PFM

$$f_{out} = \frac{i_L}{C_{PD}\left(V_{\text{limit}} - V_{\min}\right)}, \tag{5.19}$$

where V_{max} is substituted to the practical value of V_{limit}.

From eq. (5.19), it can be seen that the output frequency depends on input source voltages as well as the device characteristics such threshold voltage. At the limit when V_{min} approaches V_{max}, the frequency approaches infinity and the output becomes flat as the output pulses merge together. On the other hand, by keeping the input voltages constant, the change in frequency is due to V_{min} which is determined by threshold voltages of the Schmidt trigger inverter which in turn is a function of the hole to electron mobility ratio of its transistors as will be shown later.

5.3 CMOS Sensor Chip

The proposed system architecture for the powering and controlling the CMOS sensor chip is shown in Fig. 5.8. The power receiver generates two voltage levels; a low 3 V and a high 5 V. The lower regulated voltage is used to run the circuitry, including powering the embedded processor. In order to drive sufficient current through the high impedance electrode-cell interface it is necessary to operate the chip in active mode [7, 16, 17]. The higher voltage is used for this purpose. We implemented a dual voltage supply because, as the chip is scaled down to deeper sub-micron technology, the stimulus voltage can be fixed, independent of the circuitry voltage. This architecture will greatly ease future development in miniaturizing the chip. The embedded microprocessor generates the clock (CLK), reset (RST), and communication signals (RW, EXEC, SCLK, SDA) to the serial communication unit in the retinal implant chip. These units are implemented by using external devices.

The actual chip itself consists of the image sensing and stimulus block, and the control block. The current generator produces the necessary stimulus current to drive the stimulus electrodes located inside the pixel array. The register bank unit stores the various system memories for clock generation and stimulus waveform parameters. The sequencer unit generates timing clock signals. The serial communication unit clock (SCLK) running at 500 kHz enables data to be written or read to 10-bit address and data buffers.

A simplified schematic of the pixel circuit is shown in Fig. 5.9. It consists of the digital PFM photosensing circuit, a 3-bit stimulus amplitude memory, and a 100 × 100 μm^2 stimulus electrode. The stimulus amplitude level for each pixel is set independently using the DATA signal and latched to the 3-bit memory at the rising edge of the CLKWDATA signal. An electrode activation switch in the form of a CMOS transmission gate is connected to the stimulus electrode. The p-n junction area of the NMOS and PMOS at 94.5 μm^2 and 189 μm^2,

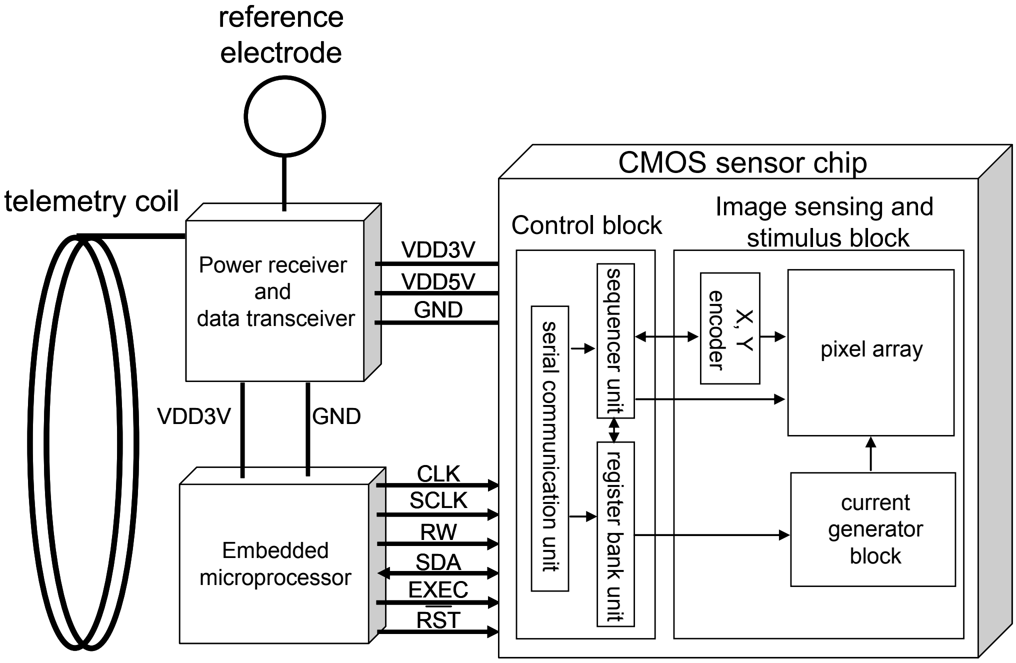

Fig. 5.8 Schematic of the proposed system architecture. The power receiver supplies voltages to power the chip and for electrical stimulation. The embedded microprocessor communicates with the sub-retinal implant chip to set the various stimulus waveform parameters.

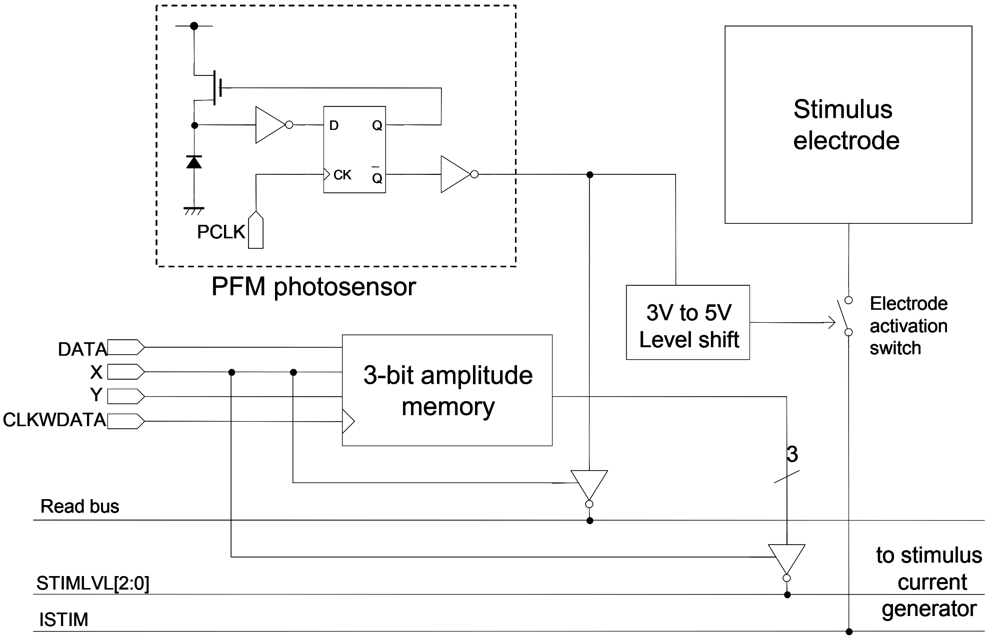

Fig. 5.9 Simplified schematic of the pixel showing the pulse frequency modulation photosensor circuit.

respectively provided adequate ESD protection. This was confirmed during testing of the device as no failure due to ESD was encountered during testing.

5.3.1 Stimulus Current Generation Circuit

It has been shown that retinal cells respond differently when stimulated with either a negative or positive pulse first [4, 6]. Also asymmetrical pulse (different phase amplitudes) has been reportedly used for retinal stimulation [18]. In order to cover the wide range of stimulation waveform requirements, we designed a programmable waveform generator. Seven parameters are used to define the stimulus waveform as shown in Fig. 5.10. The pulse width TPOS, TIMD, TNEG, and TPLS are 4-bit parameters each. The clock for generation of the pulse widths is STIMCLK. A frame is completed by scanning the column pixels using the x-decoder signal which also controls the tristate buffer output to stimlvl[2:0]. Using a 2 MHz base clock, a typical operation scenario would be 1 ms pulse width resolution for the stimulus pulse running at about 100 Hz.

In order to reduce the necessary circuit area but still maintain a wide stimulus range with fine tuning resolution, we implemented a 3-bit linear and exponential D/A. The schematic for the current generator array is shown in Fig. 5.11. The current generator is designed using a series of current mirror circuit with varying transistor sizes. The stimulus current amplitude level is first read from a pre-assigned 3-bit memory in each pixel. This is then used to set the exponential amplifier driving current. The global 3-bit positive and negative phase current, IOPOS[2:0] and IONEG[2:0], are used to tune the stimulus current to reach the desired value. The required current for stimulation, IREF is generated from the current generator unit. This current is passed through the linear D/A converter as shown in Fig. 5.12 (A), where the 3-bit IOPOS[2:0] and IONEG[2:0] signal generates a reference voltage, VREFPOS and VREFNEG

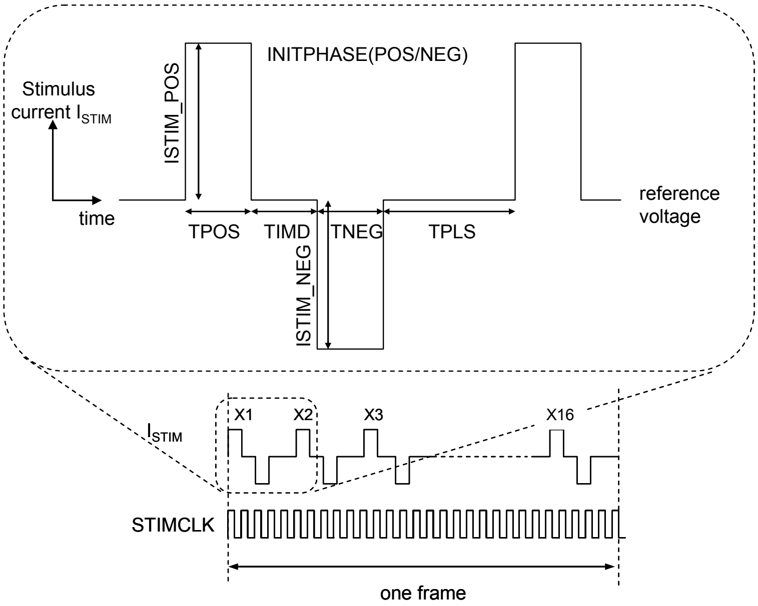

Fig. 5.10 The stimulus current waveform is fully determined using seven parameters: one to control the positive or negative phase order; four to control the pulse widths (TPOS, TIMD, TNEG, and TPLS); and two for the positive and negative amplitudes. Each row, consisting of 16 pixels, are output simultaneously as each column X is accessed sequentially.

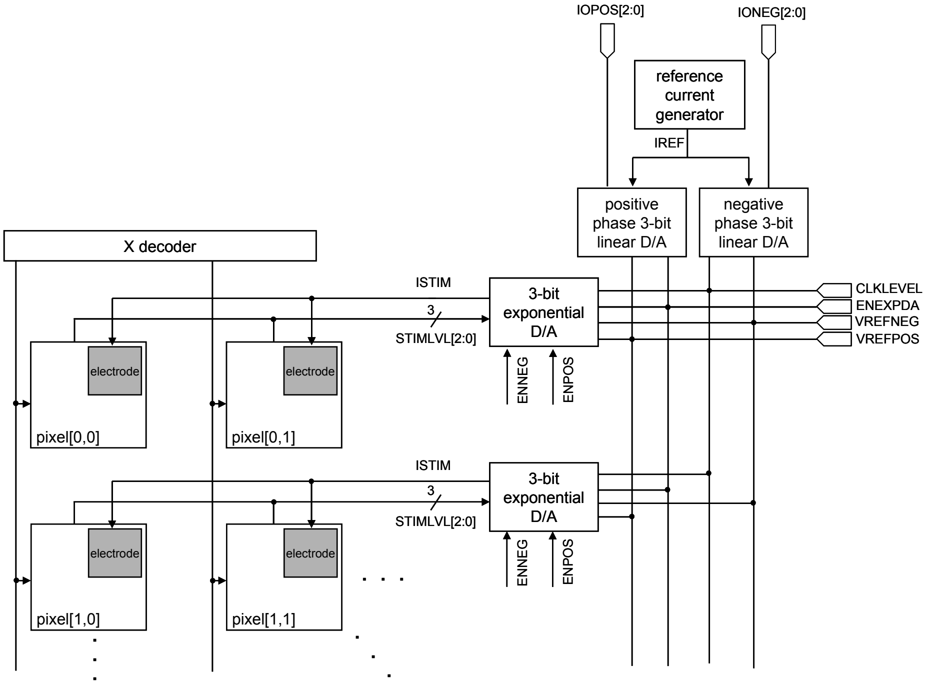

Fig. 5.11 Schematic of the stimulus current generator array block.

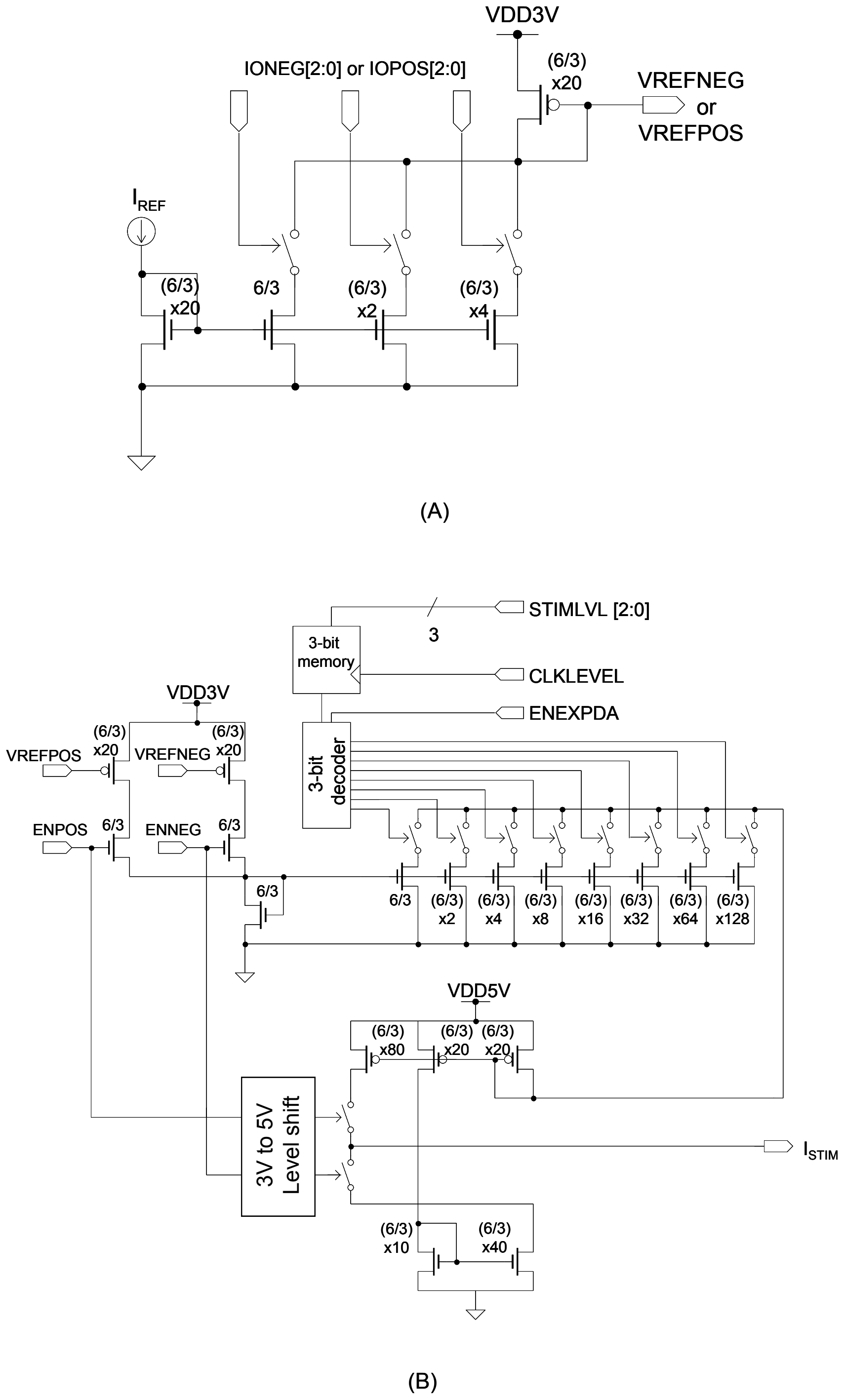

Fig. 5.12 Schematic of the (A) linear D/A, and (B) exponential D/A. Numerator and denominator values refer to the width and length (in μm) of the transistor gates respectively.

Table 5.1 Clock signals generated in control block

Clock	Frequency	Registers Used	Description
CLK	$f_{CLK} = 2MHz$	n/a	Input Clock
BASECLK	$f_{BASECLK} = f_{CLK}/2$	n/a	180^{O} phase shifted from CLK
PCLK	$f_{PCLK} = \frac{1}{2^{TPFM1}} \times \frac{1}{TPFM2+1} \times f_{BASECLK}$	TPFM1 TPFM2	PFM photosensor clock
STIMCLK	$f_{STIMCLK} = \frac{1}{2^{3}} \times \frac{1}{2^{TSTIM}} \times f_{BASECLK}$	TSTIM	Stimulus current generator clock

respectively. The linear D/A converter is implemented using a current source with three different transistor sizes. The reference voltage is then passed to the exponential D/A converter as shown in Fig. 5.12 (B) where the 3-bit STIMLVL[2:0] signal, through a 3-bit decoder, controls the stimulus current in an exponential fashion. The stimulus current is powered by the higher voltage source, VDD5V. The final stimulus current can be described using the following equation

$$I_{STIM} = I_{REF} \times \frac{IO}{20} \times 2^{STIMLVL} \times 4, \tag{5.20}$$

where IO is IOPOS when ISTIM is in the positive phase and IONEG when ISTIM is in the negative phase. This term represent the linearly increasing current. In order to reduce power consumption, current is generated only when pulses are required. This is controlled by the ENEXPDA signal, which enables the 3-bit exponential D/A.

5.3.2 Control Block

It is necessary to generate the control signals and clocks, described above, to operate the CMOS sensor chip. This is implemented as an off-chip solution. Eventually we will include it as part of the chip. The register bank, sequencer, and serial communication unit in the control

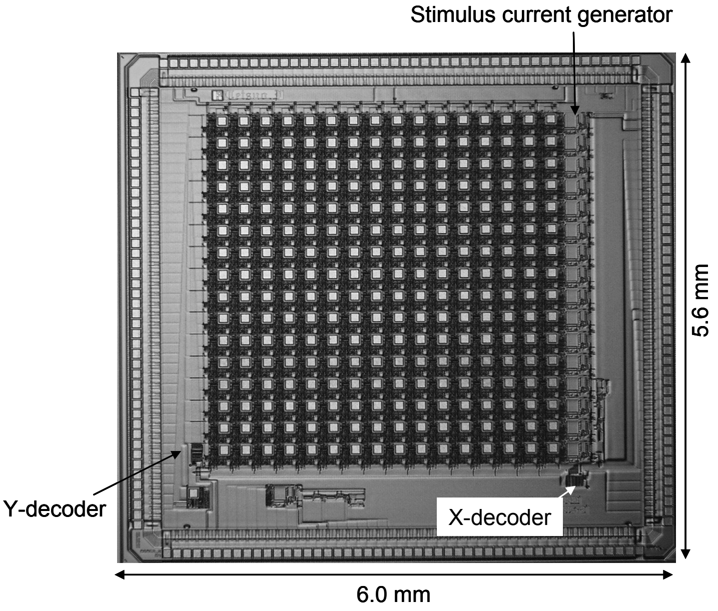

(A)

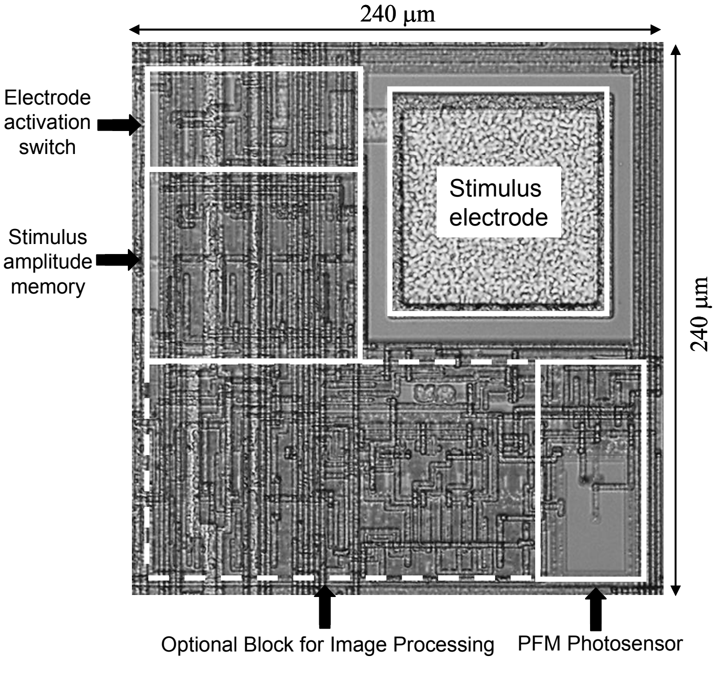

(B)

Fig. 5.13 (A) Photomicrograph of the fabricated retinal implant chip. (B) The enlarged view of the pixel.

Table 5.2 Specifications of subretinal implant chip.

Technology		0.6 μm CMOS (2-poly 3-metal)
Pixel	count	16 x 16
	size	240 μm x 240 μm
Frame rate		4 to 8,000 Hz
Voltage source		3 V (logic), 5 V (stimulus)
Base clock		2 MHz
Serial communication speed		500 kHz
Photodiode		n-well/p-substrate
Electrode size		100 μm x 100 μm
Amplitude resolution		3-bit exponential, 3-bit linear (biphasic)

block were designed using behavioral modeling, written in Verilog HDL. Registers are needed for setting the clock frequencies, and pulse parameters. The various clock signals are generated from the base clock as shown in Table 5.1.

5.4 Sensor Characteristic

The chip has been fabricated using standard 0.6 μm CMOS process. The microphotograph of the chip and the enlarged view of the pixel are shown in Fig. 5.13. The chip specification is listed in Table 5.2.

5.4.1 Photosensitivity

A typical output of the digital PFM photosensor circuit is shown in Fig. 5.14. An input signal of 1 MHz with a 50% duty cycle is used as the input clock, PCLK. A halogen lamp, with light intensities of up to 45000 lux, is used as the light source. Light intensity is measured using an illuminance meter (IM-5 Topcon, Japan). Pulse frequency is measured using a pulse counter (53131A Agilent, USA). The frequency of the output pulses shows a linearly increasing function

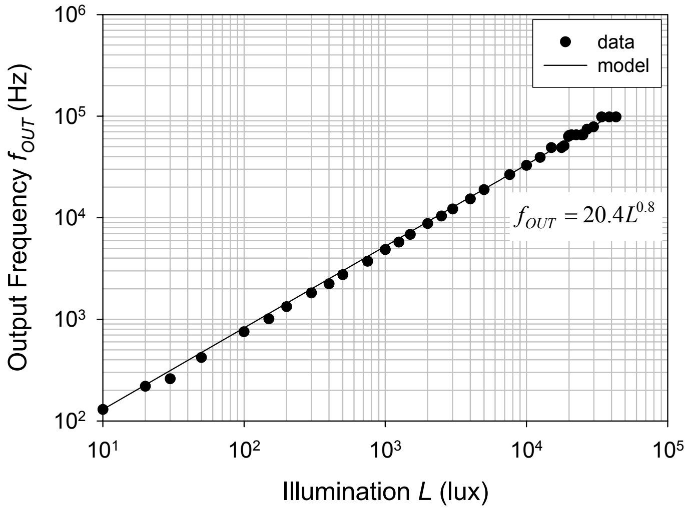

Fig. 5.14 Output of the PFM photosensor circuit.

over a light input intensity of about 4 decades (80 dB). We found that experimental values closely match the values as fitted by using eq. (5.7). The fitting parameters used here are α = 20.4 Hz/lux and γ = 0.80.

5.4.2 Image Sensing

The test setup used for measurement of the chip is shown in Fig. 5.14. In the experiment, the control block is implemented in FPGA (Altera Corp. CycloneTM EPIC12Q240C8 on HuMANDATA Ltd. CSP-024D board) for fast debugging and code finalization. This generates the necessary control and timing signals for the stimulus array chip. The output stimulus output current is measured under a probe station. In order to visualize the output image from the chip, we measured the output pulses using a digital input board (Interface PCI-2772C). Fig. 5.16 shows a typical output of the pixel array. A backlit object illuminates the chip and the output pulses are measured. The region with high light intensity shows a corresponding high frequency

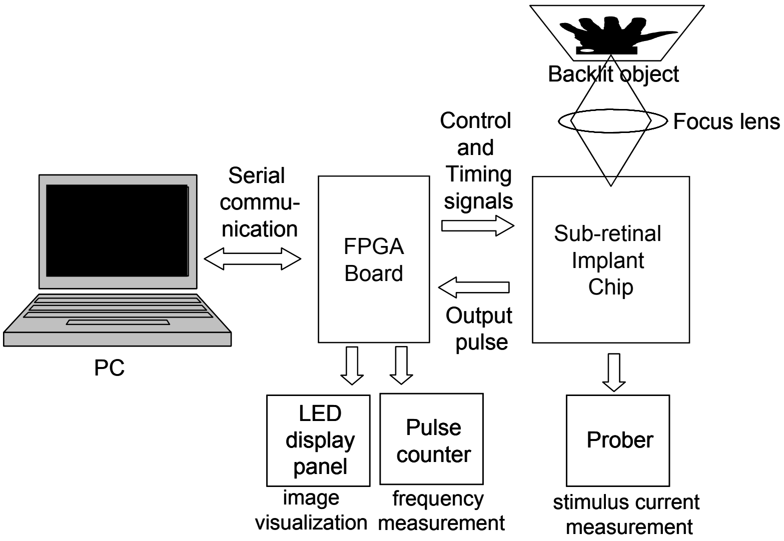

Fig. 5.15 Setup for test and measurement.

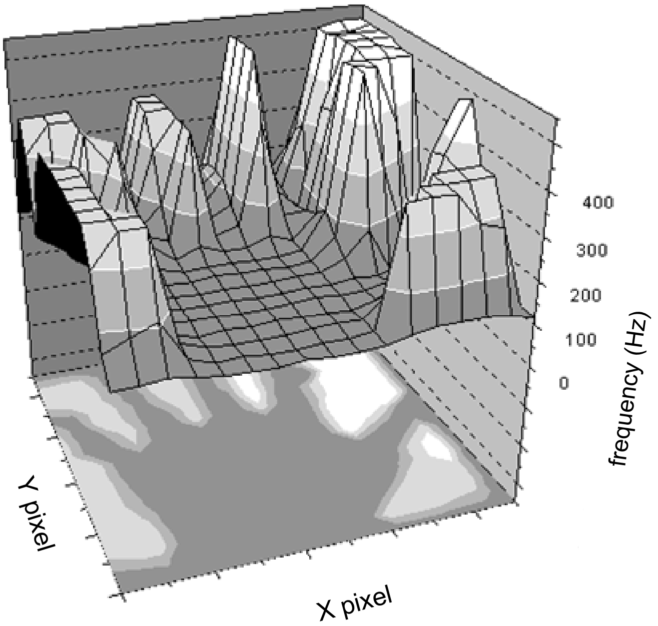

Fig. 5.16 Output of a backlit object visualized from the output pulse measurement.

pulse output while the region with low light intensity shows low frequency output. From the output we can clearly discern the image of a hand, which is used as the backlit object. Although the optimal number of electrodes has yet to be established, it is argued that some 500 to 1000 pixels are needed to restore useful vision [6]. Due to the size of the stimulus electrodes, the number of pixels is limited by the size of the chip. We demonstrated that 16 × 16 pixels can sufficiently resolve basic shapes such as that of the hand.

5.4.3 Stimulus Current Generation

By using a current-voltage converter with 1000 V/A gain, we measured the stimulus current for both the zero load and loaded cases. In order to simulate the stimulus electrode driving a stimulus current through the retina cells, we used a cell filled with saline solution (0.155 M NaCl at pH 6.4) and measured the current injected through the saline with a reference electrode placed around the stimulus electrode. The impedance of the cell at 1 kHz is about 80 kΩ. We have measured the exponential current increase by changing the 3-bit STIMLVL parameter. The result is shown in Fig. 5.17 (A). The reference voltage is set to 2.5 V. At current values below 500 μA, the difference between the positive and negative phase output is less than 5% for the loaded case, which is fairly reasonable. Overall, the current source circuit could maintain a drive current for both the loaded and zero load cases, with a maximum difference of about 8%. The stimulus current saturates at about 500 μA (for both the positive and negative phase currents) corresponding to the maximum output voltage swing of 5 V, which is the supply voltage rail. Fig. 5.17 (B) shows the linear biphasic current output. Combined, the linear and exponential incremental current values give a total of 64 current levels.

The stimulus current is measured by probing the stimulus electrode of the pixel. A typical output is shown in Fig. 5.18. There is some noise riding on the output current, but generally the

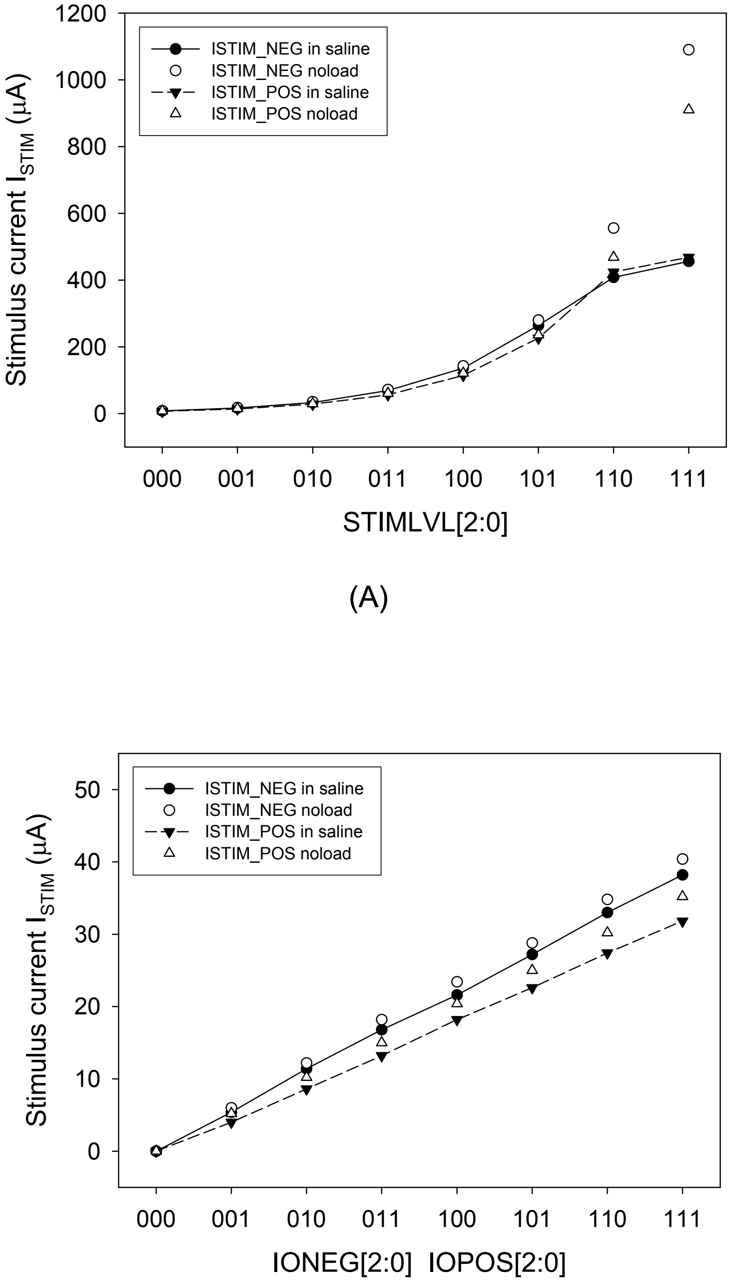

(A)

(B)

Fig. 5.17 (A) Exponential biphasic current amplifier output, and (B) Linear biphasic current amplifier output.

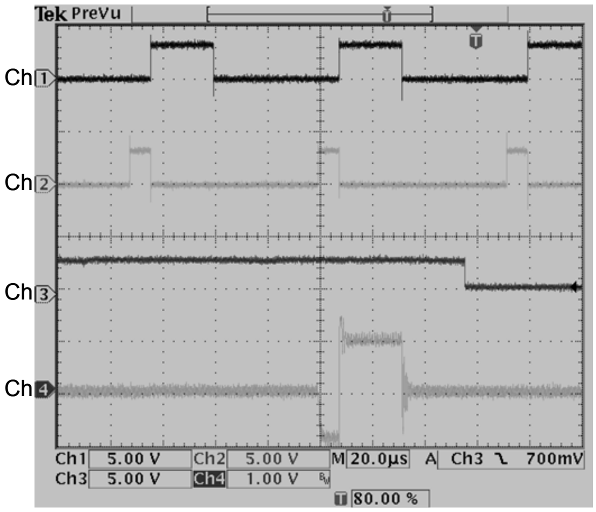

Fig. 5.18 Typical stimulus current output as measured on an oscilloscope. Ch1 and Ch2 are the ENPOS and ENNEG signal, respectively. Ch 3 is the ENEXPDA, while Ch4 is the generated output current. The stimulus parameters are: IOPOS = IONEG = 5, TPOS = 1, TNEG = 3, TIMD = 0

output follows the set parameters fairly well. The output stimulus current waveform is fully re-configurable during operation by changing the register values of each of its parameters.

There is a small discrepancy between the positive and negative phase pulse output currents. P- and n-channel MOSFETs are used for driving the positive and negative phase current respectively. Due to mismatch in transistor characteristics, the phase currents may not be equal. This mismatch, however, can easily be corrected by changing the various parameters in eq. (5.20) to reach the desired output current level. In our experiment, we have substituted the subretinal space with a saline cell. The electrical resistance of the subretinal space is about 50 kΩ for an area of 0.01 mm^2 [19]. Therefore, usage of the saline cell in our experiment can be justified. Generally it is accepted that a stimulus threshold current of 100 µA, corresponding to a charge injection of 0.1 nC at a 0.1 ms interval, will illicit neuronal response from the retinal ganglion cells [4]. In the subretinal space, lower threshold current has been reported [20]. From the experimental results, we have achieved a higher than 500 µA stimulus current output. We have applied the chip in in vitro verification with a detached frog retina whereby, stimulus currents below 100 μA was confirmed to be able to evoke retinal response [21]. By using a special packaging technique which included fabrication of a stacked Pt/Au electrode on top of the stimulus electrode [22], the device was tested for stimulation inside the sclera of a rabbit for two weeks with no significant degradation in performance. The special electrode arrangement offered sufficient protection from electrode dissolution due to charge imbalances. Because the stimulus current is raster scanned one pixel at a time, the maximum power consumption of the device due to stimulus current alone is about 2 mW.

In the future, we intend to reduce the size of the chip by using 0.35 μm CMOS process. Keeping the stimulus electrode area equal, we foresee a reduction of more than 50% for the pixel area. Also, the control block will be implemented on chip. The estimated size of the chip when fabricated using the new process is about 3 mm × 3 mm, subtending a visual field of 12°.

5.5 Effect of Mechanical Strain

5.5.1 Changes in Circuit Performance Due to Mechanical Strain

The basis of the effect of mechanical strain on MOSFET devices is the changes in p-channel metal oxide semiconductor (PMOS) and n-channel metal oxide semiconductor (NMOS) mobilities under compression and tension. This can be explained by considering the change in the piezoresistance of the inversion layer. This has been verified experimentally by the extensive work carried out by numerous researchers [23-25]. This work is extended to include the dependence of PFM frequency output on strain. We explain this dependency by observing the surface inversion layer mobility of both the NMOS- and PMOS-based devices such as the Schmitt trigger inverter and CMOS inverters. For the case of a more complicated circuit like the analog PFM,

The current flowing in the NMOS transistor channel given in eq. (5.10). A more complete description would involve the channel length modulation coeeficient λ to give

$$i_d = \mu_N C_{ox} (W/L)\left[(V_{GS} - V_{ThR})V_{DS} - V_{DS}^2/2\right][1 + \lambda V_{DS}]. \tag{5.21}$$

Changes in the current flow can be due to any number of parameters in the equation. The general case would involve all the parameters as shown in the following equation.

$$\frac{\Delta i_{dn}}{i_{dn}} = \frac{\Delta \mu_N}{\mu_N} + \frac{\Delta C_{ox}}{C_{ox}} + \left(\frac{\Delta W}{W} - \frac{\Delta L}{L}\right) + \frac{\Delta V_{DS}}{V_{DS}} + \frac{\Delta(V_{GS} - V_{Th} - V_{DS}/2)}{(V_{GS} - V_{Th} - V_{DS}/2)} + \frac{\Delta(1 - \lambda V_{GS})}{(1 - \lambda V_{GS})}. \tag{5.22}$$

Terms containing constants which includes the second term and all the terms containing voltage are equal to zero, which leaves,

$$\frac{\Delta i_{dn}}{i_{dn}} = \frac{\Delta \mu_N}{\mu_N} + \left(\frac{\Delta W}{W} - \frac{\Delta L}{L}\right). \tag{5.23}$$

Hence, changes in current can be said to be due to changes in carrier mobility or changes due to gate geometry. By definition, conductivity, σ is the reciprocal of resistivity, ρ. And conductivity is directly proportional to mobility. The change in mobility is related to strain in the following manner.

$$\frac{\Delta \mu}{\mu} = -\frac{\Delta \rho}{\rho} = -Y \cdot \varepsilon \cdot \Pi \tag{5.24}$$

Where Y is the Young's modulus, ε is strain, and Π the piezoresistivity which has directional property. Further, the longitudinal change in dimension of transistor gate length L is equal to the strain by definition. Whereas, the transverse changes in dimension of the gate width W is related to strain in the following manner,

$$\frac{\Delta W}{W} = -\nu \cdot \varepsilon. \tag{5.25}$$

Hence, eq. (5.23) can be rewritten in terms of the strain as,

$$\frac{\Delta i_{dn}}{i_{dn}} = -\varepsilon\left(Y \cdot \Pi + (\nu - 1)\right). \tag{5.26}$$

From the above analysis, it can be seen that changes in transistor current is directly proportional to the applied mechanical strain. This analysis can be further applied to a combination of transistors once the directionality of the gate structures from the layout is known.

The output frequency of the analog PFM circuit is dependent on the V_{min} term as shown in eq. (5.19). This term is related to the threshold voltage of the Schmitt trigger inverter. And the threshold voltage is related to the transistors In order to simplify our analysis, as a first approximation, we took V_{min} to be the lower threshold voltage V_{TSL} of the Schmitt trigger inverter [26]. In this case,

$$V_{\min} = V_{TSL} = \frac{V_{ThN2} + \sqrt{3n}\left(V_{DD2} - V_{ThP4}\right)}{1+\sqrt{3n}}, \tag{5.27}$$

where V_{ThN2} and V_{ThP4} are the threshold voltages of the M2 and M4 transistors of the Schmitt trigger inverter as shown in Fig. 20, and n is the mobility ratio of holes to electrons, respectively (see Appendix B for derivation). The *W/L* ratio of M4 and M2 are 5.4/0.6 and 1.8/0.6, respectively. Simulation of the PFM output pulse frequency matching the experimental settings was performed. The variables used were, V_{DD1} = 0.8V, V_{DD2} = 0.6 V, V_{DD3} = 1 V, V_{ThN2} = 0.7 V, and V_{ThP4} = -0.7 V. From the simulation result, we found that V_{min} = 0.6 V_{TSL} allows the model to optimally fit the simulation results. Here V_{DD3} and V_{DD1} are the input voltages while V_{TSL} is the lower threshold voltage of the Schmitt trigger inverter.

5.5.2 Sample Preparation and Measurement Setup

In order to study the directional property of the PFM, we prepared the layout of the MOS devices with the channel oriented such that the flow of current was in the $\left[\bar{1}\ 1\ 0\right]$ and $\left[1\ 1\ 0\right]$

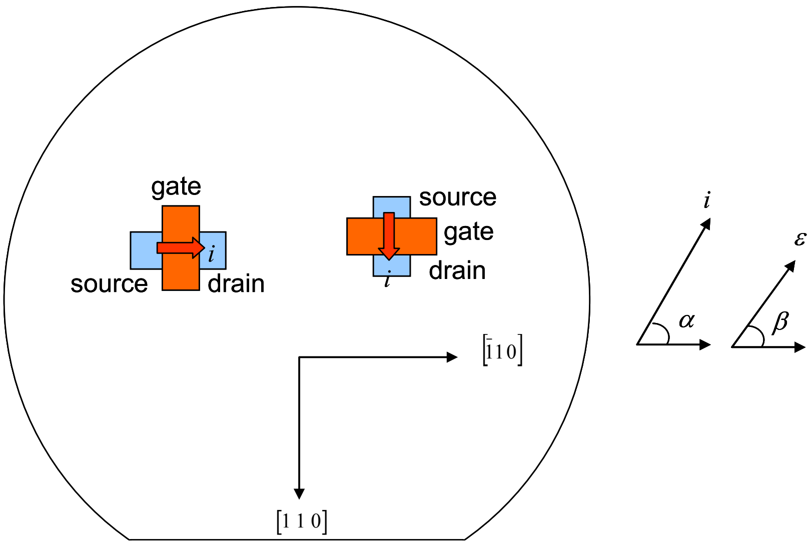

Fig. 5.19 Crystallographic directions $[1\,1\,0]$ and $[\bar{1}\,1\,0]$ on the wafer are shown together with MOSFET current flow *i* and strain ε directions.

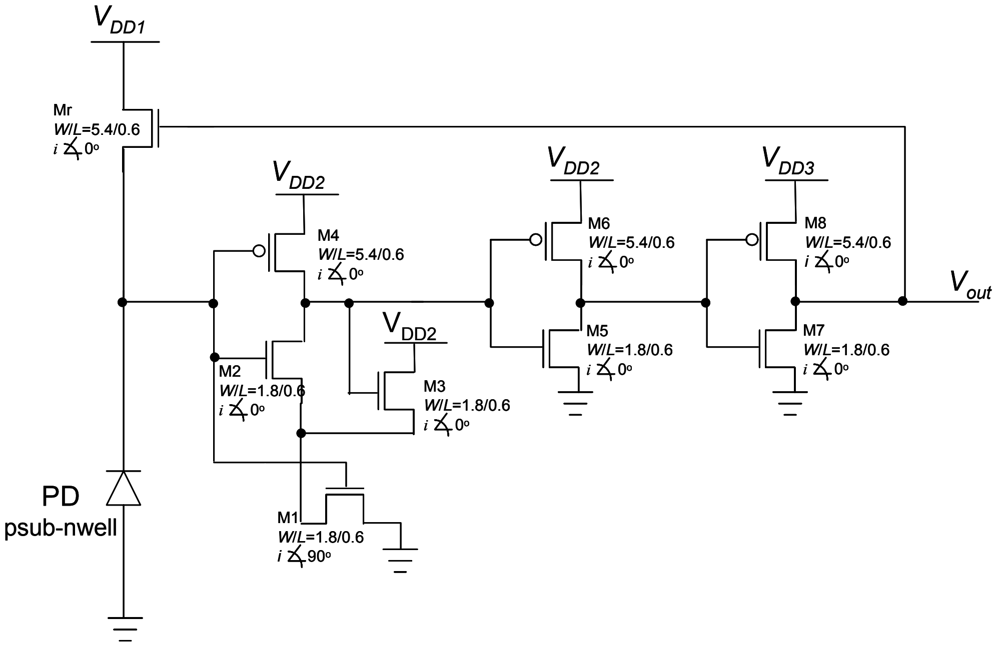

Fig. 5.20 Layout of PFM circuit with orientation of channel current flow direction. The operating voltage of V_{DD1}, V_{DD2}, and V_{DD3} are 0.8 V, 0.6 V, and 1.0 V respectively.

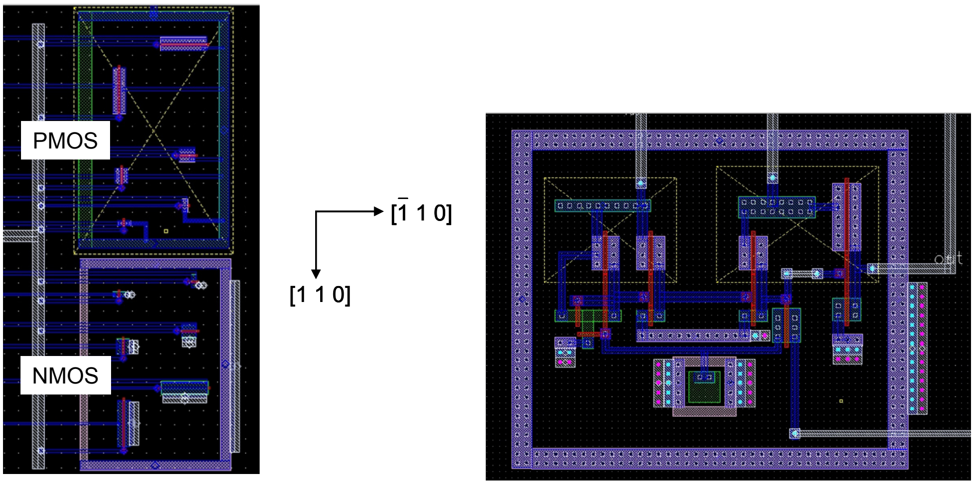

(A) (B)

Fig. 5.21 (A) NMOS and PMOS device layout. (B) PFM device layout

directions only. Using the $\left[\bar{1}\;1\;0\right]$ direction as the datum, the orientation of current flow and strain is shown in Fig. 19. Depending on the device orientation and the direction of strain, α-β = is equal to 0° or 90° where the angles α and β are defined as shown in Fig. 5.19. The orientation-dependent layout of the analog PFM circuit with orientation direction is shown in Fig. 5.20. The layout of the MOS transistors and the PFM circuit is shown in Fig. 5.21.

In order to conduct the bending experiment, a bending jig was used. In this jig, uniaxial bending is possible. In order to make the chip compliant to bending, the chip was thinned down to approximately 50 μm. The chip was attached onto the polyimide substrate with double-sided adhesive tape. A schematic of the bending jig is shown in Fig. 5.22 (A). Various layer thicknesses were measured using a micrometer. The radius of curvature was determined optically using a parallel laser beam illuminating the chip. The radius of curvature R is equal to $d_1\left(2\sin\theta\right)$, where the angle θ is calculated using $\tan 2\theta = \left(d_2 - d_1\right)/2L$ for positive curvature. For negative curvature θ is calculated from eq. (5)

$$\tan 2\theta = \begin{cases} \dfrac{(d_1 - d_2)}{2L}, d_1 > d_2 \\ \dfrac{d_2}{2L} \quad , d_1 = d_2 , \\ \dfrac{(d_1 + d_2)}{2L}, d_1 \le d_2 \end{cases} \tag{5.28}$$

where d_1 is the width of the incident laser beam and d_2 is the width of the reflected laser beam at length L from the chip as shown in Fig. 5.22 (B).

In our experiment, illuminations of 500, 1000, and 2000 lux were tested. The incident light intensity on the chip was measured externally via an illuminance meter (Line Seiki EL1000, range: 0-19990 lux). The halogen lamp power setting was stabilized for 10 min before measurements were taken.

5.5.3 Experimental Result

The output frequency of the PFM can be evaluated at different values of α and β. Two special cases were considered, i.e., PMOS and NMOS oriented at α-β = 0° and 90°, respectively. We found that the channel current flow of these MOS devices varies with crystallographic orientation and the amount of applied bending, as shown in Fig. 5.23. Under any operating conditions, the drain current of a PMOS or NMOS can be assumed to be a linear function of only the mobility term [24, 25]. From this simple relationship between current and mobility, we deduce that bending affects mobility and current in the same order. Our experimental results on bending of PMOS and NMOS confirm this linear relationship. Also, we note that the rate of change of n (with respect to curvature) is positive for the α-β = 90° case and negative for the α-β = 0° case.

Using the BSIM3v3 spice model for the MOSFETs and standard 0.6 μm CMOS technology process parameters, we simulated the operation of the PFM by changing the

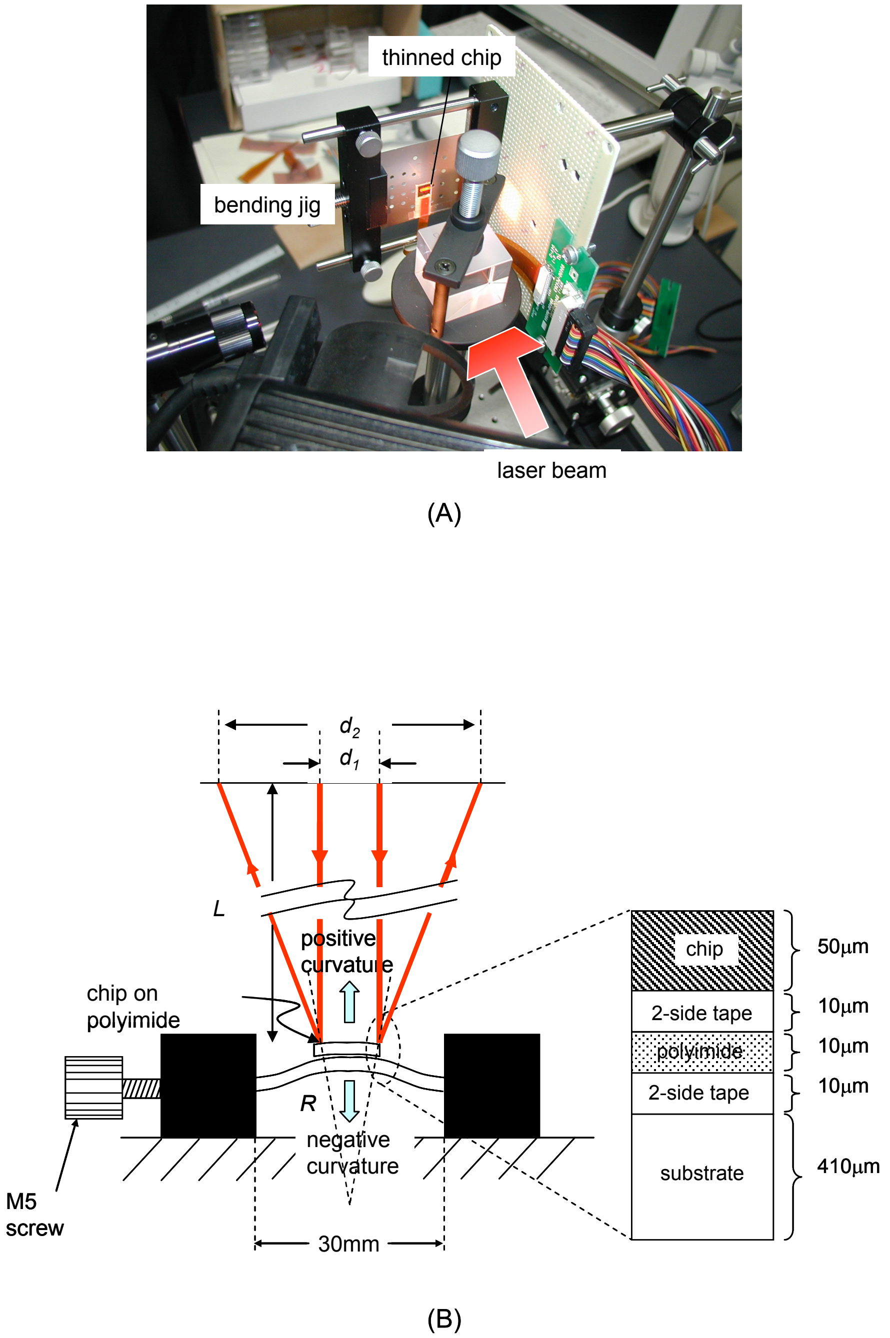

Fig. 5.22 (A) Jig for Bending Experiment. (B) Schematic of bending jig and curvature measurement by laser beam. The thickness of the various layers is shown in the inset.

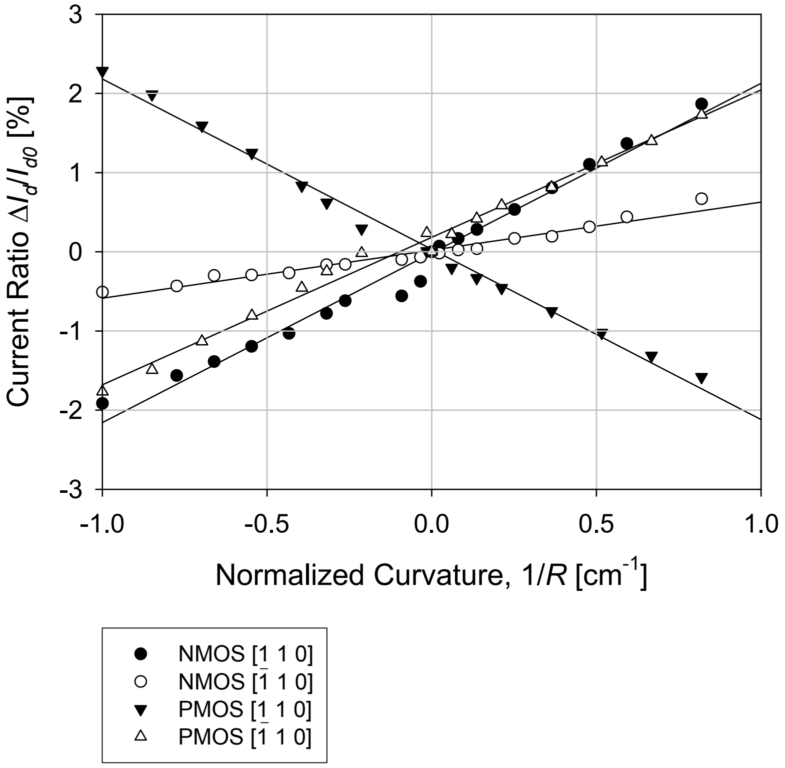

Fig. 5.23 The change of surface inversion mobility can be seen by measuring the channel flow current of the MOS transistors. In this figure, the saturation current, I_d of PMOS and NMOS with channel width and length ratio, W/L = 1.8 μm/0.6 μm at two perpendicular orientations were measured with respect to the amount of bending. Here the ratio of change of current, ΔI_d ($=I_d-I_{d0}$), to the current at zero curvature I_{d0} is plotted against the curvature $1/R$.

mobility values of all the PMOS and NMOS independently. The photodiode photon-to-current conversion was simulated by substituting the incident light, with a correspondingly suitable photogenerated current. Calculation of the PFM output frequency was carried out using eq. (5.19), again by varying the value of n. It can be seen that the PFM output frequency is an increasing function of *n* for positive values of *n*. Hence, the rate of change of frequency will be in proportion to the rate of change of n within the range of interest. This confirms our initial observation whereby the mobility ratio *n* varies linearly with bending. We found that the rate of change of *n* of -0.1 and 0.03 in the simulation for α-β = 0° and 90° respectively, gives modeling

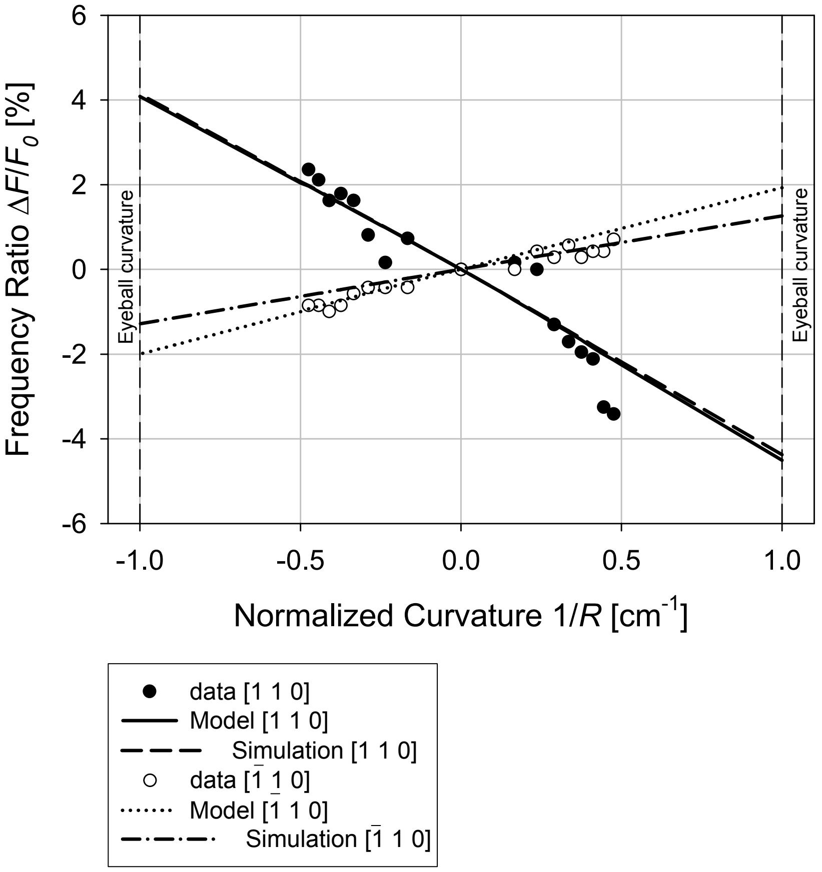

Fig. 5.24 Output frequency of PFM for two perpendicular bending directions $[1\,1\,0]$ and $[\bar{1}\,1\,0]$ are shown. The y-axis shows the normalized frequency variation, $\Delta F/F_0$ while the x-axis shows the normalized curvature to the human eye. Here ΔF is defined as F-F_0 while F_0 is the frequency at zero curvature. Comparison is made among the experiment, simulation and calculation from model eq. (5.19). For the simulation and modeling, the rates of change are n of -0.1 and 0.03 for the $[1\,1\,0]$ and $[\bar{1}\,1\,0]$ directions respectively.

results that match our simulation results. When these results are combined, we observed that there is fairly close agreement among experimental, simulation, and modeling results as shown in Fig. 5.24. Hence, this verifies our assumption that changes in mobility play a major role in the change of output frequency of the PFM photosensor.

When the simulation result is extrapolated to the curvature of the human eye (negative curvature in the implanted state), we see that the maximum variation in frequency is about +4.0%. This implies that the effect of bending can be ignored.

5.6 Summary

We have developed a CMOS image sensor chip for subretinal implantation based on the PFM photosensor circuit. Image sensing of sufficient resolution has been achieved from the 16 × 16 pixel array sensor. A linear and exponentially controlled biphasic stimulus current exceeding the threshold levels of the human retina has also been demonstrated. Next we have shown the dependence on strain on the transistor characteristic. This analysis is expanded to cover its effect on the PFM-based photosensor output frequency. The change in frequency is explained in terms of change in mobility, which affects LSI devices in a predictable way. A negligible variation of output frequency was found in the case of the PFM circuit when bend to the curvature of the human eye.

References

[1] P. Fromherz, “Neuroelectronic interfacing: semiconductor chips with ion channels, nerve cells, and brain,” in *Nanoelectronics and Information Technology*, R. Waser, ed., Berlin: Wiley, 2003, pp. 781-810.

[2] M. O. Heuschkel, M. Fejtl, M. Raggenbass, D. Bertrand, P. Renaud, “A three-dimensional multi-electrode array for multi-site stimulation and recording in acute brain slices,” *J. Neurosci. Methods*, vol. 114, pp. 135–148, Mar. 2002.

[3] K. Najafi, K. D. Wise, “An implantable multielectrode array with on-chip signal processing,” *IEEE J. Solid-State Circuits*, vol. Sc-21, pp. 1035-1044, Dec. 1986.

[4] E. Margalit, M. Maia, J. D. Weiland, R. J. Greenberg, G. Y. Fujii, G. Torres, D. V. Piyathaisere, T. M. O’Hearn, W. Liu, G. Lazzi, G. Dagnelie, D. A. Scribner, E. de Juan Jr, M. S. Humayun, “Retinal prosthesis for the blind,” *Surv. Opthalmol.*, vol. 47, pp. 335-356, Jul. 2002.

[5] E. Zrenner, “Will retinal implants restore vision?” *Science*, vol. 295, pp. 1022-1025, Feb. 2002.

[6] M. S. Humayun, E. de Juan Jr., J. D. Weiland, G. Dagnelie, S. Katona, R. Greenberg, S. Suzuki, “Pattern electrical stimulation of the human retina,” *Vision Res.*, vol. 39, pp. 2569-2576, Jul. 1999.

[7] J. Ohta, N. Yoshida, K Kagawa, M. Nunoshita, “Proposal of application of pulsed vision chip for retinal prosthesis,” *Jpn. J. Appl. Phys.*, vol. 41, pp. 2322-2325, Apr. 2002.

[8] B. Sakmann, O.D. Creutzfeldt, “Scotopic and mesopic light adaptation in cat’s retina,” *Pfugers Arch.*, vol. 313, pp. 168-185, 1969.

[9] K. Kagawa, K. Isakari, T. Furumiya, A. Uehara, T. Tkuda, J. Ohta, M. Nunoshita, “Pixel design of a pulsed CMOS image sensor for retinal prosthesis with digital photosensitivity control,” *Electron. Lett.*, vol. 39, pp. 419-421, Mar. 2003.

[10] K. Kagawa, K. Yasuoka, D. C. Ng, T. Furumiya, T. Tokuda, J. Ohta, M. Nunoshita, “Pulse-domain digital image processing for vision chips applicable to low-voltage operation in deep-submicron technologies,” *IEEE J. Select. Topics Quantum Electron.*, vol. 10, pp. 816-828, Jul. 2004.

[11] W. Liu, K. Vichienchom, M. Clements, S. C. DeMarco, C. Hughes, E. McGucken, M. S. Humayun, E. de Juan, J. D. Weiland, R. Greenberg, "A neuro-stimulus chip with telemetry unit for retinal prosthetic device," *IEEE J. Solid-State Circuits*, vol. 35, pp. 1487-1497, Oct. 2000.

[12] G. J. Suaning, N. H. Lovell, "CMOS Neurostimulation ASIC with 100 Channels, scaleable output, and bidirectional radio-frequency telemetry," *IEEE Tran. Biomed. Eng.*, vol. 48, pp. 248-260, Feb. 2001.

[13] A. Y. Chow, M. T. Pardue, V. Y. Chow, G. A. Peyman, C. Liang, J. I. Perlman, N. S. Peachey, "Implantation of silicon chip microphotodiode arrays into the cat subretinal space," *IEEE Trans. Neural Syst. Rehab. Eng.*, vol. 9, pp. 86-95, Mar. 2001.

[14] W. Yang, "A wide-dynamic-range, low power photosensor array", in *IEEE ISSCC Dig. Tech. Papers*, 1994, pp. 230-231.

[15] F. Andoh, H. Shimamoto, and Y. Fujita, "A digital pixel sensor for real-time readout," *IEEE Trans. Electron Devices*, vol. 47, pp. 2123-2127, 2000.

[16] M. Schwarz, R. Hauschild, B. J. Hosticka, J. Huppertz, T. Kneip, S. Kolnsberg, L. Ewe, H. K. Trieu, "Single-chip CMOS image sensors for a retina implant system," *IEEE Trans. Circuits Syst. II*, vol. 46, pp. 870-877, Jul. 1999.

[17]D. Ziegler, P. Linderholm, M. Mazza, S. Ferazzutti, D. Bertrand, A.M. Ionescu, Ph. Renaud, "An active microphotodiode array of oscillating pixels for retinal stimulation," *Sens. Actuators A*, vol. 110, pp. 11-17, 2004.

[18] M.N. Nadig, "Development of a silicon retinal implant: cortical evoked potentials following focal stimulation of the rabbit retina with light and electricity," *Clin. Neurophysiol.*, vol. 100, pp. 1545-1553, 1999.

[19] C.J. Karwoski, D.A. Frambach, L. M. Proenza, "Laminar profile of resistivity in frog retina," *J. Neurophysiol.*, vol. 54, pp. 1607-1619, 1985.

[20] A. Stett, W. Barth, S. Weiss, H. Haemmerle, E. Zrenner, "Electrical multisite stimulation of the isolated chicken retina," *Vision Res.*, vol. 40, pp. 1785-1795, Jun. 2000.

[21] T. Furumiya, D. C. Ng, K. Yasuoka, K. Kagawa, T. Tokuda, M. Nunoshita, J. Ohta, "Functional verification of pulse frequency modulation-based image sensor for retinal prosthesis by in vitro electrophysiological experiments using frog retina," *Biosens. Bioelectron.*, 2005, in press.

[22] T. Tokuda, Y.-L. Pan, A. Uehara, K. Kagawa, M. Nunoshita, J. Ohta, “Flexible and extendible neural interface device based on cooperative multi-chip CMOS LSI architecture,” *Sens. Actuators A*, vol. 122, pp. 88-98, Mar. 2005.

[23] A. Hamada, T. Furusawa, N. Saito, E. Takeda, “A new aspect of mechanical stress effects in scaled MOS devices,” *IEEE Trans. Electron Devices*, vol. 38, pp. 895-900, Apr. 1991.

[24] H. Mikoshiba, “Stress-sensitive properties of silicon-gate MOS devices,” *Solid-State Electron.*, vol. 24, pp. 221-232, Mar. 1981.

[25]A. P. Dorey, T. S. Maddern, “The effect of strain on MOS transistors,” *Solid-State Electron.*, vol. 12, pp. 185-189, Mar. 1969.

[26] S. -M. Kang, Y. Leblicci, CMOS Digital Integrated Circiuits: Analysis and Design, 3rd. ed., International Ed.: Mc-Graw-Hill Higher Education, 2003, pp. 350-353.

Chapter 6

Conclusions

The main theme throughout this entire thesis is the application of CMOS image sensors for bioimaging applications. We adopted the use of a CMOS technology for fabrication of the sensor due to the possibility of multiparameter sensing. In this work, we have explored and solved many issues related to photosensing, fluorescence detection, packaging for on-chip imaging, and electrical stimulation. When applied for in vivo imaging, initially we encountered some difficulties in providing sufficient excitation light inside the mouse brain. However, this issue was resolved during in vivo verification imaging by using the brain phantom and illumination light from a fiber tip. We found that when the tip is brought to about 1 mm from the sensor surface, sufficiently uniform excitation light was obtained. This has finally led to the successful in vivo fluorescence imaging and quantitative measurement of the AMC fluorophore. We believe that this work is important as it represents the first reported work of using a CMOS image sensor for functional imaging inside the intact mouse brain. From this work, we have gained important insight into the pulse modulation photosensing method and realized that more work would be needed in order to develop a pulse modulation based image sensor with fast frame rate imaging. Also, we have gained a more thorough understanding of the on-chip imaging configuration for in vivo imaging with the experimental determination of the achievable spatial resolution. A comparison with other non-invasive imaging methods is unavoidable, however, as discussed in the introduction of Chapter 4, the region of applications that the CMOS sensor is fairly wide. Thus, a direct comparison with other methods would be difficult, and instead the advantages of the CMOS sensor should be highlighted and further applications should be investigated.

6.1 Conclusion from Current Work

From Chapter 3, a model equation was developed to explain the CMOS photosensor sensitivity. This equation was further used to describe the image sensor characteristic for fluorescence detection. We have also developed a novel technique to package the CMOS image sensor for on-chip fluorescence imaging. By using this technique, we overcame the difficulty of fluorescence detection due to signal saturation under the intense excitation light. By using the packaged sensor, we demonstrated on-chip fluorescence imaging and detection. A brain tissue phantom was developed concurrently to serve as a platform for in vitro and in vivo fluorescence imaging.

From Chapter 4, in vitro and in vivo fluorescence imaging using the CMOS image sensor was demonstrated. Fluorescence imaging and quantitative measurement was performed deep inside the hippocampus of the mouse brain. In the experiment, optimization of the fiber tip distance from the sensor surface was performed experimentally. This work would further benefit from a more quantitative approach by numerical verification of the experimental result.

From Chapter 5, it was concluded that a CMOS chip fabricated using standard process was capable of generating sufficient electrical currents to stimulation the retinal cells. The pulse frequency modulation photosensing circuit used, has certain attractive properties which make it suitable for retinal cell stimulation. Based on this output, a programmable biphasic waveform was generated. Although this device was specifically targeted for use as a retinal prosthesis, other nerve cells that is susceptible to external electrical stimulation can be used. This will widen the range of experiments and applications where the CMOS stimulus chip can be used.

6.2 Future Outlook

From the conclusion of the work presented in Chapter 4, one immediate work that could be performed would be to use the CMOS image sensor for other functional imaging experiments of the mouse brain. One such experiment would include electrical stimulation of the hippocampus and studying its response by using fluorescence imaging methods. This is interesting for the study of brain memory and learning functions.

The successful demonstrations of on-chip imaging and electrical stimulus generation using a CMOS sensor chip have two important implications. First, we have created extra knowledge on the advantages of using CMOS technology for sensor chip fabrication. This information has positive impact and will definitely add on the current reported results. Second, the work that we have achieved here serves as the basic building block to propel and motivate further work involving the development of a truly multiparameter sensing and stimulation sensor chip. In this work, we have independently verified the imaging and electrical stimulus functions of the CMOS image sensor. By integrating the image sensing and electrical stimulation functions onto a single CMOS sensor chip, a multi-functional sensor chip can be realized. A long term objective would include the continuous effort in deploying CMOS-based sensors for use in the biomedical and scientific field.

Appendix A

Minimum Detectable Light Intensity in Photosensor Model

In Chapter 4, the minimum detectable light intensity from the photosensor model was defined as the reciprocal of the constant β of the following modeling equation.

$$y = \frac{\alpha}{(1+\beta \cdot x)^{\gamma}} \tag{A1}$$

The logarithmic plot for eq. (A1) produces a graph that has a characteristic as shown in Fig. A1. Further, the graph can be divided into two straight line asymptotes, y_1 and y_2, for the regions, $x \ll 1/\beta$ and $x \gg 1/\beta$, respectively, thus giving,

$$y_1 = \alpha, \tag{A2}$$

$$y_2 = \frac{\alpha}{(\beta \cdot x)^{\gamma}}. \tag{A3}$$

The x value whereby the two asymptotes meet has the value $1/\beta$. This is defined as the

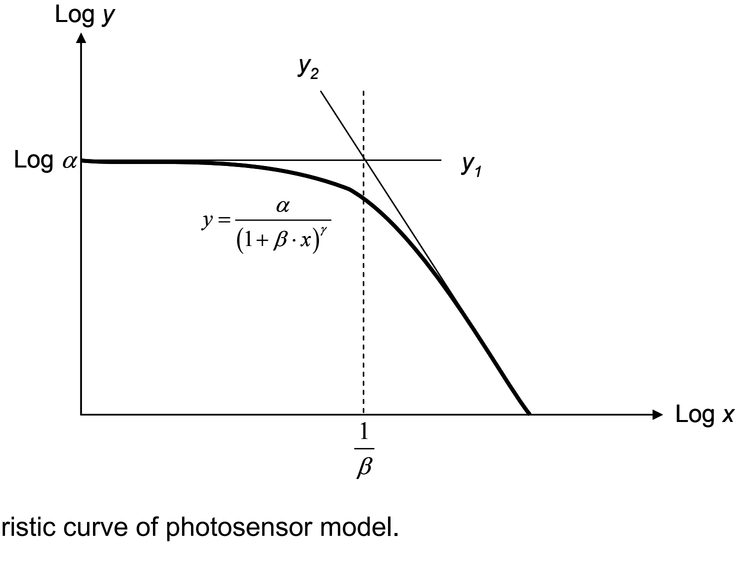

Fig. A1 Characteristic curve of photosensor model.

minimum detectable value as x decreases to 0. Further, from eq. (A3), the slope of the curve has the value, γ which is taken as the photosensor sensitivity.

Appendix B

Threshold Voltage of CMOS Inverter and Schmidt Trigger Inverter

In Chapter 5, the minimum threshold voltage of Schmidt trigger (ST) inverter was presented in the analysis of the analog PFM circuit. In the following discussion, the switching point voltage (threshold voltage) will be derived. Fig. B1 (A) shows the circuit of the CMOS inverter and its input-output characteristic. Because the derivation of the ST inverter threshold voltage is based on the same method to derive the threshold voltage of the CMOS inverter, it's derivation will also be shown here. Fig. B1 (B) shows the circuit of the modified-Schmidt trigger inverter used in Chapter 5 and its input-output characteristic.

For the inverter, the switching point voltage V_{SP} is defined as the point where the input voltage V_{in} is equal to the output voltage V_{out}. At this point, both the pMOS and nMOS transistor, M_{P2} and M_{N2} are operating in the saturation mode. Since Kirchoff's law holds true at all time, the current flow through the channels of the two transistors are equal. Hence,

$$\frac{k_{N1}}{2}\left(V_{SP}-V_{ThN1}\right)^2=\frac{k_{P2}}{2}\left(V_{DD}-V_{SP}-V_{ThP2}\right)^2, \tag{B1}$$

where, V_{ThN1} and V_{ThP2} are the threshold voltage at zero substrate bias of the M_{N1} and M_{P2} transistors, respectively, while k_{N1} and k_{P2} are the transconductance parameters of the transistors. These variables are defined as,

$$\begin{aligned} k_{N1}&=\frac{\mu_{N1}\cdot C_{ox}}{2}\left(\frac{W}{L}\right)_{N1} \\ k_{P2}&=\frac{\mu_{P2}\cdot C_{ox}}{2}\left(\frac{W}{L}\right)_{P1} \end{aligned} \tag{B2}$$

where, the μ_{N1} and μ_{P2} are the electron and hole mobilities of the n-type MOS and p-type MOS,

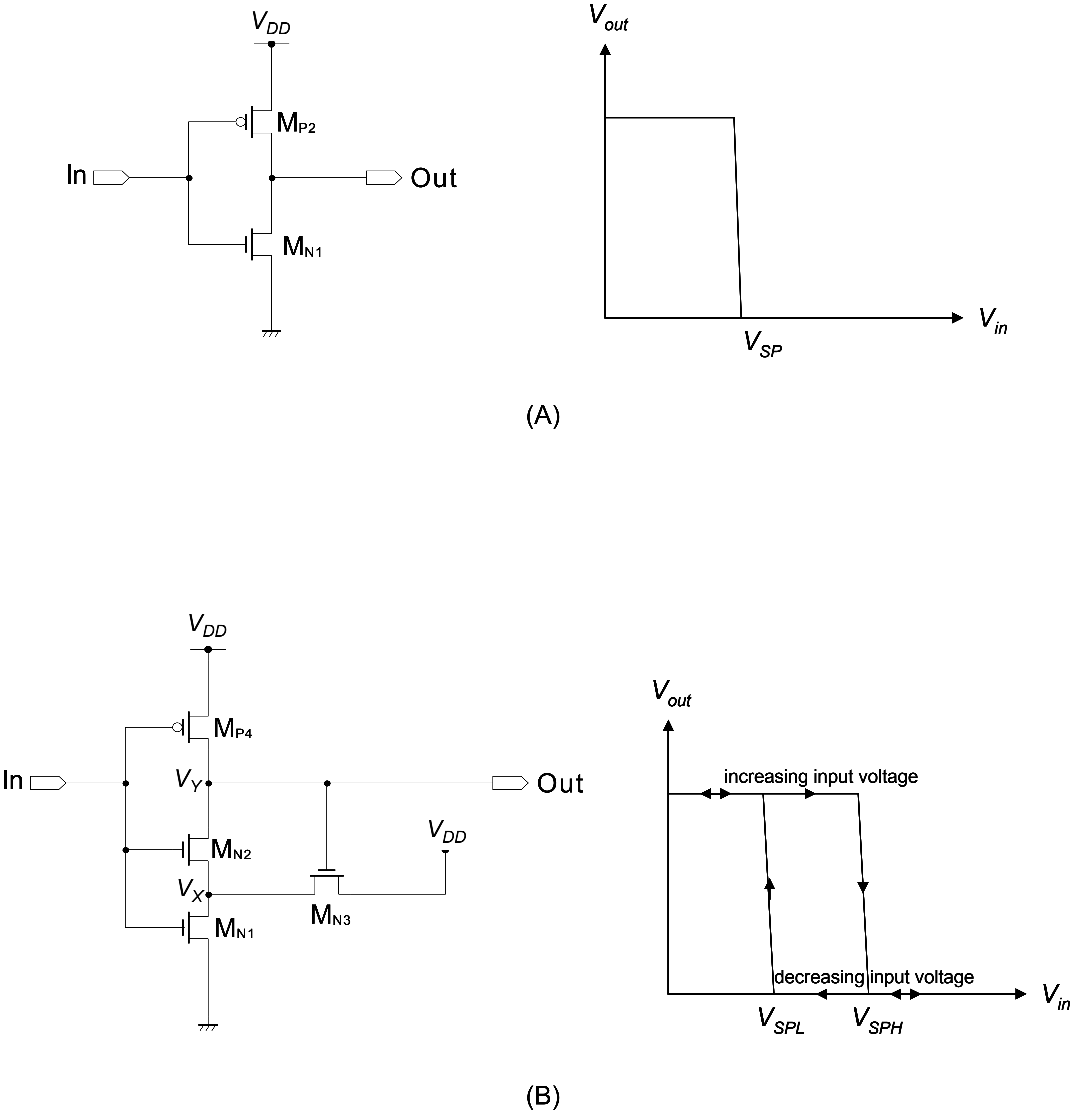

(A)

(B)

Fig. B1 (A) Schematic of the CMOS inverter circuit and its input output waveform. (B) Schematic of the modified-Schmidt trigger inverter circuit and its input output.

respectively. C_{ox} is the gate oxide capacitance per unit area, and W and L are the widths and lengths of the transistor gate, respectively. By rearranging eq. (B1), V_{SP} can be calculated as,

$$V_{SP} = \frac{V_{ThN1}\sqrt{\frac{k_{N1}}{k_{P2}}} + \left(V_{DD} - V_{ThP2}\right)}{\left(1 + \sqrt{\frac{k_{N1}}{k_{P2}}}\right)}, \tag{B3}$$

Next, we show how the lower and higher switching point voltages of the ST inverter, V_{SPL} and V_{SPL} are derived. In order to calculate, consider the case when the increasing in put voltage approaches V_{SPH} as shown in Fig. B1. At this state, the transistors M_{N1} and M_{N2} are off and M_{N3} is ON. Hence, the voltage

$$V_X = V_{DD} - V_{ThN3}. \tag{B4}$$

As the input voltage is increased further, M_{N1} is turned on and V_X falls. The switching point occurs when the output voltage goes low. At this point,

$$V_{in} = V_{SPH} = V_{ThN2} + V_X. \tag{B5}$$

Assuming M_{N1} operates in linear region, M_{N6} in saturation and M_{N4} remains off, the following current flow equation can be arrived at.

$$k_{N1}\left(V_{SPH} - V_{ThN1}\right)^2 = k_{N3}\left(V_{DD} - V_X - V_{ThN3}\right). \tag{B6}$$

V_{SPH} can then be found by assuming $V_{ThN2} = V_{ThN3}$ and substituting into (B5) gives,

$$V_X + V_{ThN3} = V_{SPH}, \tag{B7}$$

Substituting (B7) into (B6) we obtain

$$V_{SPH} = \frac{V_{DD} + V_{ThN1}}{2}. \tag{B8}$$

Finally, by using similar argument when the input current is decreased, the lower switching voltage, V_{SPL} can be found. By considering that both M_{N2} and M_{P4} in saturation,

$$k_{N2}\left(V_{SPL} - V_{ThN2}\right)^2 = k_{P4}\left(V_{DD} - V_{SPL} - V_{ThP4}\right)^2. \tag{B9}$$

Rearranging (B9) gives,

$$V_{SPL} = \frac{V_{ThN2}\sqrt{\frac{k_{N2}}{k_{P4}}} + \left(V_{DD} - V_{ThP4}\right)}{\left(1 + \sqrt{\frac{k_{N2}}{k_{P4}}}\right)}. \tag{B10}$$

By expanding the transconductance terms, the following expression can be obtained,

$$V_{SPL} = \frac{V_{ThN2}\sqrt{\frac{1}{n}\frac{\left(W/L\right)_{N2}}{\left(W/L\right)_{P4}}} + \left(V_{DD} - V_{ThP4}\right)}{\left(1 + \sqrt{\frac{1}{n}\frac{\left(W/L\right)_{N2}}{\left(W/L\right)_{P4}}}\right)}. \tag{B11}$$

where, *n* is defined as the mobility ratio of holes to electrons.

List of Publications

Technical Journals

1. D. C. Ng, K. Isakari, A. Uehara, K. Kagawa, T. Tokuda, J. Ohta, and M. Nunoshita, "A Study of Bending Effect on Pulse-Frequency-Modulation-Based Photosensor for Retinal Prosthesis," *Jpn. J. Appl. Phys.*, vol. 42, pp.7621-7624, Dec. 2003.

2. D. C. Ng, T. Tokuda, A. Yamamoto, M. Matsuo, M. Nunoshita, H. Tamura, Y. Ishikawa, S. Shiosaka, and J. Ohta, "On-chip Biofluorescence Imaging Inside a Brain Tissue Phantom Using a CMOS Image Sensor for In vivo Brain Imaging Verification," *Sens. Actuators B*, 2006, in press.

3. D. C. Ng, T. Tokuda, A. Yamamoto, M. Matsuo, M. Nunoshita, H. Tamura, Y. Ishikawa, S. Shiosaka, and J. Ohta, "A CMOS Image Sensor for On-chip in vitro and in vivo Imaging of the Mouse Hippocampus," *Jpn. J. Appl. Phys.*, 2006, in press.

4. D. C. Ng, T. Furumiya, K. Yasuoka, A. Uehara, K. Kagawa, T. Tokuda, J. Ohta, M. Nunoshita, "Pulse Frequency Modulation-based CMOS Image Sensor for Subretinal Stimulation," IEEE Trans. Circuits Syst. II, 2006, in press.

5. D. C. Ng, H. Tamura, T. Tokuda, A. Yamamoto, M. Matsuo, M. Nunoshita, Y. Ishikawa, S. Shiosaka, and J. Ohta, "Real Time In vivo Imaging and Measurement of Serine Protease Activity in the Mouse Hippocampus Using a Dedicated CMOS Imaging Device," *J. Neuroscience Methods*, 2006, in press.

Proceedings of International Conferences

1. D. C. Ng, T. Furumiya, A. Uehara, K. Kagawa, T. Tokuda, J. Ohta, M. Nunoshita, "Pulsed Frequency Modulation-based Retinal Implant Chip with 1-bit Pulse Image Processing," in *Proceedings Optics in Computing (OiC)*, Engelberg, pp. 11-12, Apr. 2004.

2. D. C. Ng, H. Okamoto, T. Tokuda, K. Kagawa, J. Ohta, M. Nunoshita, "A Pulse Modulation CMOS Image Sensor with 120dB Dynamic Range and 1nW/cm^2 Resolution for Bioimaging Applications," in *Extended Abstracts International Conference on Solid State Devices and Materials (SSDM)*, Tokyo, pp. 384-385, Sep. 2004.

3. D. C. Ng, M. Matsuo, T. Tokuda, K. Kagawa, M. Nunoshita, H. Tamura, Y. Ishikawa, S. Shiosaka, J. Ohta, “A CMOS Image Sensor for in vitro and in vivo Imaging of the Mouse Hippocampus,” in *Extended Abstracts International Conference on Solid State Devices and Materials (SSDM)*, Kobe, pp. 74-75, Sep. 2005.

4. D. C. Ng, M. Matsuo, T. Tokuda, K. Kagawa, M. Nunoshita, J. Ohta, “In vitro and In vivo On-chip Bio-fluorescence Imaging Using a CMOS Image Sensor,” in *Proceedings IS&T/SPIE 18th Annual Symposium Electronic Imaging*, vol. 6068, Feb. 2006.

Proceedings of Domestic Conferences and Meetings

1. D. C. Ng, K. Isakari, K. Kagawa, T. Tokuda, J. Ohta, M. Nunoshita, “A Study of Bending Effect (strain) on PFM-based Photosensor for Retinal Prosthesis,” in *Extended Abstracts The 50th Spring Meeting The Japan Society of Applied Physics (JSAP) and Related Societies,* Yokohama, no. 3, 29p-P12-3, p. 1392, Mar. 2003.

2. D. C. Ng, T. Furumiya, A. Uehara, K. Kagawa, T. Tokuda, J. Ohta, M. Nunoshita, “Pulsed Frequency Modulation-based Retinal Implant Chip with 1-bit Pulse Image Processing,” *Technical Report the Institute of Image Information and Television Engineers (ITE)*, vol. 27, no. 58, pp. 9-12, Oct. 2003.

3. D. C. Ng, H. Okamoto, T. Tokuda, K. Kagawa, J. Ohta, and M. Nunoshita, “Development of a CMOS Image Sensor for Bio-Imaging Applications using Pulse Modulation Method”, in *Extended Abstracts The 51st Spring Meeting 2004 The Japan Society of Applied Physics (JSAP) and Related Societies*, Tokyo, no. 3, p. 1120, Mar. 2004. (in Japanese)

4. D. C. Ng, H. Okamoto, T. Tokuda, K. Kagawa, J. Ohta, M. Nunoshita, “Pulse Modulation CMOS Image Sensor for Bio-fluorescence Imaging - On-chip Detection of Low Level AMC”, in *Extended Abstracts The 65th Autumn Meeting The Japan Society of Applied Physics (JSAP)*, Tokyo, no. 3, pp. 1144, Sep. 2004. (in Japanese)

5. D. C. Ng, H. Okamoto, M. Matsuo, A. Yamamoto, T. Tokuda, K. Kagawa, J. Ohta, M. Nunoshita, “Development of CMOS Imaging Chip for In vivo Bioimaging”, in *Digest of Technical Papers 25th Annual Meeting, 2005 The Laser Society of Japan*, Kyoto, pp. 220, Jan. 2005. (in Japanese)

6. D. C. Ng, Hideki Okamoto, Masamichi Matsuo, Akio Yamamoto, Takashi Tokuda, Keiichiro Kagawa, Jun Ohta, and Masahiro Nunoshita, "Development of CMOS imaging chip for in vitro and in vivo bioimaging", in *Extended Abstracts The 52nd*

Spring Meeting The Japan Society of Applied Physics (JSAP) and Related Societies, Saitama, no. 3, pp. 1466, Mar. 2005. (in Japanese)

7. D. C. Ng, M. Matsuo, A. Yamamoto, T. Tokuda, K. Kagawa, M. Nunoshita, J. Ohta, “Characterization of a CMOS image sensor for in vivo brain imaging using a modeled slice sample,” in *Extended Abstracts The 66th Autumn Meeting, 2005 The Japan Society of Applied Physics (JSAP)*, Tokushima, no. 3, pp. 1137, Sep. 2005. (in Japanese)

Awards

1. D. C. Ng, *Monbukagakusho Scholarship Award*, Apr. 2002.